Effective Date: June 18, 2014
Revision A

GSFC JPSS CMO
September 19, 2014
Released

Joint Polar Satellite System (JPSS) Ground Project
Code 474
474-00026

Joint Polar Satellite System (JPSS) OMPS Nadir Profile Ozone Algorithm Theoretical Basis Document (ATBD)

For Public Release

The information provided herein does not contain technical data as defined in the International Traffic in Arms Regulations (ITAR) 22 CFC 120.10. This document has been approved For Public Release.

Goddard Space Flight Center
Greenbelt, Maryland

National Aeronautics and Space Administration

Joint Polar Satellite System (JPSS)
OMPS Nadir Profile Ozone
Algorithm Theoretical Basis Document (ATBD)

JPSS Electronic Signature Page

Prepared By:

Ray Godin
JPSS Data Products and Algorithms EDR Lead
(Electronic Approvals available online at https://jpssmis.gsfc.nasa.gov/mainmenu_dsp.cfm)

Approved By:

Eric Gottshall
JPSS Data Products and Algorithms Manager
(Electronic Approvals available online at https://jpssmis.gsfc.nasa.gov/mainmenu_dsp.cfm)

Goddard Space Flight Center
Greenbelt, Maryland

Preface

This document is under JPSS Ground AERB configuration control. Once this document is approved, JPSS approved changes are handled in accordance with Class I and Class II change control requirements as described in the JPSS Configuration Management Procedures, and changes to this document shall be made by complete revision.

Any questions should be addressed to:

JPSS Ground Project Configuration Management Office
NASA/GSFC
Code 474
Greenbelt, MD 20771

Change History Log

Revision	Effective Date	Description of Changes (Reference the CCR & CCB/ERB Approve Date)
Original	04/22/2011	474-CCR-11-0041: This version baselines D43775, OMPS Nadir Profile Ozone Algorithm Theoretical Basis Document ATBD (ref AT60822-OMP-002), Rev C dated 10/28/2009 as a JPSS document, version Rev –. This is the version that was approved for NPP launch. Per NPOESS CDFCB - External, Volume V – Metadata, doc number D34862-05, this has been approved for Public Release into CLASS. This CCR was approved by the JPSS Algorithm ERB on April 22, 2011.
A	06/18/2014	**474-CCR-13-1249:** Approved by the JPSS Ground Algorithm ERB on November 7, 2013. Changed Sections 3.1.2, 3.1.2.7 – 3.1.2.11. **474-CCR-14-1798:** Approved by the JPSS Ground Algorithm ERB on June 18, 2014. Changed Section 3.1.2.6.

Northrop Grumman Space & Mission Systems Corp.
Space Technology
One Space Park
Redondo Beach, CA 90278

Engineering & Manufacturing Development (EMD) Phase
Acquisition & Operations Contract

CAGE NO. 11982

OMPS Nadir Profile Ozone Algorithm Theoretical Basis Document ATBD (ref AT60822-OMP-002)

Document Number: D43775

Document Date: 10/28/2009

Revision: C

Point of Contact: Bhaswar Sen, A&CV

ELECTRONIC APPROVAL SIGNATURES:

_____
Bruce Hauss, A&CV IPT Lead

_____

Prepared by
Northrop Grumman Space Technology
One Space Park
Redondo Beach, CA 90278

Prepared for
Department of the Air Force
NPOESS Integrated Program Office
C/O SMC/CIK
2420 Vela Way, Suite 1467-A8
Los Angeles AFB, CA 90245-4659

Under
Contract No. F04701-02-C-0502

Northrop Grumman Space & Mission Systems Corp.
Space Technology
One Space Park
Redondo Beach, CA 90278

NORTHROP GRUMMAN
Raytheon

Revision/Change Record

Document Number D43775

Revision	Document Date	Revision/Change Description	Pages Affected
---	02/12/2007	Initial PCIM Release to bring document into Matrix Accountability. Reference original document number: AT60822-OMP-002 delivered in 2004	All
A	07/24/2008	Updated section 3.1 to reflect algorithm changes described in SPCRs 1240, 1241, 1242 and 1268. Removed reference to CMIS	31-94 All
B	02/11/2009	Revision of the SDR algorithm description to be consistent with the software updates by ECR-A-192. Corrected typos. Added system level reference documents. Affected sections 1, 2, and 3.1	1-76
C	10/28/2009	Revision of the EDR algorithm description to be consistent with the software updates by ECR-A-**261B.**	All

Raytheon Revision/Change History

Revision	Document Date	Revision/Change Description	Pages Affected
Draft	March 1, 1999	1st Draft Release.	All
Revised Draft	April 6, 1999	Proposal Modifications	All
RRR1	February 15, 2000	Updated for RRR1	All
RRR2	November 5, 2000	Corrections, update of SDR algorithm	All
RRR3	July 23, 2001	Further corrections, update of SDR algorithm Removal of Section 8, Appendices D and E	All
CDR (Rev. B)	December 8, 2002	Update of SDR algorithm, added SDR interpolation study, performance updates, accuracy and precision tables for specs.	All
Rev. C	February 25, 2004	NGST SPCR ALG00000307: Sec. 3.2.7, 6.3 and Appendix A: references to microgm/gm have been changed to ppmv to reflect system specifications; Sec.6.3:Eq.(62) Referenced;Sec.6.3 spelling errors corrected; Sec. 8 and Appendices A, B, and C corrected for page numbers	All
Rev D	July 20, 2004	Updated for V4.4 SDR algorithm release Revised geolocation section, removed attitude correction section Multiple corrections prior to official algorithm	All

		release to IDPS	

TABLE OF CONTENTS

Page

LIST OF FIGURES

Page

LIST OF TABLES

Page

1 Introduction

The Ozone Mapping and Profiler Suite (OMPS) is an important component of the National Polar-Orbiting Operational Environmental Satellite System (NPOESS). The OMPS mission is to provide the NPOESS users with data products that describe the vertical, horizontal, and temporal distribution of ozone in the Earth's atmosphere. These data (or Environmental Data Records - EDRs) are derived from the spaceborne ultraviolet, visible, and near infrared observations of a two-sensor system.

1.1 SYSTEM DESCRIPTION

The nadir system has two focal planes: one operating from 300 to 380 nm for total column ozone observations, and the other operating at 250 to 310 nm for profile ozone observations. Together with the interface and control electronics they are the OMPS sensor suite. For the NPP mission, the OMPS sensor suite also contains a limb system that has a focal plane operating from 290 to 1000 nm for high vertical resolution profile ozone observations.

The ground processing system will receive and process the sensor data into Raw Data Records (RDRs), Sensor Data Records (SDRs) and EDRs or Intermediate Products (IPs). These data products will be delivered to the NPOESS users in pre-defined format and contents.

The OMPS system will produce one NPOESS EDR, ozone Total Column (TC). In addition, it will produce the ozone nadir profile IP. The EDR requirements thresholds listed in section 40.3.2 of the NPOESS system specification, document SY15-0007, shall be met when data from OMPS is processed using the operational algorithms described in these ATBDs.

The OMPS algorithms include the following:

1 The **Nadir Total Column Ozone SDR algorithm** was originally developed by the OMPS sensor subcontractor and significantly improved by NGST to meet the NPOESS program need.

2 The **Nadir Profile Ozone SDR algorithm** was originally developed by the OMPS sensor subcontractor and significantly improved by NGST to meet the NPOESS program need.

3 The **Nadir Total Column Ozone Algorithm** is adapted from the heritage TOMS version 7 algorithm. We have included modular enhancements to meet EDR requirements and to provide for graceful degradation.

4 The **Nadir Profile Ozone Algorithm** is adopted from the heritage SBUV/2 operational algorithm. The ozone profile from this algorithm provides a link to the heritage twenty-year ozone profile data set.

Figure 1.1-1 maps the flow of the OMPS data from the sensors through the RDR, SDR, and EDR Algorithms. For the SDR algorithm, the figure identifies the required inputs as the external

EDRs, the climatological databases, and the calibration data. For the EDR Algorithms, this figure also identifies the connection between the algorithms.

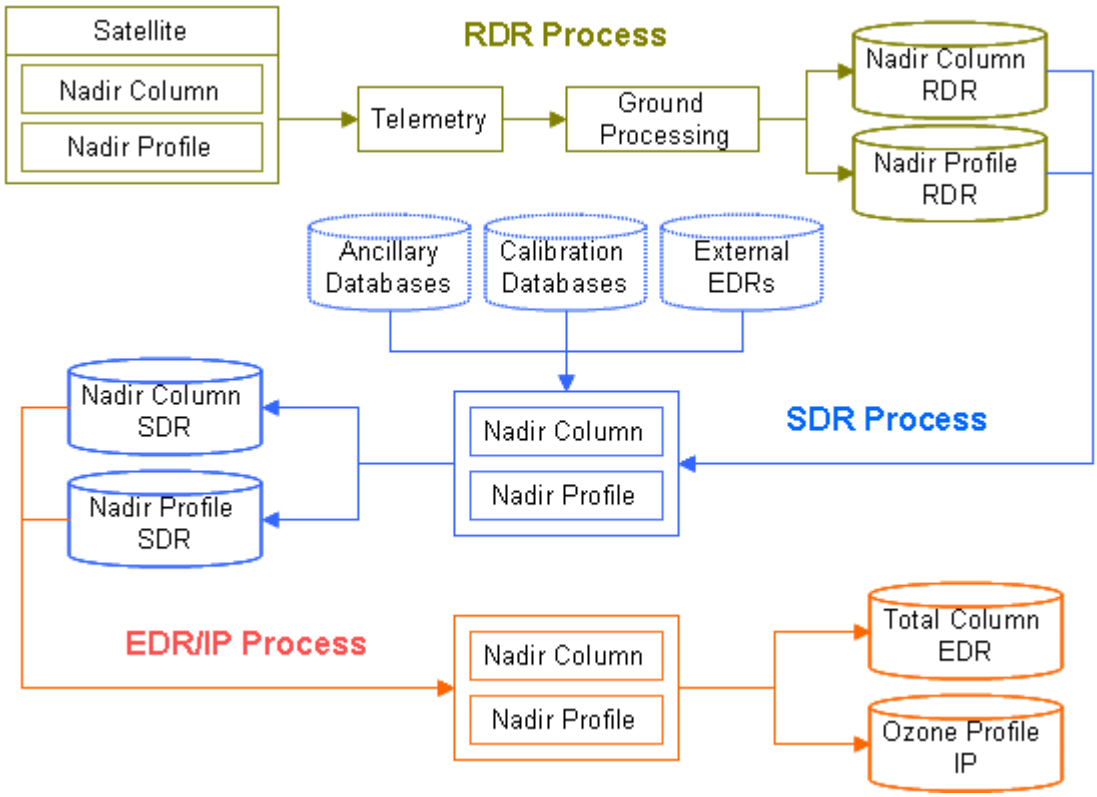

Figure 1.1-1. Overview of the data flow from sensors input to the generation of RDR, SDR and EDR/IP data products

1.2 OBJECTIVES

This Algorithm Theoretical Basis Document (ATBD) describes the algorithm used to retrieve the OMPS Nadir Profile Ozone Product. The primary data product produced by the OMPS Nadir Profiler (NP) will be the layer ozone amounts for all solar zenith angle viewing conditions less than or equal to 80 degrees. This document identifies the sources of input data that are required by the algorithm, provides the physical theory and mathematical background underlying the use of this information, describes practical considerations affecting the algorithm, lists any assumptions employed in the algorithm retrieval process, describes the data products, and details expected sensor and algorithm errors (accuracy and precision).

1.3 OVERVIEW

The OMPS nadir profiler is designed to provide continuity for heritage ozone profile measurements made by the BUV, SBUV, and SBUV/2 instruments. This continuity will serve to reduce risk to NOAA's primary mission of long-term ozone measurement associated with a change in measurement technique at the outset of the NPOESS era. Also, the fundamental sensitivity of the nadir Backscatter Ultraviolet (BUV) measurement to the upper level scale height of ozone will help to fill a critical need of pressure altitude registration for the OMPS Limb profiler that will fly on NPP satellite.

These needs are filled by the OMPS Nadir Profiler (NP) at a low cost for two main reasons. One is that the NP sensor is integrated with the primary nadir sensor for total column, so that the incremental costs of providing the expanded wavelength coverage is low. The other reason is that the retrieval algorithm, by design, would be adopted from the current SBUV/2 processing system, and adapted to the NPOESS environment, thereby reducing development costs. In the same vein, the SDR algorithm will be extremely similar to the algorithm used for the OMPS Nadir Total Column Sensor (TC). This means that once the TC SDR algorithm is established, only slight modifications will be required to adapt the same algorithm to the NP.

Because the NP retrieval algorithm is to be adopted/adapted directly from the existing algorithm, we have borrowed heavily from existing government documentation in assembling the IP retrieval portions of this ATBD. A substantial amount of the material below has been reproduced from the NASA Reference Publication 1234, 1990, “Nimbus 7 Solar Backscatter Ultraviolet (SBUV) Ozone Products User's Guide.” We trust this expediency will be viewed as the beginning of a history of cost savings derived from the re-useable nature of this algorithm concept. The NASA Publication describes Version 5 of the SBUV ozone algorithm. We have updated this description to apply to the Version 6 algorithm being applied to the SBUV/2 data currently being obtained by NOAA. Our retrieval algorithm development will consist mainly of creating an interface adapter module that will convert the OMPS nadir profiler SDR into the form currently used as input to the Product Processor module that is the current NOAA equivalent of an OMPS SDR.

1.4 DATA PRODUCTS

Clearly, the primary data product produced by the OMPS Nadir Profiler (NP) will be the layer ozone amounts derived by the retrieval algorithm. It is this data that will provide continuity to the long-term ozone monitoring community. As mentioned in section 1.1, the layer ozone amounts product derived from NP SDRs is an IP, not an EDR.

It is the quantities C and sigma, which are described in more detail in Sections 2 and 6, that parameterize the ozone scale height of the upper atmosphere (around 1 mb), and contain information about the pressure altitude registration of the Limb Profiler measured ozone profile (See ICSR 9020401).

The NP retrieval provides additional information including an estimate of the total column ozone and the Lambertian equivalent surface reflectivity of each measured scene; all of this information is described in Section 6.

1.5 APPLICABLE DOCUMENTS

1.5.1 NPOESS system level documents:

NPOESS System Specification, DOC SY15-0007, Rev N
Operational Algorithm Description Document for the OMPS NP SDR Algorithm Software (D39546)
Operational Algorithm Description Document for the OMPS NP IP Algorithm Software (D38045)
NPP EDR Production Report, Document Number D37005
EDIR Interdependency Report, Document Number D36385
NPOESS Common Data Format Control Book, Document Number D34862

1.5.2 OMPS system level documents

1.5.2.1 Controlling Documents

OMPS System Specification – Document Number 542798
OMPS Algorithm Development Specification – Document Number 542808

1.5.2.2 OMPS Reference Documents

OMPS Algorithm Theoretical Basis Document: Nadir Total Column Ozone Algorithm—Document Number D43774.
OMPS Algorithm Theoretical Basis Document: UV/VIS Limb Profile Ozone Algorithm—Document Number IN0092-107.
OMPS Algorithm Theoretical Basis Document: Nadir Profile Ozone Algorithm—Document Number D43775.
OMPS Algorithm Theoretical Basis Document: IR Total Column Ozone Algorithm—Document Number IN0092-109.
OMPS Algorithm Test and Verification Plans and Procedures (ATVPP) – Document Number IN0092-124.

1.6 REVISION HISTORY

The original version of this document was dated March 1, 1999. Revisions to this document were made as the nadir sensor design and algorithm matured, and as performance information was verified and validated.

In February 12, 2007, this document was re-baselined and checked into the NPOESS Matrix system by NGST. Subsequent revisions since this initial PCIM release are

recorded in Table 1.6-1. Change and revision history prior to the PCIM release is documented in Table 1.6-2.

Table 1.6-1 Revision History of This Document

Revision	Document Date	Revision/Change Description	Pages Affected
---	02/12/2007	Initial PCIM Release to bring document into Matrix Accountability. Reference original document number: AT60822-OMP-002 delivered in 2004	All
A	07/24/2008	Updated section 3.1 to reflect algorithm changes described in SPCRs 1240, 1241, 1242 and 1268. Removed reference to CMIS	31-94 All
B	02/11/2009	Revision of the SDR algorithm description to be consistent with the software updates by ECR-A-192. Corrected typos. Added system level reference documents. Affected sections 1, 2, and 3.1.	1-76
C	10/16/2009	Revision of the EDR algorithm description to be consistent with the software updates by ECR-A-261	

Table 1.6-2. Revision History of This Document Prior to PICM Release

Revision	Release Date	Section	Change Type
CFI	April 6, 1999		Draft release
RRR1	February 15, 2000	3.1.1	Make SDR content consistent with Algorithm Development Specification document
		Table 2.5-1	Time dependent error estimates revised
		3.1.3.3	Expanded diffuser deployment schedule discussion
		Table 7.5-1	Radiometric calibration error estimates revised
		8.1-8.2	Align ATBD with ATVPP
		Appendix E	Added to track LOC
RRR2	November 5, 2000	3	Updated SDR earth view and calibration
		1.8	Updated contributing author list
RRR3	July 23, 2001	3	Further updated SDR description, reviewed and corrected EDR description
		8	Deleted Section 8
		D	Deleted Appendix D (now described in Version Description Document)
		E	Deleted Appendix E
		All	Corrected typographical and grammar errors
CDR	November 23, 2002	3	Updated SDR production section
		3	Added SDR interpolation subsection
		7	Added stray light study
		7	Added SNR sensitivity study
		5	Updated data requirements
		4	Updated assumptions and future version
		7	Added summary for accuracy and precision budget
		All	Corrected typographical and grammar errors
Rev. C	February 25, 2004	3.2.7, 6.3, A	NGST SPCR ALG00000307: mass mixing ratio (micro-gm/gm) changed to that of volume mixing ratio (ppmv)
		6.3	Eq.(62) referenced; spelling errors corrected
		8, A, B, C	page numbering errors corrected
Rev. D	July 20, 2004	All	Updated for V4.4 SDR algorithm release
			Removed attitude correction section
			Revised geolocation section

1.7 CONTRIBUTING AUTHORS

The following people have contributed to the development of the algorithm software and documentation for the production of the NPOESS ozone data products (including the IR Ozone product):

Colin Seftor Raytheon
Igor Shimansky Raytheon

Lack Larson	Raytheon
Hilary Snell	AER, Inc
Susan Beresford	AER, Inc.
Richard Buss	Raytheon
Brent Canova	Ball Aerospace & Technologies Corp.
Kelly Chance	Harvard-Smithsonian
David Flittner	University of Arizona
Jeffrey Hayes	Raytheon
Jennifer Hegarty	AER, Inc.
Benjamin Herman	University of Arizona
Glen Jaross	Raytheon
James Leitch	Ball Aerospace & Technologies Corp.
Jean-Luc Moncet	AER, Inc.
John Qu	Raytheon
Hélène Rieu	AER, Inc.
Juan Rodriguez	Ball Aerospace & Technologies Corp.
James Russell	Hampton University
Colin Seftor	Raytheon
Richard Slonaker	Raytheon
Thomas Swissler	Consultant
Charles Wellemeyer	Raytheon

2 Scientific Basis

2.1 PHYSICAL DESCRIPTION

Interpretation of the radiance measurements made by a Backscatter UltraViolet (BUV) instrument requires an understanding of how the Earth's atmosphere scatters ultraviolet radiation as a function of solar zenith angle. Incoming solar radiation undergoes absorption and scattering by atmospheric constituents such as ozone, Rayleigh scattering, and scattering by aerosols. Radiation that penetrates to the troposphere is scattered by clouds, and radiation that reaches the ground is scattered by surfaces of widely differing reflectivity. The wavelengths chosen for BUV measurements were selected because of their high ozone absorption. At all of these wavelengths absorption by other atmospheric components is normally negligible compared to that of ozone. However, at the 255 nm channel originally chosen for the SBUV, nitrogen oxide γ-band emission has a non-negligible contribution, and this wavelength has, therefore, not been used in SBUV ozone retrievals. A new channel at 252 nm has been selected for use on subsequent SBUV/2 sensors. The ozone absorption coefficients differ from band to band, increasing as the wavelength decreases. Consequently, as wavelength decreases, significant absorption occurs at progressively higher levels in the atmosphere. Although in principle the backscattered intensity at a given wavelength depends upon the entire ozone profile x(p) from the top of the atmosphere to the surface, in practice it is sensitive only to the profile over a restricted range in altitudes. Consequently, measurements of backscattered radiation at shorter wavelengths yield information on the ozone profile at higher levels of the atmosphere than measurements at longer wavelengths.

At wavelengths shorter than about 295 nm, solar radiation is almost completely absorbed above the ozone density peak at 20-25 km. Because the intensity of the backscattered radiation at these wavelengths is determined solely by the ozone profile above the peak, it can be used to derive that part of the ozone profile. At these wavelengths, tropospheric features, including clouds, aerosols, and terrain height, do not affect the radiation scattering and can be ignored. The computation of atmospheric scattering for the shorter wavelengths is easier than it is for the longer wavelengths.

Between 295 nm and 310 nm, scattering takes place over a wide range of altitudes. The backscattered intensity depends upon the height of the ozone peak as well as the ozone amount below the peak. Radiation at these wavelengths thus provides profile information near and below the ozone peak.

For wavelengths longer than 310 nm, the backscattered radiance consists primarily of solar radiation that penetrates the stratosphere and is reflected back by the dense tropospheric air, clouds, aerosols, and the Earth's surface; scattering takes place predominantly in the troposphere. For these wavelengths, the backscattered intensity is determined primarily by the total optical depth of the atmosphere above the scattering layer; details of vertical variation in the optical depth function $\tau_\lambda(p)$ become largely

unimportant. The amount of ozone below the scattering layer is small and can be estimated with sufficient accuracy to permit derivation of total column ozone. Because most of the ozone is in the stratosphere, the principal effect of the total atmospheric ozone is to attenuate both the solar flux going to the troposphere and the component reflected back to the satellite. This separation of the absorbers in the stratosphere (i.e., ozone) and the “reflector” in the troposphere (i.e., atmospheric scattering, clouds, and Earth surface) causes backscattered radiances longer than 310 nm to depend weakly on the vertical distribution of ozone in the stratosphere.

Derivation of atmospheric ozone content from measurements of the backscattered radiance requires a treatment of scattering from the Earth’s surface, by clouds, and by other aerosols. These scattering processes are not isotropic; the scattered light depends upon both incident angle and viewing angle. In principle, then, the reflectivity is a function of solar zenith angle. Studies by Dave (1978) and by Fraser and Ahmad (1978) show that, in practice, the contribution of clouds and aerosols to the backscattered intensity can be treated by assuming that radiation is reflected from a particular pressure level called the “scene pressure” with an effective “scene reflectivity” R. Thus, in addition to deriving a reflectivity for the albedo calculations, a pressure level for the effective reflecting surface must be defined for each instantaneous field of view (IFOV).

2.2 SENSOR DESCRIPTION

The NPOESS satellite will operate in a near circular, sun-synchronous orbit. The nominal orbit for the satellite is 833 km altitude, 98.7 degree inclination. The orbit will be a "precise" orbit (i.e., altitude maintained to +/-17 km, nodal crossing times maintained to 10 minutes throughout the mission lifetime) to minimize orbital drift (precession). The NPOESS platform will be capable of flying at any equatorial node crossing time. However, the nominal configuration will be a nodal crossing time of 1330.

The OMPS nadir sensor is a double focal plane UV grating spectrometer with the nadir profiling radiances measured using a two-stage spectrometer similar in optical design to the SBUV/2 instrument. The nadir profiler spectrometer shares a telescope with the total column spectrometer; its FOV is co-boresighted with total column FOV. The nadir profiler FOV is 250 km cross track with a reporting interval of 250 km along track. Spectral resolution is 1 nm across the spectral range of 250 to 310 nm. The expected signal-to-noise ratios (SNRs) for the eight spectral channels used in the nadir profiling algorithm are higher than those attained with the SBUV/2 instrument, with the exception of the 252 nm channel (SNR of 41 vs. 65). The center wavelengths, minimum required SNRs, and minimum radiances for the channels covered by the nadir profiling focal plane are given in **Table 2.2-1**. The nadir profile spectrometer is expected to meet or exceed these SNRs. Spectral channels supplied by the nadir total column spectrometer are listed in **Table 2.2-2**. A depolarizer in the telescope keeps the linear polarization sensitivity below 1%.

Table 2.2-1. Channel Wavelengths, Required SNRs, and Expected Minimum Radiances for the Nadir Profile Spectrometer

Wavelength nm	Minimum SNR	Min. Radiance ph/sec-cm^2-sr-nm
252.00	35	1.52E8
273.61	100	6.86E8
283.10	200	1.39E9
287.70	260	1.88E9
292.29	400	3.52E9
297.59	400	5.21E9
301.97	400	5.84E9
305.87	400	1.03E10

Table 2.2-2. Wavelengths and SNRs Supplied by the Nadir Total Column Spectrometer

Wavelength (nm)	Minimum SNR	Min. Radiance (ph/sec-cm^2-sr-nm)
312.5	1000	2.61E12
318	1000	3.26E12
331	1000	4.43E12
336	1000	1.17E13
364	1000	5.01E12
377	1000	5.16E12

On-orbit calibration is provided by weekly solar irradiance measurements with a reflective diffuser at the entrance aperture. The albedo calibration, defined as the ratio of radiance calibration to irradiance calibration at the same wavelength, will be determined to an accuracy better than or equal to 2% at all wavelengths from 250 - 310 nm. Working and reference diffusers are used to monitor diffuser degradation. The reference diffuser comparisons should be able to measure working diffuser reflectance changes at the level of 0.1% per year to provide good long-term stability of sensor measurements.

2.3 FORWARD MODEL

The calculation of albedos follows the formulation of Dave (1964). We define the backscattered albedo as the ratio of the radiance backscattered from the Earth/atmosphere to the solar irradiance incident on the top of the atmosphere. Consider an atmosphere bounded below by a Lambertian surface of reflectivity R. For unit incident solar irradiance at a solar zenith angle of θ_0, the intensity I of the radiation scattered toward the zenith can be expressed as

$$I(\theta_0, R, \tau) = I_0(\theta_0, \tau) + RI_s(\theta_0, \tau) f_1(\tau) / \left[1 - Rf_2(\tau)\right], \quad (1)$$

where the two terms on the right-hand side represent the atmospheric and surface contributions to the backscattered radiation, respectively. I_s is the intensity of direct and diffuse radiation reaching the surface, f_1 is the fraction of reflected radiation directed towards the zenith, and f_2 is the fraction of reflected radiation scattered back to the surface. These quantities are complex functions of θ_0 and $\tau_\lambda(p)$; the latter represents the optical depth of the atmosphere at a given wavelength as a function of the atmospheric pressure p. The product of I and f_1 is often combined into one term designated as T. For an atmosphere containing only Rayleigh scatterers and ozone, $\tau_\lambda(p)$ can be written as $\tau_\lambda(p) = \alpha_\lambda x(p) + \beta_\lambda p$ where, x(p) is the column ozone amount above a pressure p, α_λ is the ozone absorption coefficient, and β_λ is the Rayleigh scattering coefficient averaged over the instrument bandpass centered at λ.

At wavelengths below 290 nm, little solar radiation penetrates below 30 km, permitting surface, cloud, and aerosol effects to be ignored; because radiation is scattered from a region of the atmosphere which is optically thin for scattering, multiple scattering effects may also be ignored. For such cases, the backscattered intensity I in (1) can be explicitly written to a high degree of accuracy as

$$I_\lambda = (1/4\pi) F_\lambda \beta_\lambda P(\cos\theta_0) \int \exp[-s(\alpha_\lambda x(p) + \beta_\lambda p)]\, dp. \quad (2)$$

This expression for I_λ is commonly described as the single scattering radiance. The Rayleigh phase function $P(\cos\theta_0)$, assuming a depolarization factor of 0.035 (Bates, 1984), can be written as

$$P(\cos\theta_0) = 0.7619\ (1 + 0.937\cos^2\theta_0). \quad (3)$$

The slant path (air mass) s can be approximated by $1+\sec(\theta_0)$ at low solar zenith angles (<60°), or by the Chapman (1931) function at moderate solar zenith angles (60°-80°). For solar zenith angles greater than 80°, s must be treated as a function of p, calculated by ray-tracing.

It is convenient to describe the ratio of backscattered to incident radiation in terms of a parameter Q_λ, defined by the following expression:

$$Q_\lambda = \{4\pi / [(\beta_\lambda P(\cos\theta_0)]\}(I_\lambda / F_\lambda). \quad (4)$$

For the single scattering case defined by (2),

$$Q_\lambda = \int C_\lambda(p)\, d(\log p), \quad (5)$$

where

$$C_\lambda(p) = \partial Q_\lambda / \partial \log p = p \exp\left[-s(\alpha_\lambda \chi(p) + \beta_\lambda p)\right]. \quad (6)$$

Q_λ, which is the product of the single scattering albedo and physical and numerical constants, has the dimensions of pressure. Its value is typically close to the pressure near which most of the radiation at wavelength λ is backscattered. C_λ (p) is called the contribution function. It defines the shape of the scattering layer and is plotted in **Figure 2.3-1** for the SBUV wavelength bands (see Table 3.3-1). The contribution function derived in (6) completely describes the scattering layer only for wavelengths shorter than 290 nm.

For longer wavelengths, in addition to the single scattering component described by (2), there is an additional component of the backscattered radiation originating in the dense troposphere and at the Earth's surface. This additional component is described as multiple scattering and reflectivity (MSR). The position p_{max} of the peak of the contribution function is derived by setting dC/dp = 0, which gives

$$\beta_\lambda s p_{\max} + \alpha_\lambda s \, dx / d \log p = 1. \quad (7)$$

This result shows that, in general, there can be two peaks in the contribution function—one determined by the strength of ozone absorption at a given wavelength (α_λs), and the other by the optical path for Rayleigh scattering (β_λs). The former peak occurs where the partial pressure of ozone in the atmosphere (dx/d log p) attains a value equal to $(\alpha_\lambda s)^{-1}$ and the latter peak is at a pressure equal to $(\beta_\lambda s)^{-1}$. For the shorter SBUV wavelengths the former peak dominates the latter, lower tropospheric peak because of the strong attenuation of the ultraviolet light near the ozone peak. However, at moderately absorbing wavelengths near 300 nm, both peaks can have equal strength, as seen in Figure 2.3-1.

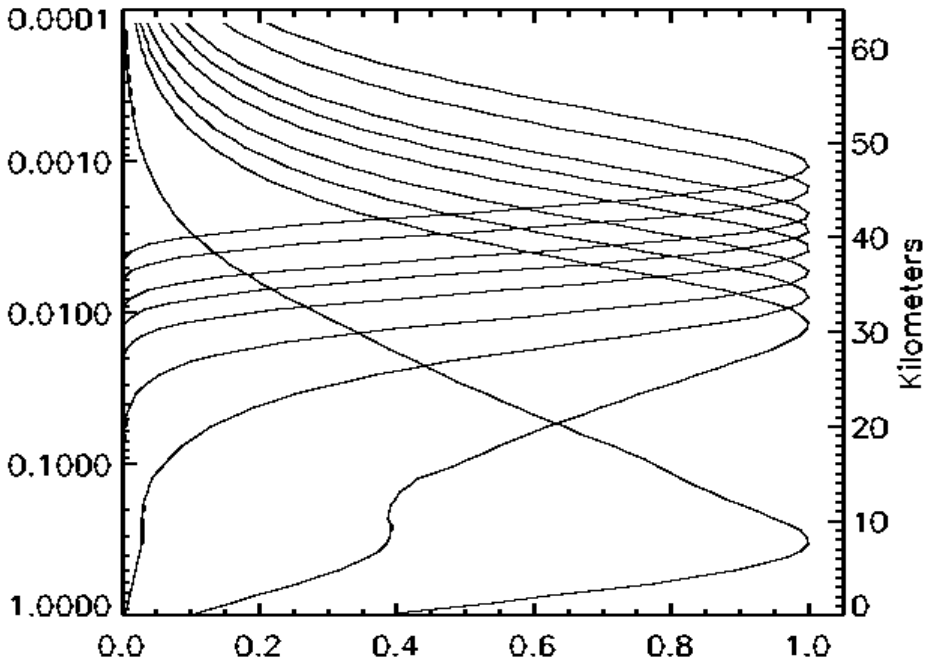

Figure 2.3-1. Single scattering contribution functions for the ozone profiling wavelength channels listed in Table 2.2-1

2.4 RETRIEVAL

The retrieval of total ozone is based on a table lookup and interpolation process (Klenk et al., 1982). A table that gives backscattered radiance as a function of total ozone, solar zenith angle, surface pressure, surface reflectivity, and latitude is constructed. Given the computed radiances for the latitude, surface pressure, reflectivity, and solar zenith angle of each radiance measurement, the total ozone value for the scan can be derived by interpolation in the table.

The wavelength dependence of the backscattered radiance for the eight shortest wavelengths measured by the experiment is a function of the ozone profile. However, this profile cannot be derived directly from the measured radiances. Because the radiances are integrals of contributions from various levels, the ozone profile solution consistent with a set of radiance measurements is not unique. Some constraints are needed in order to find the mathematical solution that represents physical reality. The profile algorithm uses an optimum statistical method (Rodgers, 1976; Bhartia et al., 1981; Klenk et al., 1983; Bhartia et al., 1996) to obtain profiles from the measured radiances and from *a priori* information that includes a first guess profile and an estimate of its variance, the estimated errors in the measurements, and the correlations between profile variance and errors of measurement at different levels. The *a priori*

information provides a constraint on which of the solutions consistent with the measurements is to be accepted, and the optimum method governs the way in which the constraint is applied. Section 3.3 describes the algorithms for both total ozone and ozone profiles in greater detail.

2.5 ERROR SOURCES

The ozone values derived from BUV measurements have three types of uncertainties: uncertainties in the basic measurements, uncertainties in the physical quantities needed to retrieve ozone values from the measurements, and uncertainties in the mathematical procedure used to derive ozone values from the measurements. In addition, the limits on the inherent information content of the measurements must always be considered in studying the ozone values derived from BUV measurements. This section summarizes the essential points. Section 7 discusses these uncertainties in greater detail.

Table 2.5-1 summarizes the overall uncertainties. The total ozone value derived from BUV observations is the integrated amount of ozone from the top of the atmosphere down to the average altitude of the Earth's surface in the instrument's instantaneous field of view. When clouds are present, the instrument cannot detect the ozone below them. In such cases, the reported total ozone includes an estimated ozone amount in the atmosphere below the clouds. This estimation procedure is described in Section 3.3. It is also worthwhile to note that even in the absence of clouds, the backscattered radiances are relatively insensitive to the ozone near the surface. Therefore, the BUV derived "total ozone" will not respond fully to fluctuations in the ozone concentration near the surface. This issue is discussed by Klenk et al. (1982).

The BUV ozone profiles are reported in two forms. The primary results from the algorithm are layer ozone amounts in Umkehr layers, defined in Table A.1, which, except for the lowest and the highest layers, are roughly 5 km in height. For the convenience of the users, the ozone values are also reported as ozone mixing ratios at 19 pressure levels.

The threshold long-term stability indicated in Table 2.5-1 can be achieved by maintaining the long-term albedo calibration to 0.5% over the nominal 7 year lifetime of the OMPS Sensors (see Table 7.2-1). This is accomplished through the use of a diffuser carousel described in Section 3.1.2.

In either case, it is important to note that the inherent vertical resolution of the measurements is about 8 km between the altitudes of 30-50 km. Below 30 km the resolution degrades rapidly. Below 20 km the SBUV/2 has little structural information about the ozone profile; the primary information consists of the layer amount of ozone between 20 km and the reflecting surface. Above 50 km the information provided is generally not useful except at high solar zenith angles. Very close to the terminator the range of validity extends up to 60 km. The limited vertical resolution of the backscatter ultraviolet technique must be considered in studies of the ozone vertical profiles derived from using this technique.

Table 2.5-1. Overview of Uncertainties

Type of Error	Level				
	(~48 km) 1 mbar	3 mbar	10 mbar	30 mbar	Total
Random (rms)	5%	3%	5%	10%	2%
Absolute (bias)	7%	5%	5%	6%	3%
Time-dependent (Over 7 years)	1%	0.7%	0.5%	0.5%	0.5%

3 Algorithm Description

3.1 SDR DATA PRODUCTION

This section describes the contents of and process by which Sensor Data Records (SDRs) are generated from the input Raw Data Records (RDRs). The two basic RDR types, Earth view and calibration, are processed separately by the SDR algorithm. The primary products of calibration processing are databases that store the results of calibration analyses. These databases are subsequently used during Earth data processing to adjust the spectral and radiometric calibrations of those data. **Figure 3.1-1** illustrates the major processing components of the SDR algorithm. The basic components of SDR processing: signal correction, calibration analysis, and calibration application, are all automated. Intervention is required only for anomalies.

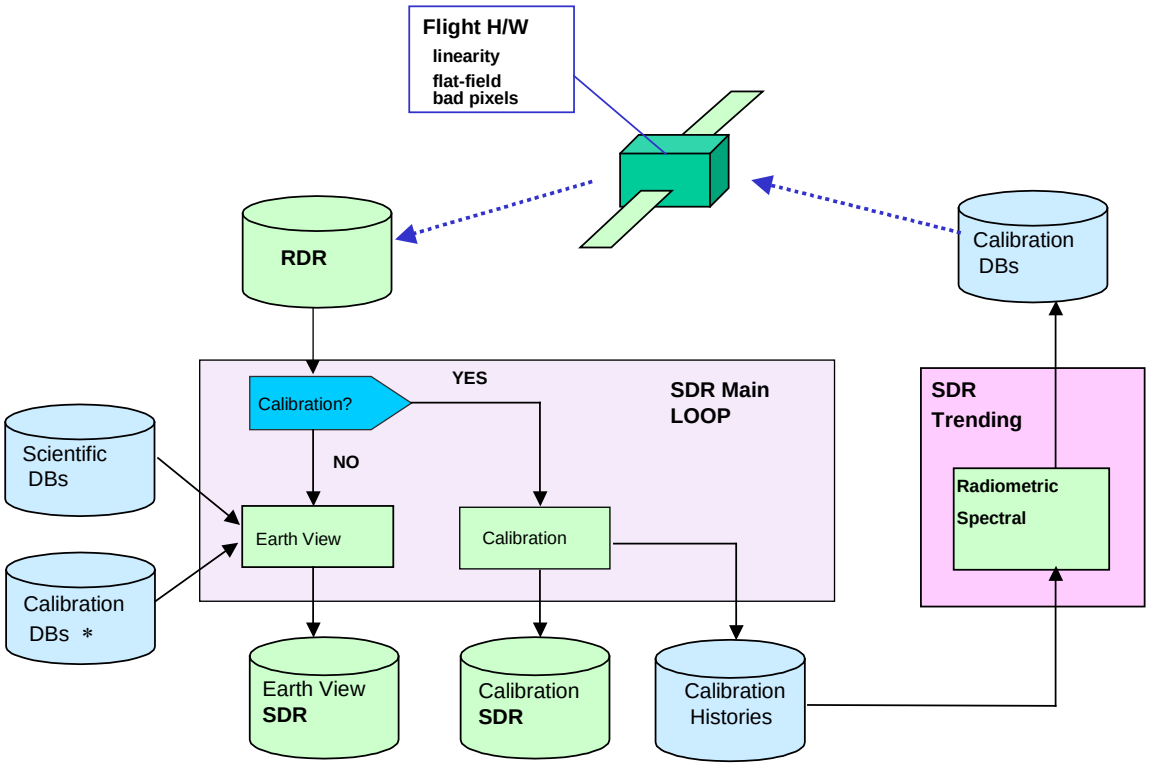

Figure 3.1-1. Schematic Showing SDR Generation

3.1.1 SDR algorithm Inputs and Outputs

The SDR algorithm processes the input RDR data into two separate output SDR files (SDFs): calibration and Earth. The Earth SDF is made available to the retrieval algorithm for further processing. The calibration SDF remains as an archival SDR product. An SDF of either type is a snapshot of the observations and data processing within a particular time.

The SDR algorithm processes individual RDRs of any data type in any data type order, as long the RDRs are time ordered. The SDR algorithm separates the Earth RDRs from the calibration RDRs, processes them separately, and then stores them in separate output calibration and Earth SDFs. The algorithm assumes that all calibration RDRs from a calibration sequence are in the same RDF, though Lamp, Solar, and Dark RDR data can be in separate RDFs from each other, or they can be in the same input RDF. It makes no difference: all calibration RDRs in an RDF are processed and written to a single output calibration SDF. Alternately, the algorithm writes Earth SDRs grouped by day into an SDF for those input RDRs with the same common observation day. Thus, for an orbit spanning two days, the algorithm produces two separate earth SDFs, one for each day.

Each SDF is primarily an archival product containing raw counts, count corrections, measurement precisions, and calibrated values: radiances for Earth and count rate for solar. We designed the earth and calibration SDFs to contain all the information necessary, under normal circumstances, for a retrospective processing of SDF data into EDRs. As such, an SDF contains all calibration factors and identifies the ancillary information needed to convert raw sensor counts to calibrated radiances.

In addition to the two types of output SDFs, the SDR algorithm stores cumulative histories of the calibration observations in a separate set of databases, some of which are used in subsequent SDR processing for trending and signal processing corrections.

The inputs and outputs described in this ATBD are provided in narrative form for a qualitative description of functionality only. For a detailed description of the NP SDR algorithm input and output data files and their contents, please refer to the Operational Algorithm Description Document for the OMPS Nadir Profiler SDR Algorithm Software (D39546).

3.1.1.1 Inputs to the SDR algorithm

The SDR processing of both calibration and Earth data *together* uses the following input sources:

- RDR headers and data records

- Spacecraft diary ephemeris and attitude with times
- BATC generated databases of utilized pixels (sample tables)
- BATC generated timing pattern table
- Band center wavelength table
- Spectral response bandpass shape table
- CCD pixel look angle table
- Sensor diffuser irradiance goniometry characteristics (BRDFs) table
- Linearity correction table
- Radiance and irradiance calibration coefficient tables
- Baseline solar irradiance observed by OMPS early in the mission
- Standard high spectral resolution solar flux
- Wavelength fitting parameters and wavelength shift lookup table
- OMPS Total Column SDR radiances and irradiances
- EDR products from other NPOESS sensors, including:
  1. Atmospheric profiles of temperature and pressure – CrIMSS
  2. Cloud cover fraction – VIIRS
  3. Cloud top pressure – VIIRS
  4. Snow/ice fractional surface coverage – VIIRS
     - Sea Ice Characterization - VIIRS
     - Snow Cover/Depth – VIIRS
  5. Quarterly Surface Type Gridded IP - VIIRS

- Climatological databases, including:
  1. Terrain pressure
  2. Cloud top pressure
  3. Snow/ice surface coverage fraction
  4. UV reflectance
  5. Tropospheric ozone column
  6. South Atlantic Anomaly radiation level

External data, either static climatology values or dynamic EDRs from other NPOESS sensors, are stored in each Nadir Profile SDR record at each spatial location. Actual observed EDR data values, when available, supersede the climatological values. The present version of the NP retrieval algorithm does not utilize external NPOESS EDR information. It is anticipated that future versions may, so they are included in the current SDR algorithm. The co-location of the external EDRs with OMPS data cells is performed as part of SDR processing and is based on time tags and geolocation. The threshold horizontal and vertical cell sizes specified by the VIIRS and CrIS design documents are sufficient for OMPS resolutions.

3.1.1.2 Outputs from the SDR algorithm

The SDR processing creates two types of products: SDFs and calibration databases. The comprehensive list of all the products generated by the SDR software is provided in the Operational Algorithm Description document, the descriptions provided in this

section are only meant to be pointers to the most critical items which deserve discussion in a Theoretical Basis Document. All begin with an ASCII file header containing identifying information. In the case of SDFs, this is known as the major header.

The SDR algorithm writes the following information into the header of each OMPS NP SDR product:

- Spacecraft identification tag
- Sensor identification tag
- SDR product identification tag
- Flight software version
- RDR software version
- SDR software version
- Generation date and time
- Ancillary data file names and version numbers (Timing pattern and Sample Tables)

3.1.1.2.1 Earth - Sensor Data Files (SDFs)

An SDF can cover any length of time, but because down linked RDR data must be sorted and ordered sequentially prior to SDR algorithm processing, the nominal coverage of an operational RDR File (RDF) and its associated SDF is one full orbit. The SDR algorithm processes individual RDRs of any data type in any data type order, as long the RDRs are time ordered. The SDR algorithm separates the Earth RDRs from the calibration RDRs, processes them separately, and then stores them in separate calibration and Earth SDFs.

The Earth SDFs contain all of the Earth view data, observation information, and the state of the Nadir Sensor that the NP retrieval algorithm needs to produce NP IP. An SDF also contains sufficient information to permit a complete reprocessing by the SDR algorithm, if necessary. Thus, uncorrected radiometric counts are included in the file, as well as calibrated radiances in the Earth SDFs. Conversions of the initial sensor status data and geolocation data are unlikely to be repeated, so their precursors are not saved in the SDF. The OMPS Algorithm Development Specification Document (#542808) further describes the SDF contents.

Both Earth and calibration SDF files contain a 1) major header, 2) major record data, 3) minor headers, and 4) minor record data. The first two occur once, at the beginning of an SDF. They include information and data that remain constant for the period covered by the file. A sensor data record (SDR) for a particular observation consists of the minor header and minor record data. There are approximately 160 SDRs in each SDF.

SDF MAJOR RECORD DATA – Earth

The following data are written into the major Earth SDF record:

- Number of SDRs in the SDF file
- Bandcenter wavelength registration for the beginning day of the Earth observations in the SDF
- Calculated solar irradiance flux density at the OMPS wavelengths
- Radiance calibration for the current day of the Earth observations
- Dark current correction data
- Electronics Bias data

MINOR RECORD (SDR) HEADER – Earth

The minor record is associated with a group of spatial data cells representing one report period. Each minor record contains a header and data record. The following information is written in the minor record header:

- Unique SDR identification tag
- Orbit number
- Logical sequence number
- Operation mode
- Date and time at start & end of period
- CCD integration time
- Input RDR data quality flags
- Input RDR header information
- Subsatellite latitude and longitude at start & end
- Spacecraft altitude at start & end
- Solar right ascension at start & end
- Solar declination at start & end
- Spacecraft-centered solar azimuth at start & end
- Spacecraft-centered solar elevation at start & end
- Spacecraft geocentric position (X,Y,Z) and velocity (V_x, V_y, V_z) at start & end
- Spacecraft attitude (difference from nominal; in Roll, Pitch, Yaw) at start & end

MINOR RECORD (SDR) DATA – Earth

The following data are written into the minor data record:

- Data and processing quality flags
- Radiation anomaly flags (SAA, solar eclipse, and sun glint)
- External data source flags
- Sensor status data
- Intra-orbital spectral shift coefficients (unimplemented)

- Field-of-View (FOV) Latitudes, Longitudes for each spatial cell
- FOV angles for solar zenith, satellite zenith, and relative azimuth
- Terrain pressures – climatology database
- Cloud top pressures – VIIRS, *or* climatology
- Cloud coverage fractions – VIIRS *or* flagged as missing
- Snow/Ice cover – VIIRS *or* climatology database
- UV reflectance – climatology database
- Temperature profiles –CrIMSS
- Pressure profiles – CrIMSS
- Raw RDR sensor counts
- Calibrated Earth radiances
- Smear correction data

3.1.1.2.2 Calibration - Sensor Data Files (SDFs)

An output calibration SDF contains all of the sensor calibration data for one RDF dataset. Sensor calibrations include solar, lamp, and dark measurements. If one or more of these is contained in an RDF, a single SDF is produced. The calibration SDF contains sufficient information to permit a complete reanalysis of sensor calibrations. Thus, uncorrected sensor signals are included in the file as well as corrected calibration signals. Conversions of the initial housekeeping data and geolocation data are unlikely to be repeated, so their precursors are not saved in the SDF. The OMPS Algorithm Development Specification Document (#542808) further describes the SDF contents.

As with Earth SDF files, calibration SDFs contain a 1) major header, 2) major record data, 3) minor headers, and 4) minor record data. The first two occur once, at the beginning of an SDF. They include information and data that remain constant for the period covered by the file. A sensor data record (SDR) for a particular observation consists of the minor header and minor record data. The number of SDRs in a file varies with the calibration schedule, but is unlikely to exceed 160.

SDF MAJOR RECORD DATA

The following data are written into the calibration SDF major record:

- Bias correction values
- Dark signal correction values
- Pixel map of current good and bad pixels
- Wavelengths currently used
- Flat Field current values
- Current solar count rate
- Reference solar irradiance
- Number of SDRs in the SDF file

MINOR RECORD (SDR) HEADER – solar, dark, or lamp data

The minor record contains data for one report period. Each minor record contains a header and data record, as well as some associated statistical measurement uncertainties. The following information is written in the minor record header:

- Unique SDR identification tag
- Orbit number
- Logical sequence number
- Operation mode
- Date and time at start & end of period
- CCD integration time
- Diffuser position code
- Input RDR data quality flags
- Input RDR header information
- Spacecraft geocentric position (X,Y,Z) at start & end
- Spacecraft attitude (difference from nominal; in Roll, Pitch, Yaw) at start & end
- Solar right ascension at start & end
- Solar declination at start & end
- Spacecraft-centered solar azimuth at start & end
- Spacecraft-centered solar elevation at start & end
- Subsatellite latitude and longitude at start & end
- Spacecraft altitude at start & end

MINOR RECORD (SDR) DATA – solar, dark, or lamp data

The following data, and some associated statistical measurement uncertainties, are written in the minor data record:

- Data and processing quality flags
- Radiation anomaly flags – SAA and solar eclipse
- External data source flags
- Sensor status information
- Raw RDR counts
- Smear data
- Solar-Orbital Plane Beta angle at start & end
- Goniometric correction factors
- Corrected counts

3.1.1.2.3 Databases

The calibration SDR processing produces an extensive set of databases that are used as input to 1) Earth SDR processing, 2) SDR algorithm trending, 3) generating uplink tables to flight software, or 4) off-line data quality and calibration analyses. All are history databases with the latest information appended to the end of a file. If calibration data is missing from the current RDF, the most recent entries in the calibration databases are used to process the RDR data. The databases are keyed by year and day of year.

Each record of the database histories contains coadded data. When possible, bad pixels are excluded from coadded data, except for dark data, which is used to identify bad pixels. Dark data obtained during the passage of the satellite through the terrestrial SAA are stored separately from other dark data. It is assumed that Lamp data are not acquired through the SAA. Throughout the SDR algorithm description, we refer to these databases by their logical names. The algorithm produces the following direct databases while processing calibration data.

- BIASES – detector electronic offset in counts
- DARKS – detector dark signal in counts
- SAA_DARK – during South Atlantic Anomaly, detected dark signal in counts
- LAMP - lamp signals in counts and count rates
- LINEARITY – detector linearity functional fit
- RAWFLX - corrected solar signal corrected for detector and normalized by the baseline solar signal
- FLUX - same as RAWFLX but corrected for detector spectral shifts
- WMON - bandcenter wavelength shifts relative to the baseline solar measurement

The generation of these primary history databases is described more fully in Section 3.1.3.4., but the record entries for all the above databases are created directly from processed calibration RDFs. Both BIASES and DARKS are updated for every input RDF containing coadded dark RDRs. To permit further data trend analyses, the observation time-averages of the sensor status information in the RDR header, are also stored in the listed databases, except for the LINEARITY database. An initial laboratory characterization of the linearity is stored in the LINEARITY database for the first operational processing of flight data, though if the initial entry is missing, and if input Lamp RDR data are supplied, the algorithm will correct properly subsequent data, because LINEARITY is updated when Lamp data are processed. The remaining databases are updated when Solar RDR data are processed.

From these primary databases, the SDR algorithm also creates a set of derived databases that contain analysis results such as trending. Due to the infrequency of calibration operations, the algorithm relies upon radiometric and spectral calibration values that are extrapolated from trended fits to the actual calibration observations. The

databases contain quantities for each pixel or a binned set of pixels on the CCD image. The generation of these databases is described more fully in Section 3.1.3.5.

- BADPIXELS - bad pixel severity for each pixel on detector
- LINEARITY - detector linearity
- CF_EARTH - radiometric calibration factors for the Earth scene spatial cells
- CF_SOLAR - radiometric calibration factors for the solar illuminated pixels
- WAVELENGTHS - bandcenter wavelengths corrected for solar Doppler shift
- FLATFIELDS - relative multiplication factors for each pixel used in binning for an Earth spatial cell. These are locally normalized to unity for each Earth data cell.

3.1.1.2.4 Uplink Files

The SDR algorithm produces two calibration products for use in creating OMPS NP upload tables. The contents of these tables are processed outside of the SDR algorithm for upload to the flight hardware and software and are used for on-board signal corrections and pixel use and rejection. The LINEAR_UPLOAD file is updated concurrently with LAMP calibration databases, whereas the FLAT_UPLOAD file is updated for each change of day of Earth input RDR data. Flight software tables should be generated using these files, with human-in-the-loop, and it remains an operational decision whether or not to upload new ones. In addition, the SDR algorithm produces bad pixel databases containing information of suspected new bad pixels detected from the new calibration data. These databases are reviewed outside of the operational SDR algorithm, and once these suspected bad pixels are confirmed, the EV_sampletable will be updated for uploading to the flight hardware and software.

It should be emphasized that both bad pixel tables and linearity tables used by the operational SDR algorithm should always be checked for consistency with the flight software. An update to the EV_sampletable LUT or the linearity LUT in the ground processing should not happen unless it has been detected from the earth view RDR engineering data that the flight versions of these tables have been updated. The update to these LUTs is a manual process, and the SDR algorithm is not allowed to update these LUTs on its own. Generation of these files is described further in Section 3.1.3.5.

3.1.2 Earth View Processing

The processing goal is to obtain for each observed Earth spatial data cell, a calibrated Earth radiance spectrum, observation angles, and geolocations, as well as matching NPOESS external data, climatological data, and OMPS Total Column calibrated radiances and irradiances. These constitute the set of data needed by the NP IP algorithm for ozone profile retrievals. **Figure 3.1-2** shows the flow for processing each raw data file (RDF) containing multiple Earth view RDRs. The description that immediately follows is an overview of the processing. Detailed discussions of the processes, corresponding to the individual elements in Figure 3.1-2, are contained in subsections.

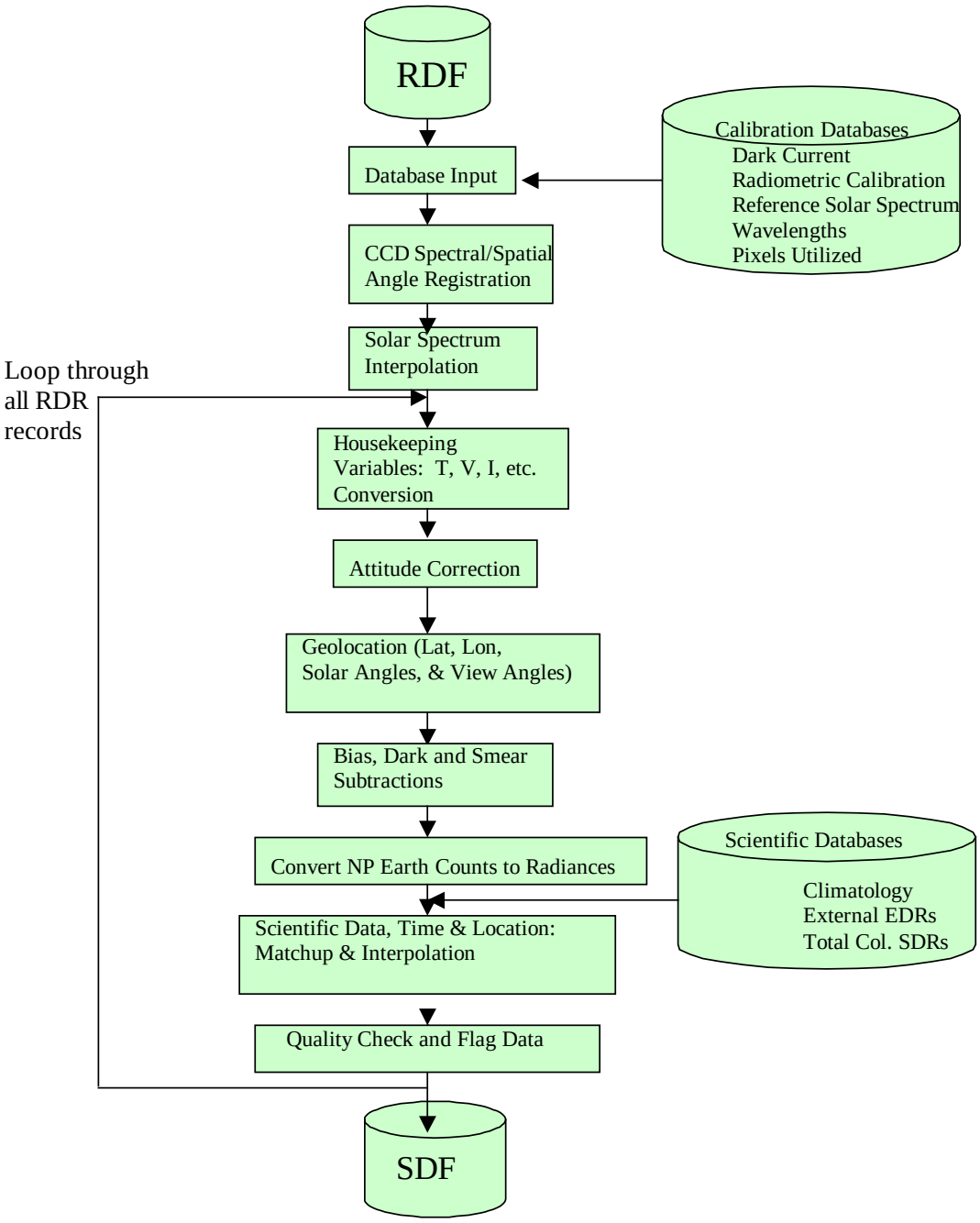

Figure 3.1-2. Schematic showing Earth View SDR generation process

The OMPS NP flight hardware corrects sensor signals for non-linearity and relative pixel response. The NP flight software then bins pixels in the spatial dimension to create a macropixel. A macropixel is typically made up of 93 to 94 individual pixels, except when a bad pixel is excluded. Bad pixel identification is based upon the EV_sampletable LUT. Thus, for each RDF containing Earth data, the algorithm reads the concurrent EV_sampletable, which is always checked to be consistent with the flight software. All ground processing of Earth data excludes bad pixels from the operations, whenever possible. The remaining signal corrections and calibrations are then applied during ground processing of RDRs into SDRs, using pre-computed databases, except for the exposure smear correction, which uses signals accompanying the earth scene data.

At the start of the Earth SDR processing, the NP SDR algorithm reads the CCD map of pixel optical angles, sensor radiometric calibration coefficients, EV sample tables, and ingests an RDF containing the Earth RDRs. Then, for the current day of the Earth RDR data, the SDR algorithm reads both the wavelength database and the Earth radiance calibration factors database, whose values are written into the output SDF major record. Note that the SDR algorithm performs these initial processing steps for different days in an RDF. Therefore, RDFs that contain data from two days are split by day into separate output SDF files.

The remainder of the processing is executed many times: once for each RDR minor record (i.e., set of radiance observations) within an RDF. One input RDR corresponds to one output SDR. After reading the header data from an RDR, the algorithm performs limit checks on both the sensor status data and the CCD data, the flagging results of which are then written into the SDR along with the sensor status data. Next, the algorithm reads the spacecraft diary for attitude and ephemeris and interpolates them to the times of the OMPS RDR observations. With the OMPS mounting angles and attitude deviations, the algorithm obtains the OMPS sensor true attitude, with which it geolocates the Earth spatial data cells by the begin and end observation times. The average geolocation and scattering angles are recorded in each SDR.

At this point, prior to the radiance calibration, the algorithm can perform the optional stray-light correction. Details of stray-light correction are discussed in Section 3.1.2.7**.**

Importantly, the SDR algorithm corrects the initial Earth view signal output from the OMPS sensor by removing bias, dark, and smear signals. With the corrected counts, the algorithm then converts the Earth counts to radiance, using binned calibration constants and radiance calibration factors, as well as the integration time. It should be pointed out that due to the fine structures in the solar diffuser, calibration factors computed from the solar data may not have the desired accuracy to be used in radiance calibration. Therefore, we have added a switch to the algorithm to allow the operator to decide whether to use the calibration factor or not when converting counts into radiances.

Moreover, all external data (climatology, external EDRs, and TC SDRs) are matched in time and location to the NP earth view observations and interpolated, if necessary, in time and space. Finally, the algorithm checks and sets quality flags, particularly for the satellite passing through the South Atlantic Anomaly (SAA) radiation zone, viewing the Earth at solar eclipses, and viewing the Earth at sun glint angles. Additional flags for good pixel percentage, as well as wavelength and radiance ranges are checked and set. After the algorithm processes all RDRs within the RDF, it writes the calibrated Earth radiances and all supporting data into the SDF.

3.1.2.1 Database Input

The following database information is read for use during Earth data processing:

- Macropixel sample table LUT – CCD map of EV macropixels
- EV_sampletable LUT – CCD map of EV macropixels including bad pixels
- SC_sampletable LUT – CCD map of solar calibration pixels
- LED_sampletable LUT – CCD map of LAMP pixels
- Timing pattern LUT – integration time, number of co-adds, and number of frames for each data type (EV, DARL, LAMP,SOLAR)
- Bias signals for both image halves (BIASES)
- Most recent dark signals for each macropixel (DARKS or SAA_DARK)
- Radiometric calibration factors for current day (CF_EARTH)
- Radiometric calibration constants
- Baseline solar irradiance (RAWFLX)
- Bandcenter wavelengths of each macropixel for current day (WAVELENGTHS)
- Detector map of pixel optical angles
- Atmospheric and Surface Climatology (monthly, global grids); space radiation SAA map
- OMPS-TC SDRs (by observation time)
- Other NPOESS EDRs (VIIRS, CRIMSS)

3.1.2.2 CCD Spectral and Spatial Registration

The goal of the registration is to assign a wavelength and two angles for each data cell. The initial laboratory CCD spectral and spatial maps exist for every illuminated CCD pixel. The SDR algorithm bins and averages the laboratory calibration maps for wavelength into the same data samples as Earth data. Because the spectral calibration excludes bad pixels, the registration does not need to adjust for deleted pixels.

The spatial registration contains CCD pixel look angles and is used to compute the pointing direction (unit vectors) of each individual CCD pixel in the sensor cube coordinates. These unit vectors are then combined according to the EV sample table to calculate the overall Line Of Sight (LOS) for each EV macropixel, which is later used by the common geolocation algorithm to geolocate the EV data location.

The wavelengths of the binned Earth data are read from the WAVELENGTHS database. If calibrated wavelengths are missing, the Earth data are flagged accordingly. Slight distortions of the focal plane on the CCD cause the pixel bandcenter wavelengths to vary slowly across the spatial dimension, resulting in different spectral registration for every Earth macropixel. The spectral registration includes a daily correction for instrument-induced spectral shifts, as well as Doppler shifts caused by OMPS satellite motion toward the Sun. We also anticipate that the spectra will be subjected to uncorrected intra-orbital wavelength shifts due to thermal fluctuations. However, thermal models indicate these shifts are within the spectral registration error allocation. We have investigated strategies to characterize these additional shifts, but they are not currently part of the baseline algorithm.

3.1.2.3 Housekeeping Data

Sensor housekeeping data generally include information from thermistors as well as any feedback from mechanical systems, command verification, etc. Most housekeeping data, particularly from thermistors, are telemetered in raw form. The SDR algorithm assumes that the NPOESS processing environment uses predetermined conversion factors provided by the OMPS sensor contractor to convert the housekeeping data into sensor status data that resides in each RDR. These status quantities within an RDR are copied and written by the SDR algorithm into the corresponding output SDR.

3.1.2.4 Solar Irradiance Spectrum

Because the NP IP algorithm uses Earth radiances normalized by solar irradiances as its primary data, each SDF contains a solar irradiance spectrum along with the measured Earth radiances. One should note that neither the SDF radiances nor the SDF irradiances are fully calibrated products. Only the normalized radiances, in which sensor effects and solar flux changes cancel, fulfill that requirement. The SDR algorithm does not compute normalized radiances due to the potential for radiance and irradiance measurements to be measured with different spectral scales. Instead, the algorithm determines the solar irradiance $F^m(\lambda)$ at the time of an Earth observation by correcting the baseline NP solar spectrum $F^m(\lambda^r)$ for subsequent changes in the sensor spectral registration.

The SDR algorithm computes a factor γ for each macropixel during calibration trending in order to estimate $F^m(\lambda)$.

$$F^m(\lambda) = \gamma F^m(\lambda^r) \tag{8}$$

The computation of γ is described in Section 3.1.3.5.9. These factors, registered by day, are read in from the WAVELENGTHS database. The algorithm computes baseline solar irradiance values $F^m(\lambda^r)$ from pre-launch irradiance calibration constants k^j and values T_o read in from the RAWFLX database.

$$F^m(\lambda^r) = k^i T_o \tag{9}$$

The SDR algorithm writes the values $F^m(\lambda)$ into the Earth SDF major record

3.1.2.5 Geolocation

Like other sensors, the geolocation of OMPS SDRs is done in two steps, the sensor specific geolocation and the common geolocation. In the sensor specific geolocation algorithm, which is part of the OMPS NP SDR algorithm implementation, the LOS unit vector in the instrument coordinate is computed from the sensor CCD pixel spatial registration table. Details are discussed in section 3.1.2.5.2. In the second step, the common geolocation algorithm, which is not part of the OMPS SDR algorithm implementation, uses the LOS vectors to compute the projected earth piercing location for each measurement. The actual implementation of the common geolocation algorithm is beyond the scope of this ATBD and if interested, should be referred to the ATBD for the common geolocation algorithm. Nonetheless, the discussion in this section contains information pertinent to the common geolocation and such information is included for reference only.

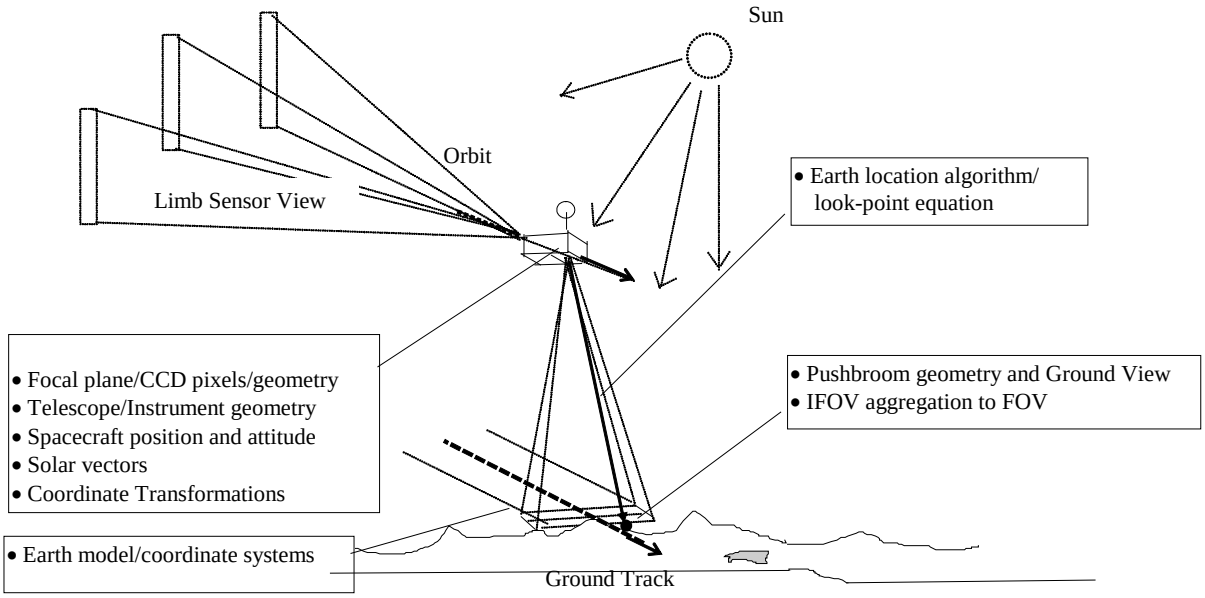

Figure 3.1-3. OMPS geolocation elements

Primary elements of the OMPS geolocation process are shown in Figure 3.1-3. The geolocation algorithm transforms the sensor view angles to the geodetic coordinate system in which geodetic latitude and longitude are expressed. Related parameters, such as solar and satellite zenith angles, used by the SDR and EDR/IP algorithms are calculated within the geolocation algorithm. The following sections describe the theoretical basis for the geolocation algorithm and the implementation approach.

3.1.2.5.1 Coordinate System Definitions

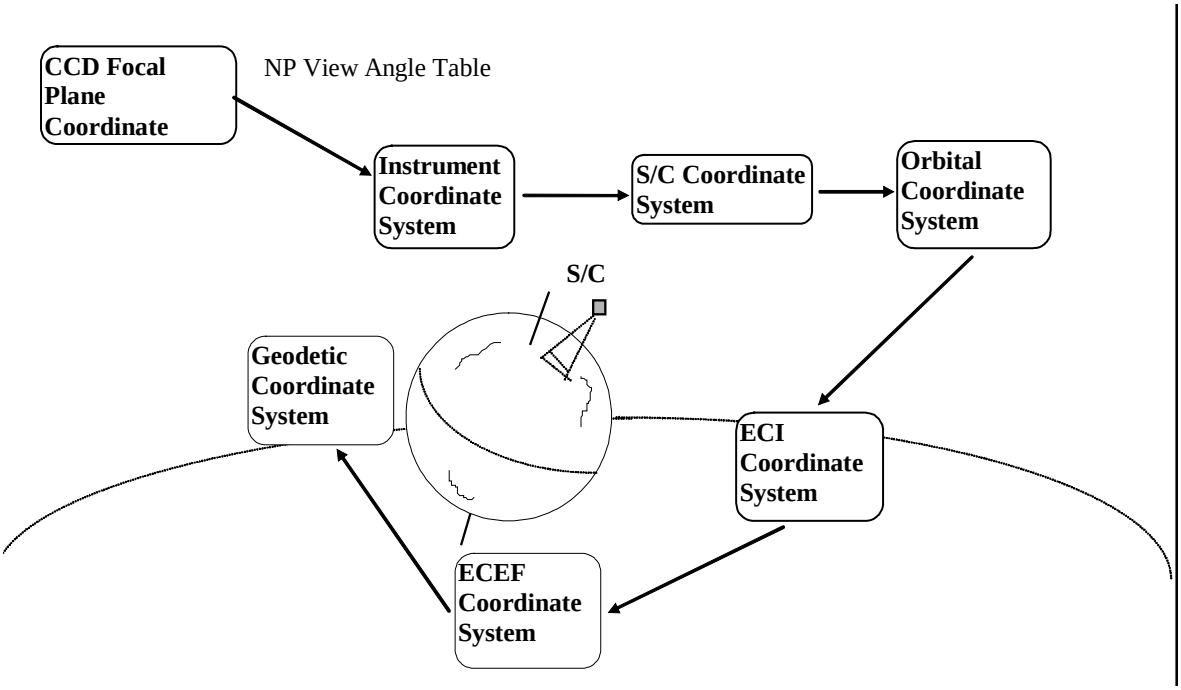

Figure 3.1-4. OMPS geolocation coordinate systems

Figure 3.1-4 displays the coordinate systems used in geolocation along with the typical sequence of coordinate transformations from FOV view angles to geodetic coordinates.

Instrument Coordinate System

The instrument coordinate system (Figure 3.1-5) is the coordinate system in which an image space view vector emanating from the center of a detector or spatial element number and sample time is converted to an object space viewing vector. It is based on the OMPS reference axes defined by the OMPS alignment cube. During preflight testing, the actual alignment of the aft optics/CCD focal plane, and the spacecraft coordinate system to the instrument coordinate system will be measured. This coordinate system is based on preflight measurements of the orientation of the instrument alignment cube.

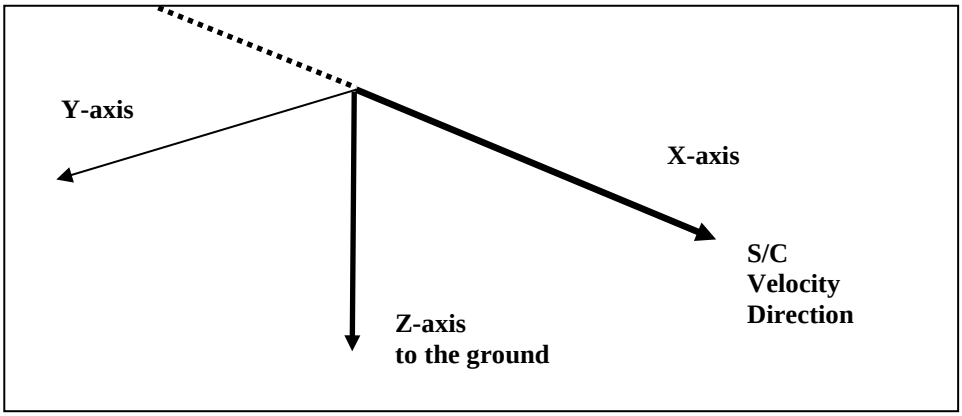

Figure 3.1-5. Instrument Coordinate System

Spacecraft Coordinate System

The spacecraft coordinate system is fixed to the NPOESS spacecraft with its origin at the spacecraft center of mass. The coordinate axes are defined by the spacecraft attitude control system. It is the orientation of this coordinate system relative to the orbital coordinate system that is captured in the spacecraft attitude data.

Orbital Coordinate System

The orbital coordinate system is centered on the satellite and its orientation is based on the spacecraft position in inertial space (Figure 3.1-6). The origin is the spacecraft center of mass with the Z axis pointing from the spacecraft center of mass to the direction perpendicular to the reference ellipsoid. The Y axis is the normalized cross product of the Z axis and the instantaneous (inertial) velocity vector. It corresponds to the direction of the negative of the instantaneous angular momentum vector direction. The X axis is the cross product of the Y and Z axes.

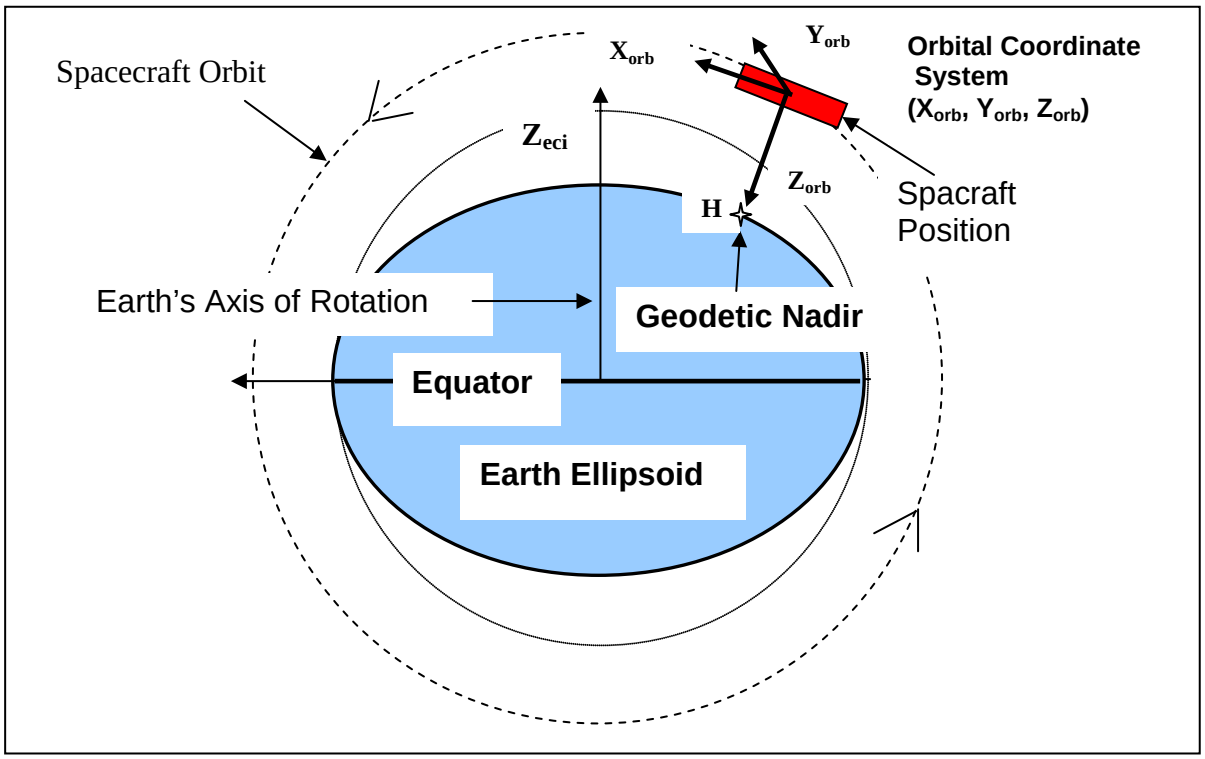

Figure 3.1-6. Orbital Coordinate System

Earth Centered Inertial Coordinate System (ECI)

The Earth Centered Inertial (ECI) coordinate system has its origin at the Earth's center of mass (Figure 3.1-7). The Z axis corresponds to the mean north celestial pole of epoch J2000.0. The X axis is based on the mean vernal equinox of epoch J2000.0. The Y axis is the cross product of the Z and X axes. This coordinate system is described in detail in NIMA, 1997.

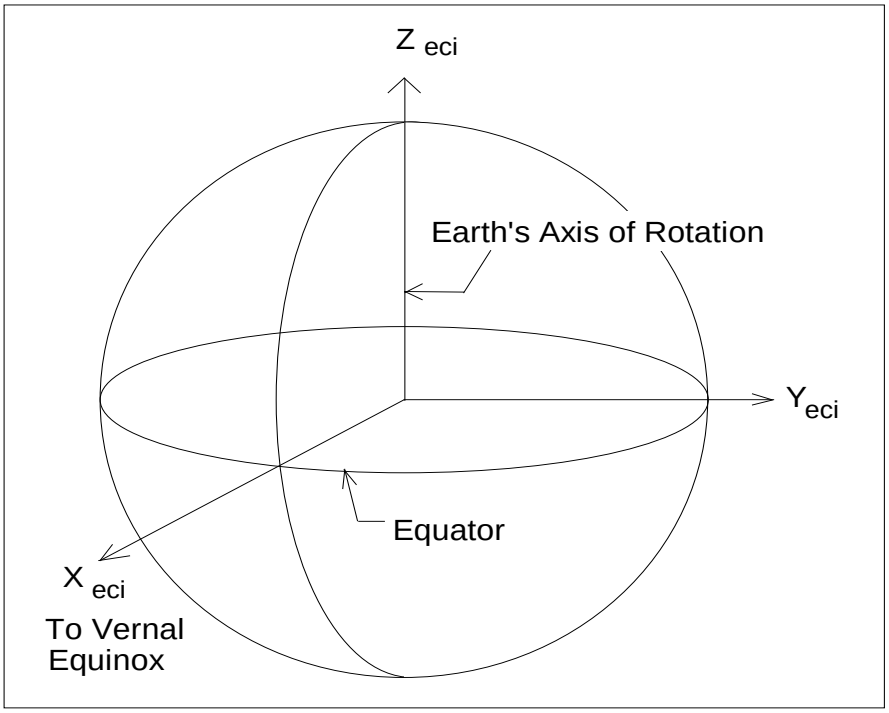

Figure 3.1-7. ECI Coordinate System

Earth Centered Earth Fixed (ECEF)

The Earth Centered Earth Fixed (ECEF) coordinate system has its origin at the center of mass of the Earth (Figure 3.1-8). It corresponds to the Conventional Terrestrial System (CTS) defined by the International Earth Rotation Service (IERS), which is the same as the U. S. Department of Defense World Geodetic System 1984 (WGS84) geocentric reference system. This coordinate system is described thoroughly in NIMA, 1997.

Geodetic Coordinate System

The geodetic coordinate system is based on the WGS84 reference frame with coordinates expressed in latitude, longitude, and height above the reference Earth ellipsoid. No ellipsoid is required by the definition of the ECEF coordinate system but the geodetic coordinate system depends on the selection of an Earth ellipsoid. Latitude and longitude are defined as the angle between the ellipsoid normal and its projection onto the equator and the angle between the local meridian and the Greenwich meridian, respectively. The Earth location data fields in each OMPS SDR will be expressed in the geodetic coordinate system.

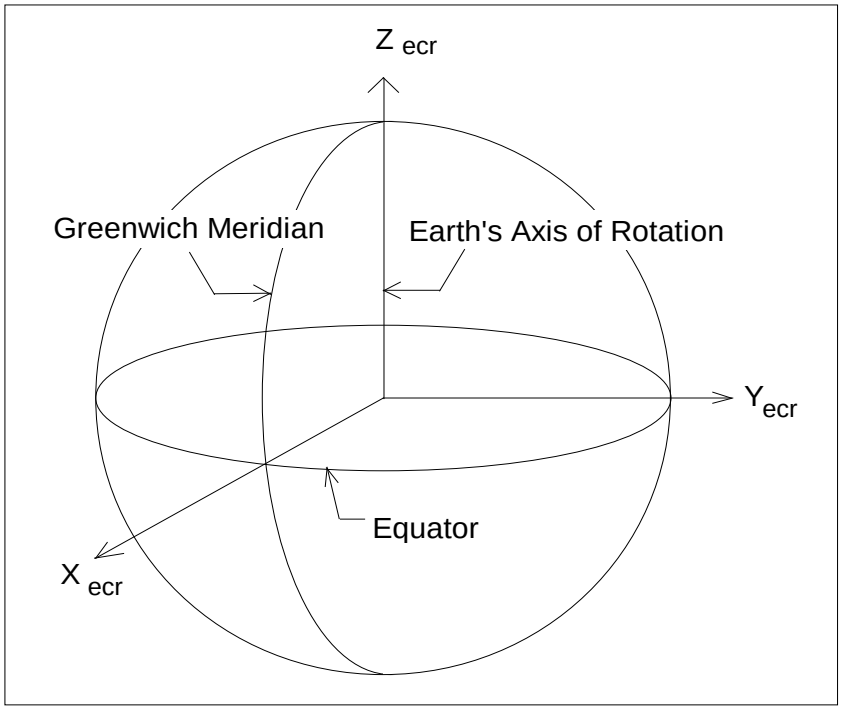

Figure 3.1-8. ECEF Coordinate System

3.1.2.5.2 Coordinate transformations

Focal Plane to Telescope to Instrument Coordinate System

In theory, the view vectors for each of the CCD pixels could be expressed in instrument coordinates with the help of optical ray trace models. Transformation matrices could be developed for each of the optical subassemblies between the focal plane and entrance aperture and then combined to calculate the view vector. This approach is useful when the optical characteristics of a particular subassembly may change on orbit in response to external factors, such as time varying thermal loads. For OMPS, BATC developed a sophisticated sensor/optical model that was used to calculate entrance aperture view angles along with a number of other sensor parameters. While predicted sensor characteristics are useful for SDR and EDR/IP algorithm development and testing, they may lack sufficient fidelity for operational usage. As part of their pre-launch sensor characterization testing, BATC will provide view angle pairs for each of the NP CCD pixels expressed in instrument coordinates.

The optical view angles (α, β) provided by BATC are expressed in the form of rotational angles, and the unit exit vectors are calculated as:

$$u_1 = \sin(\beta)$$

$$u_2 = -\sin(\alpha)*\cos(\beta) \quad (10)$$

$$u_3 = \cos(\alpha)\cos(\beta)$$

Here, α is called by BATC as the azimuth look angle (rotation around the x-axis), and β as the elevation look angle (rotation around the y-axis).

Figure 3.1-9 displays a simplified depiction of the sensor (focal plane and curved mirror) and the projection of the view vectors onto the Earth's surface. Predicted view angles from the sensor model are plotted in Figures 3.1-10 and 3.1-11 as a function of pixel number.

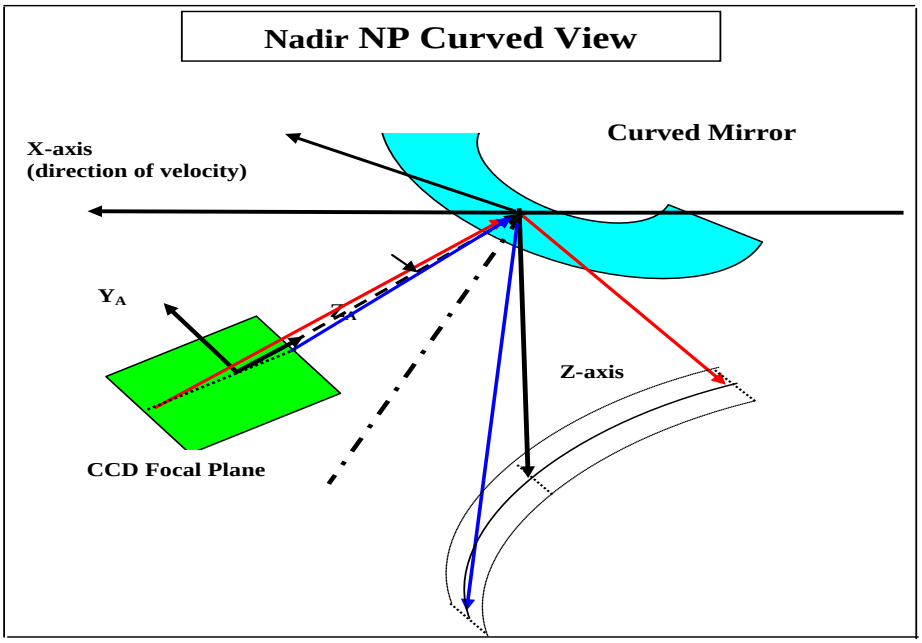

Figure 3.1-9. CCD focal plane to the ground view

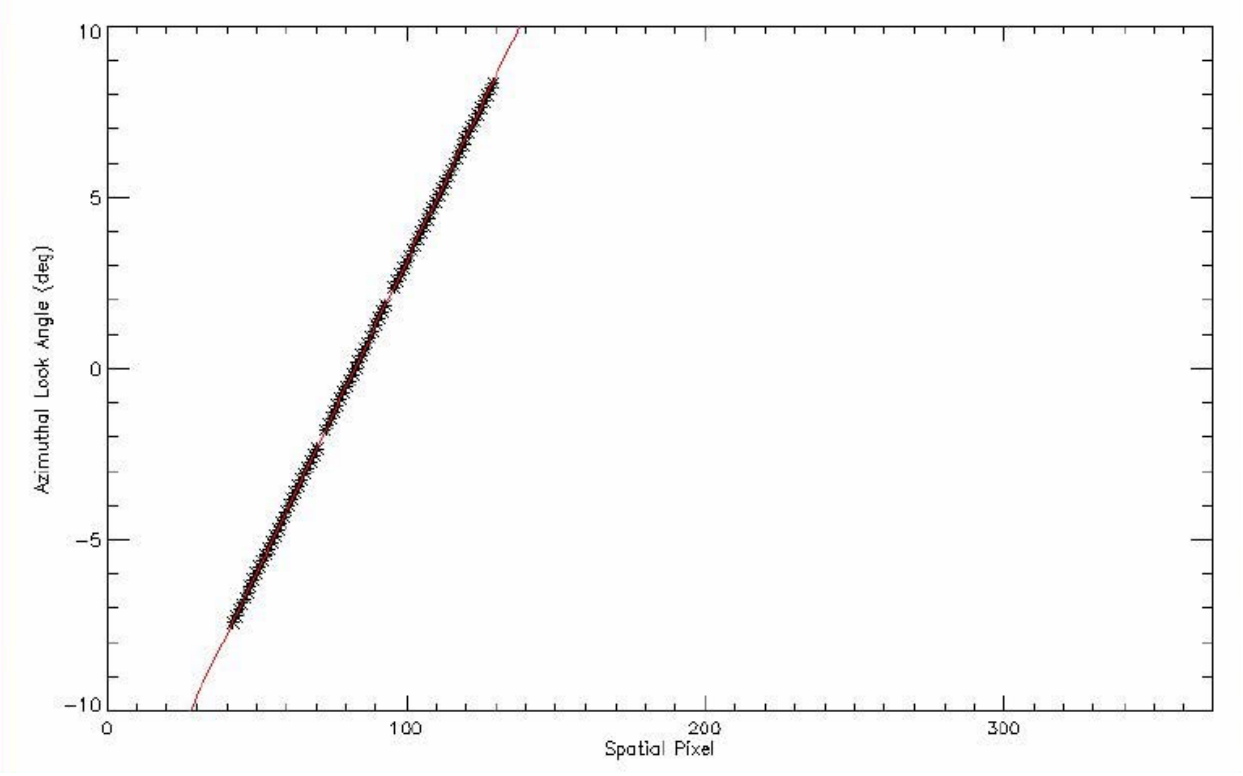

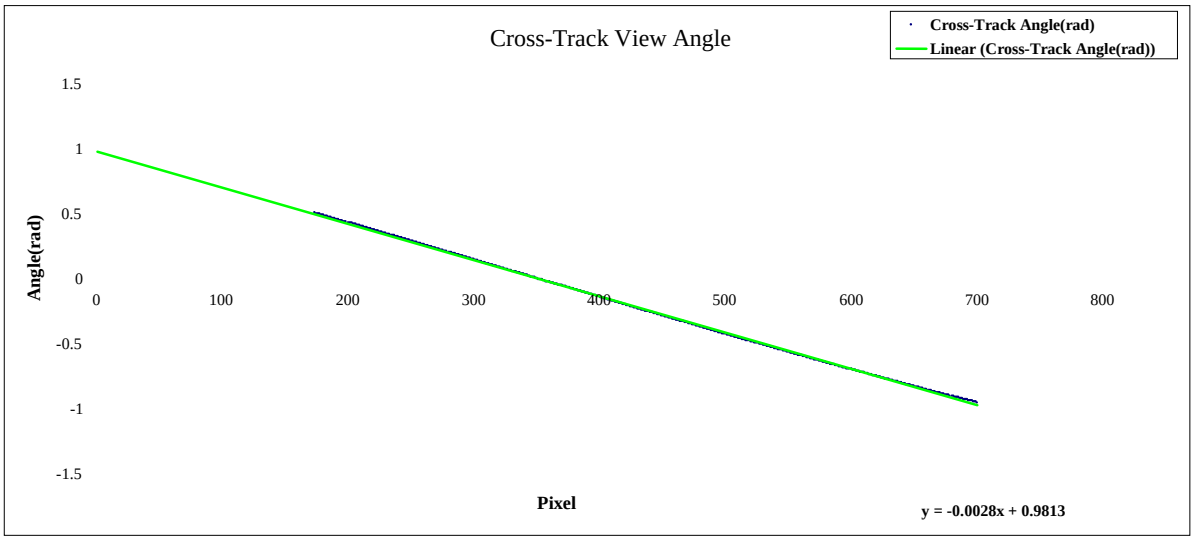

Figure 3.1-10. Cross-Track view angles α

The cross track view angle is nearly linear. The along track view angle variation is significantly nonlinear as can be seen in Figure 3.1-11.

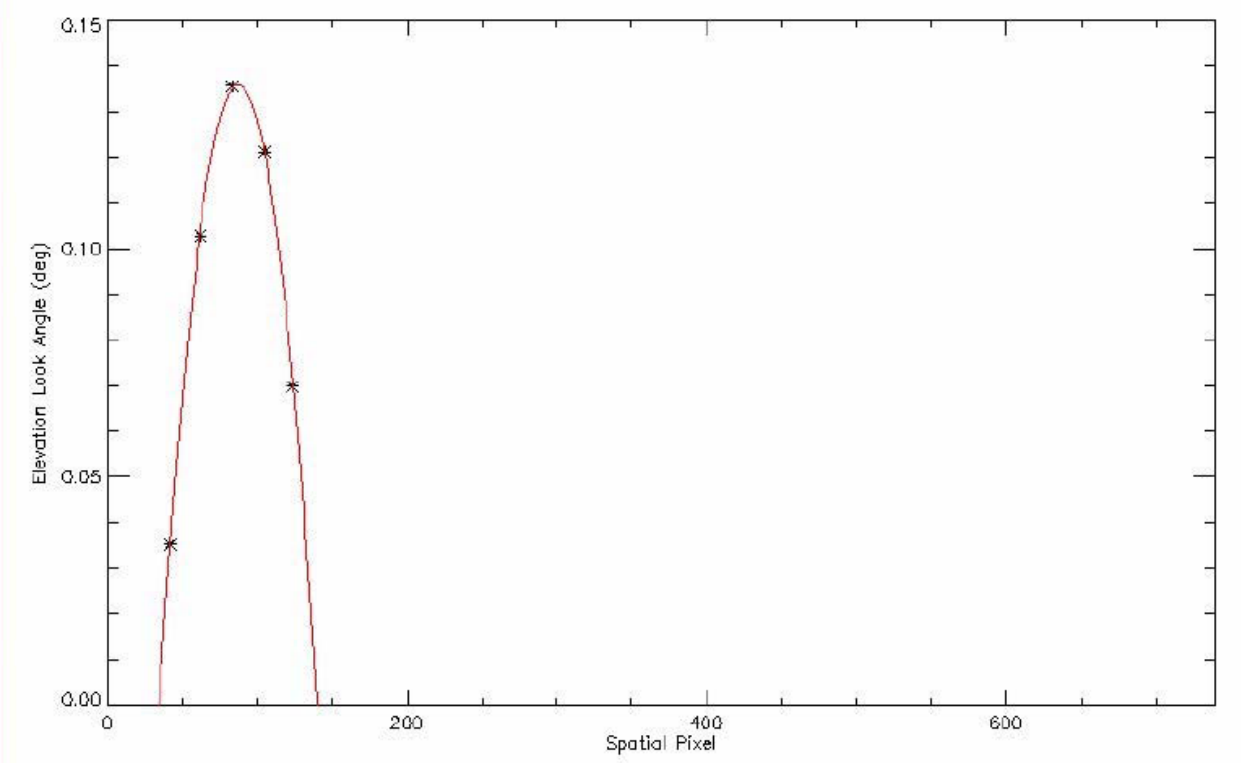

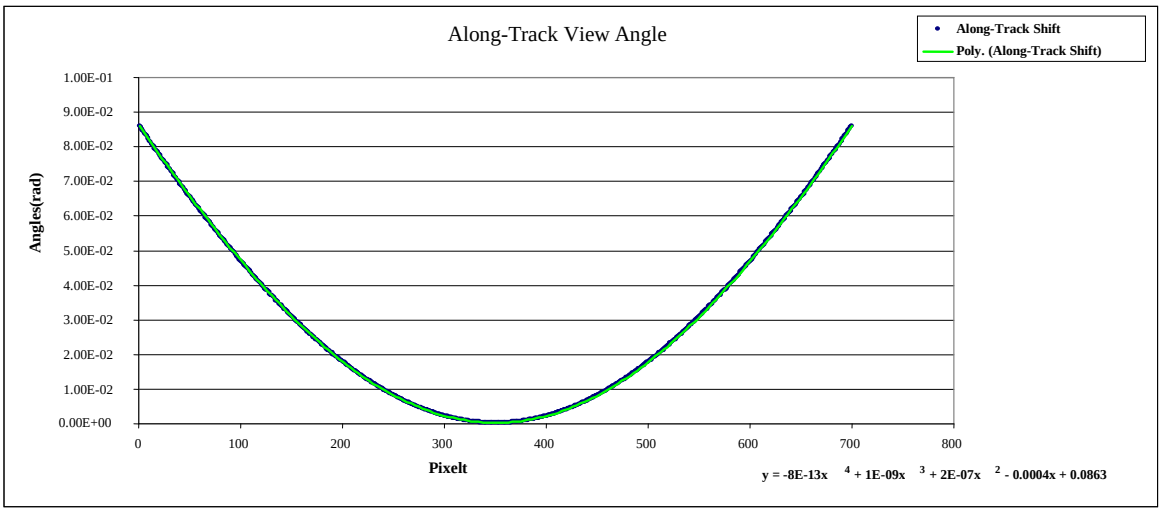

Figure 3.1-11. Along-track view angle β

The along-track view angles in Figure 3.1-11 result in a spatial smile projected on the Earth as shown in Figure 3.1-12 for the TC swath. The NP footprint overlaps the TC swath along the orbital track and only extends 125 km to either side. Consequently, the effect of the spatial smile is much smaller.

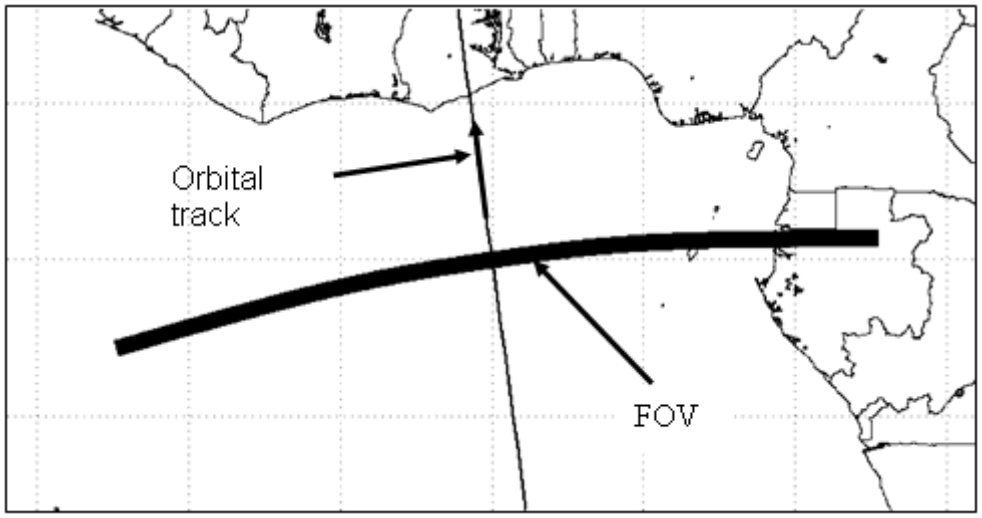

Figure 3.1-12. Ground Trace of TC with respect to spacecraft ground track

Instrument to Spacecraft

For development purposes we assume the transformation matrix between the instrument and spacecraft ($\mathbf{T}_{sc/inst}$) is given by

$$T_{sc/inst} = \begin{bmatrix} 1 & 0 & 0 \\ 0 & 1 & 0 \\ 0 & 0 & 1 \end{bmatrix} \quad (12)$$

These values should be replaced after the sensor has been mounted on the spacecraft and the alignment measured between the sensor and spacecraft reference axes.

Spacecraft to Orbital

The relationship between the spacecraft and orbital coordinate systems is defined by the spacecraft attitude. For NPP and NPOESS attitude information will be provided as a quaternion, which will be converted to Euler angles for use in the SDP Toolkit (ECS Project, 1995). The transformation from spacecraft to orbital coordinates is a three-dimensional rotation matrix, with the components of the rotation matrix being functions of the spacecraft roll, pitch, and yaw attitude angles. The nature of the functions of roll ξr, pitch ξp, and yaw ξy depends on the exact definition of these angles (i.e. how they are generated by the attitude control system). Wertz (1985) requires the proper rotation order to be yaw, roll, and pitch. Since the spacecraft attitude is constantly changing, this transformation is time varying. The transformation matrix is:

$$\mathbf{T}_{\text{orb/sc}} = \begin{bmatrix} \cos\xi_y & -\sin\xi_y & 0 \\ \sin\xi_y & \cos\xi_y & 0 \\ 0 & 0 & 1 \end{bmatrix} \begin{bmatrix} 1 & 0 & 0 \\ 0 & \cos\xi_r & -\sin\xi_r \\ 0 & \sin\xi_r & \cos\xi_r \end{bmatrix} \begin{bmatrix} \cos\xi_p & 0 & \sin\xi_p \\ 0 & 1 & 0 \\ -\sin\xi_p & 0 & \cos\xi_p \end{bmatrix}$$

$$\mathbf{T}_{\text{orb/sc}} = \begin{bmatrix} \cos\xi_y\cos\xi_p - \sin\xi_y\sin\xi_r\sin\xi_p & -\sin\xi_y\cos\xi_r & \cos\xi_y\sin\xi_p + \sin\xi_y\sin\xi_r\cos\xi_p \\ \sin\xi_y\cos\xi_p + \cos\xi_y\sin\xi_r\sin\xi_p & \cos\xi_y\cos\xi_r & \sin\xi_y\sin\xi_p - \cos\xi_y\sin\xi_r\cos\xi_p \\ -\cos\xi_r\sin\xi_p & \sin\xi_r & \cos\xi_r\cos\xi_p \end{bmatrix} \quad (13)$$

Orbital to ECI

The relationship between the orbital and ECI coordinate systems is based on the spacecraft's instantaneous ECI position and velocity vectors. The rotation matrix to convert from orbital to ECI can be constructed by forming the orbital coordinate system axes in ECI coordinates:

p - spacecraft position vector in ECI

v - spacecraft velocity vector in ECI

H - geodetic nadir location on ellipsoid in ECI

p' - vector **H** → **p**

$\mathbf{T}_{eci/orb}$ - rotation matrix from orbital to ECI

$\hat{\mathbf{b}}_3 = -\mathbf{p}'/|\mathbf{p}'|$ (nadir vector direction)

$\hat{\mathbf{b}}_2 = \hat{\mathbf{b}}_3 \times \mathbf{v} / |\hat{\mathbf{b}}_3 \times \mathbf{v}|$ (negative of angular momentum vector direction)

$\hat{\mathbf{b}}_1 = \hat{\mathbf{b}}_2 \times \hat{\mathbf{b}}_3$

$\mathbf{T}_{eci/orb} = \left[\hat{\mathbf{b}}_1 \quad \hat{\mathbf{b}}_2 \quad \hat{\mathbf{b}}_3\right]$

ECI to ECEF

The transformation from ECI to ECEF coordinates is a time varying rotation due primarily to Earth rotation but also containing more slowly varying terms for precession,

astronomic nutation, and polar wander. The ECI to ECEF rotation matrix can be expressed as a composite of these transformations:

$$\mathbf{T}_{ecef/eci} = \mathbf{ABCD} \quad (59)$$

A - Polar Motion

B - Sidereal Time

C - Astronomic Nutation

D - Precession

Each of these transformation terms is described in detail in NIMA, 1997.

ECEF to Geodetic

The relationship between ECEF and geodetic coordinates can be expressed simply in its direct form (NIMA, 1997):

$$x = (N + h)\cos(lat)\cos(lon)$$

$$y = (N + h)\cos(lat)\sin(lon)$$

$$z = (N(1 - e^2) + h)\sin(lat)$$

$$N = a/(1 - e^2 \sin^2(lat))^{\frac{1}{2}}$$

$$e^2 = 1 - \frac{b^2}{a^2}$$

where:

(x, y, z) - ECEF coordinates

(lat, lon, h) - Geodetic coordinates

N - Ellipsoid radius of curvature in the prime vertical

e - Ellipsoid eccentricity

a, b - Ellipsoid semi-major and semi-minor axes

Unfortunately, there is no closed form solution for the inverse problem (which is the problem of interest here). Latitude and height must be solved iteratively for points that do not lie on the ellipsoid surface.

3.1.2.5.3 Geolocation algorithm

(Note: Discussion in this section is for reference only, and may not reflect what is implemented in the common geolocation algorithm. In particular, the SDP Toolkit is not used in the operational common geolocation algorithm.)

A basic Earth ellipsoid intersection algorithm yielding geodetic altitude and longitude consists of the following steps.

Given an object viewing vector $\mathbf{u}_{\text{inst}}$ in the instrument coordinate system, (calculated from viewing angles or viewing vectors provided by BATC) and a corresponding time *t*, the algorithm proceeds as follows:

1. Compute the required coordinate transformations:

1a. Get instrument-to-spacecraft alignment matrix $\mathbf{T}_{\text{sc/inst}}$. [Construct the instrument-to-spacecraft alignment matrix based on the time *t* if a time varying model is needed.]

1b. Interpolate the spacecraft attitude to time *t* and construct the spacecraft to orbital coordinate transformation matrix $\mathbf{T}_{\text{orb/sc}}$.

1c. Interpolate the ECI spacecraft position $\mathbf{P}_{\text{eci}}$ and velocity $\mathbf{V}_{\text{eci}}$ to time *t* and construct the orbital to ECI transformation matrix $\mathbf{T}_{\text{eci/orb}}$.

1d. Construct the ECI to ECEF rotation matrix $\mathbf{T}_{\text{ecef/eci}}$ from the sampling time *t*.

1e. Construct the composite transformation matrix:

$$\mathbf{T}_{\text{ecef/inst}} = \mathbf{T}_{\text{ecef/eci}}\mathbf{T}_{\text{eci/orb}}\mathbf{T}_{\text{orb/sc}}\mathbf{T}_{\text{sc/inst}} \quad (14)$$

2. Transform the viewing vector and spacecraft position vector to the ECEF coordinate system:

2a. Rotate the viewing vector $\mathbf{u}_{\text{inst}}$ to the ECEF coordinate system:

$$\mathbf{u}_{\text{ecef}} = \mathbf{T}_{\text{ecef/inst}}\,\mathbf{u}_{\text{inst}} \quad (15)$$

2b. Rotate the spacecraft position vector to the ECEF coordinate system:

$$\mathbf{p}_{ecef} = \mathbf{T}_{\text{ecef/eci}}\,\mathbf{p}_{\text{eci}} \quad (16)$$

3. Intersect the ECEF viewing vector with the WGS84 Earth ellipsoid

Note: These equations do not account for the travel time of light or for aberration due to spacecraft motion or relativistic effects. These effects cause a systematic bias of 7 m at nadir and 14 m at the edges of the scans.

3a. Re-scale the viewing vector $\mathbf{u}_{ecef} = (u_1, u_2, u_3)$ and satellite vector $\mathbf{p}_{ecef} = (p_1, p_2, p_3)$ using the ellipsoid semi-major *a* and semi-minor *b* axis dimensions (*a, a, b*):

$$\mathbf{u}' = \begin{bmatrix} u_1 / a \\ u_2 / a \\ u_3 / b \end{bmatrix} \qquad \mathbf{p}' = \begin{bmatrix} p_1 / a \\ p_2 / a \\ p_3 / b \end{bmatrix}$$

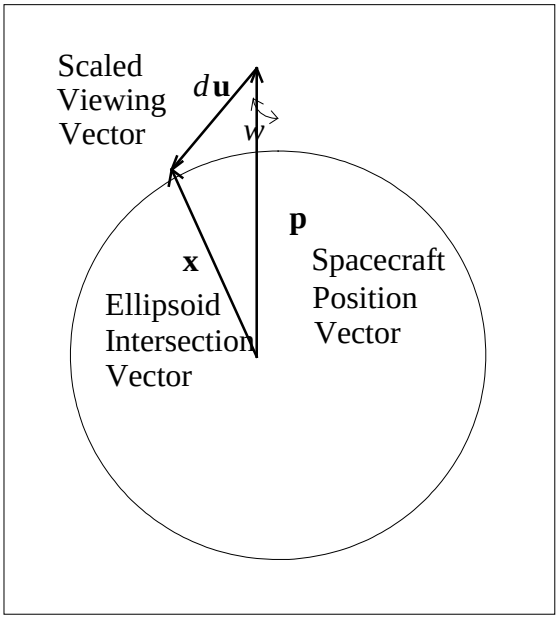

Figure 3.1-13. Ellipsoidal viewing vector intersection

Note:

$$\mathbf{x}' = \begin{bmatrix} x_1 / a \\ x_2 / a \\ x_3 / b \end{bmatrix}$$ - the unknown ground point vector (re-scaled)

3b. Solve for the scaling *d* of $\mathbf{u}'$ which intersects the unit sphere:

From the law of cosines:

$$|\mathbf{x}'|^2 = |d\,\mathbf{u}'|^2 + |\mathbf{p}'|^2 - 2\,|d\,\mathbf{u}'|\,|\mathbf{p}'|\cos(w)$$

Using the dot-product, the cosine of the acute angle *w* between $\mathbf{u}'$ and $-\mathbf{p}'$ is:

$$\cos(w) = -(\mathbf{u}'\cdot\mathbf{p}')/(|\mathbf{u}'||\mathbf{p}'|)$$

By definition $|\mathbf{x}'| = 1$ so:

$$1 = d^2|\mathbf{u}'|^2 + |\mathbf{p}'|^2 + 2d|\mathbf{u}'||\mathbf{p}'|(\mathbf{u}'\cdot\mathbf{p}')/(|\mathbf{u}'||\mathbf{p}'|)$$

Simplifying and rearranging:

$$d^2|\mathbf{u}'|^2 + 2d(\mathbf{u}'\cdot\mathbf{p}') + |\mathbf{p}'|^2 - 1 = 0$$

This can be solved for *d* using the quadratic formula:

$$d = \frac{-(\mathbf{u}'\cdot\mathbf{p}') - \sqrt{(\mathbf{u}'\cdot\mathbf{p}')^2 - |\mathbf{u}'|^2\left(|\mathbf{p}'|^2 - 1\right)}}{|\mathbf{u}'|^2}$$

This is the smaller of the two solutions for *d*, the intersection closest to the satellite. If the solution is not real, then there is no intersection.

3c. Use *d* to compute $\mathbf{x}'$ and $\mathbf{x}$:

$$\mathbf{x}' = \mathbf{p}' + d\,\mathbf{u}'$$

$$\mathbf{x} = \begin{bmatrix} x'_1\,a \\ x'_2\,a \\ x'_3\,b \end{bmatrix} = \begin{bmatrix} (p'_1 + d\,u'_1)a \\ (p'_2 + d\,u'_2)a \\ (p'_3 + d\,u'_3)b \end{bmatrix} = \begin{bmatrix} p'_1\,a + d\,u'_1\,a \\ p'_2\,a + d\,u'_2\,a \\ p'_3\,b + d\,u'_3\,b \end{bmatrix}$$

$$\mathbf{x} = \mathbf{p} + d\,\mathbf{u}$$

4. Convert the ECEF ellipsoid pierce point to geodetic coordinates (special case direct solution):

$$lon = \tan^{-1}\left(\frac{x_2}{x_1}\right) \tag{17}$$

$$lat = \tan^{-1}\left(\frac{x_3/\left(1-e^2\right)}{\sqrt{x_1^2 + x_2^2}}\right) \tag{18}$$

$$h = 0 \tag{19}$$

3.1.2.5.3.1 SDP Toolkit application

We adopted and modified the SDP Toolkit (SDPTK) to implement the steps outlined in the previous section. A spacecraft tag was created for the NPOESS series of spacecraft and the orbital simulation program was modified to improve the modeling accuracy of the program for an NPOESS orbit. The majority of the spacecraft platforms SDPTK was designed for employ geocentric pointing with geocentric referenced Euler attitude angles. The TRMM spacecraft is an exception to this in that it employs geodetic pointing and geodetic referenced Euler angles. The SDPTK orbital simulation program is capable of modeling this situation and SDPTK can input geodetic referenced attitude Euler angles and accurately calculate the spacecraft to orbital coordinate transformation with the help of an additional transformation subroutine. NPOESS is a geodetic pointing spacecraft with attitude information provided to the SDR algorithm in the form of an ECI to SC rotation quaternion. Since the Euler angles are not input from an external source, nor do we have any requirements to report Euler angles in any particular form, we are free to choose the Euler angle representation. Selecting the native mode of SDPTK, geocentric referenced Euler angles, simplifies the simulation and geolocation process and reduces the number of computations. Therefore, for NPOESS, the orbital simulation program was modified to simulate geodetic pointing and report attitude as geocentric referenced Euler angles. Attitude angles input to SDPTK in this form can be used without any additional transformations.

Because the NP geolocation process is nearly identical for Earth view and calibration data, it is performed with a single subroutine. A table of sensor view angles representing the view angles at the center of each pixel are input. For Earth view data, view angles corresponding to the center of field of view are used. Since calibration data is not spatially averaged, view angles for each individual pixel are used. Viewing vectors are formed from the view angles and the instrument to spacecraft transformation is applied using the nominal mounting matrix. SDPTK subroutine pgs_csc_subsatpoint is called to calculate the sub-satellite latitude and longitude. This call initiates input of the satellite ephemeris (position and velocity) and attitude data that is then interpolated to the requested time. The SDPTK subroutine pgs_csc_getfov_pixel takes as input the unitized view vectors and returns the geodetic latitude and longitude. Other SDPTK subroutines are called to calculate solar right ascension, declination, and elevation

angles. These are written into the SDR, but spacecraft-centered solar angles calculated by the algorithm are *not* written to an Earth SDR because the EDR processing does not require them.

Geolocation is performed for the beginning and ending time of an observation. The final geolocation is an average of the beginning and ending geolocations

3.1.2.5.3.2 Spacecraft diary data conversion

Time

Time tags applied to RDR data and to ephemeris/attitude data are assumed to follow the same definitions and format conventions. It is anticipated that spacecraft time will be reported in CCSDS 301.0-B-2 segmented time code (CDS) with time code epoch January 1, 1958. Generic SDPTK time conversion routines were modified to convert spacecraft time to International Atomic Time (TAI) with a January 1, 1993 epoch (TAI93) and to UTC time. Because the SDPTK native time is TAI93 and the SDR algorithm uses TAI93 internally, the NPOESS time code is converted to TAI93 immediately after the RDR header is input.

Ephemeris

The spacecraft diary ephemeris data, satellite position [meters, ECEF] and velocity {meters/second, ECEF], is converted to units usable by the SDPTK [meters and meters/second, ECI] and in a form acceptable by the standard SDPTK data input routines before RDR processing begins. The conversion is performed with the SDPTK routine pgs_csc_ecrtoeci. The converted ephemeris information is input to the SDR algorithm during RDR processing with the regular SDPTK data input routines.

Attitude

The spacecraft diary attitude information is also converted to a form usable by the SDPTK. The spacecraft diary provides attitude information in the form of a quaternion representing the transformation matrix from J2000 ECI to the spacecraft attitude determination frame approximating the spacecraft body frame. Following the notation for transformation matrices used in preceding sections, the attitude quaternion is expressed as $Q_{\text{sc/eci}}$. Given the time and location of the spacecraft, the SDPTK routine pgs_csc_getorbtoeciquat can be used to calculate $Q_{eci/orb}$. The orbital to spacecraft transformation is computed by multiplying the two quaternions together to yield,

$$Q_{sc/orb} = Q_{\text{sc/eci}} Q_{\text{eci/orb}} \tag{20}$$

The complex conjugate (or inverse) of $Q_{sc/orb}$, yields $Q_{orb/sc}$, which is used with the SDPTK routine pgs_csc_quattoeuler to compute geocentric referenced Euler angles (3-1-2 order).

It is anticipated that for NPP ephemeris data will be reported once per second while NPOESS data will be reported once every ten seconds. For both spacecraft, attitude quaternions will be reported every half second. Because the quaternion to Euler angle conversion requires colocated ephemeris data, the ephemeris data must be time interpolated to the higher resolution attitude time grid. The ephemeris data interpolation is performed with a third order method taken from the SDPTK ephemeris interpolation routine that requires four ephemeris points.

The SDPTK orbsim inputs are currently configured to simulate ephemeris and attitude data in one day granules. SDPTK will accept larger granules, such as a month's worth of data or smaller granules, such as a single orbit of data. Larger granules will increase search time within the granule while the smallest granule must contain four points.

3.1.2.6 Signal Corrections

Prior to radiometric calibration, raw signals from the detector are subject to corrections. Specifically, electronic bias *B*, CCD dark current D_{Jk}, and observational smear Ss_k must be removed from the observed macropixel counts O_{Jk} for binned row *J* (spatial) and column *k* (spectral) to obtain the corrected counts C_{Jk} for each macropixel *Jk*:

$$C_{Jk} = O_{Jk} - B - D_{Jk} - S_{Sk} \tag{21a}$$

In (21a), the dark current is also subject to bias correction, and the smear S_{Sk} is subject to both bias and dark corrections:

$$D_{Jk} = \sum_{j=N_D,N_J} \frac{t_E}{t_D}(D_{jk} - B_D) \tag{21b}$$

$$S_{Sk} = \left(S_k - B\right) - \sum_{j=1,N_S} \frac{t_E}{t_D}(D_{jk} - B_D)] \tag{21c}$$

where t_E and t_D are integration time for the earth data and dark data, respectively; D_{jk} and S_k are, respectively, the observed dark and smear without correction; macropixel row J includes micropixels between row N_D to N_J; smear of column k includes row *1* through N_S; and B_D denotes the bias for the dark data, which may or may not be the same as B. Combining (21a-c):

$$C_{Jk} = O_{Jk} - \sum_{j=N_D,N_J} \frac{t_E}{t_D}\left(D_{jk} - B_D\right) - \left[S_k - \sum_{j=1,N_S} \frac{t_E}{t_D}\left(D_{jk} - B_D\right) \right] \quad (21)$$

In (21), all counts except for the bias have been previously corrected for linearity. The bias correction for the observed dark, B_D, is determined from the measurements of serial over-clock pixels when acquiring the dark data. The bias correction for the earth and smear data (B in 21a & 21c) can be similarly determined. However, because the true smear S_{Sk} is much smaller than dark, which in turn is orders of magnitude smaller than bias, the corrected smear S_{Sk} (21c) derived from measurements with noise can be inaccurate, unstable, and even become negative. On the other hand, the same bias is subtracted from both the earth and smear data, making its value irrelevant to the corrected earth count C_{Jk}. Therefore B is absent from (21).

Prior to coadding the Earth data, the NP flight software applies linearity corrections based upon results of the lamp calibration processing. The split frame architecture of the NP CCD does not cause any difficulties for signal corrections because only one half is used. Because all CCD pixels (even the CCD smear rows) contain dark and bias signals, the algorithm must remove the signals prior to any smear correction.

The electronics bias is always present as an addition to the photometric counts. Unlike other data, the bias is independent of image exposure time and is read from special pixels at the edge of the solar RDRs and stored after calibration processing in the BIASES database. The SDR algorithm during Earth processing reads the BIASES database for the most current values and subtracts the weighted average of the bias values from the Earth data raw counts. In addition, the bias removal also takes into account the number of measurements co-added before the earth view and calibration images being downlinked to the ground.

The dark signal on the OMPS CCD results when electrons are thermally emitted into the conduction band of pixels in the active and storage regions. The dark signal effectively adds offset counts to the photon-generated pixel counts. Dark signal measurements are normally made during the night side of the orbit with the entrance aperture of the sensor blocked, though the algorithm separates dark data taken outside the SAA from those

data taken within the SAA, because the dark current can be expected to increase during an SAA passage. Similarly, the dark current during Earth observations can potentially increase beyond normal. SAA exposure values below 10% of maximum exposure are considered to be normal data for both Earth and dark RDRs.

During calibration processing, and prior to Earth SDR processing, the SDR algorithm characterizes and stores the normal dark signal for each pixel and identifies and stores bad pixel information. To increase the signal to noise, the normal dark data, summed cumulatively in time for the entire RDF duration, are written into a DARK database. Dark SAA data defined as at least the 10% level and greater are not summed, but stored individually in the separate SAA_DARK database along with their SAA exposure values. During Earth data processing, the SDR algorithm reads the latest processed dark data of the appropriate type, even when they were determined from subsequent measurements in the orbit.

For normal Earth data, normal dark data are subtracted. For Earth data acquired during SAA, the SDR algorithm searches and reads the SAA_DARK database for data with a similar level of SAA exposure. If one is lacking, normal dark data are used instead. Whatever the origin of the final dark data used to correct the Earth data, the algorithm bins the dark data pixels into dark macropixels, excluding bad pixels, which were identified in the EV sampletable. The SDR algorithm then subtracts the binned dark data from the corresponding Earth radiometric macropixel value in order to correct the Earth signal for sensor dark current.

At the conclusion of each detector integration period the CCD quickly shifts the electrons from the active to the storage region (parallel transfer). Photons collected in the active pixels during this transfer period are referred to as the smear signal. For a temporally constant radiance scene, even a spatially heterogeneous one, the smear signal is the same in all pixels in a column. The smear signal is measured by re-reading multiple edge rows of CCD pixels that were already read from their primary signal, thereby capturing smear signal produced during the re-reading. These rows are binned to a single row for each CCD half by the flight software. The SDR algorithm subtracts the dark- and bias-corrected smear signal from the observed Earth data to obtain signal-corrected counts, ready for radiometric calibration.

3.1.2.7 Straylight Correction

Ground test data, analysis and simulations show that the stray light contamination of the OMPS NP sensor is compliant to the < 2% requirement as a global average. Simulations using a data set designed to represent global conditions were conducted by BATC to demonstrate compliance. The results show that the sensor meets the requirement for a global average (weighting various conditions of clear/cloudy, ozone amount, latitude, etc.), however the NP exceeds requirements under conditions of concern to science and the public. Actual performance of the sensor will not be known

until on-orbit validation tests are conducted to estimate the levels of stray light contamination present in earth scenes.

A new stray light correction module has been added to the NP SDR algorithm to remove stray light contamination in order to meet the NP IP performance requirement specifications. The correction is based on the stray light correction approach implemented for the LP SDR algorithm. The EV counts *C* are binned into 14 spectral regions:

$$C_{JK}^{m} = \sum_{k} C_{Jk}^{m}$$

where *J* represents the J^{th} spatial macro pixel, *K* represents the binned K^{th} spectral region, *m* indicates that this is measurement, and *k* represents the unbinned k^{th} spectral channel. The binning is mostly for the benefit of reducing computational burden. Note, OMPS NP has a single macropixel.

The binned signal is then multiplied with the pre-computed stray light correction matrix to estimate the stray light contamination, ΔC_{lm}, in the binned count C_{lm} for macro pixel (*l,m*):

$$\Delta C_{lm} = \sum_{J,K} C_{lmJK} C_{JK}^{c}$$

where the 4-D matrix operator C_{lmJK} is pre-computed from the measured sensor point-spreading-function (PSF). The superscript *c* indicates that this is the stray-light corrected quantity, which is not known initially but are estimated by iteration:

$$\begin{aligned}
&C_{lm}^{0} = C_{lm}^{m} \\
&\Delta C_{lm}^{c} = 0 \\
&for\ i = 1, n_iteration \\
&\quad C_{lm}^{i} = C_{lm}^{i-1} - \Delta C_{lm}^{c} \\
&\quad C_{JK}^{i} = \sum_{k} C_{Jk}^{i} \\
&\quad \Delta C_{lm}^{c} = \sum_{J,K} C_{lmJK} C_{JK}^{i} \\
&end\ for
\end{aligned}$$

Where superscript *m* and *c* denote measured and stray light corrected counts, *0, i,* and *i-1* denote iteration, and *n_iteration* is a pre-defined parameter of maximum number of iteration. Default value for *n_iteration* is 2.

There is no out of range (OOR) stray light contamination from OMPS NP sensor. After the spectral stray light contaminations have been computed, they are removed from the measured counts to get the stray-light corrected counts for each and every channel:

$$C_{lm}^{c} = C_{lm}^{m} - \Delta C_{lm}$$

3.1.2.8 Radiometric Correction

Following the signal processing, the algorithm computes calibrated radiances using corrected earth-view counts, integration times, pre-launch radiance calibration constants, and time-dependent radiometric calibration factors (see Section 3.1.3.5.4). Prior to binning the individual pixels into a spatial cell macropixel, the flight software applies flat field corrections to pixel counts in order to correct for the non-commutative additions of counts from varying pixel sensitivities. Since the mean correction applied to each macropixel is 1, the Earth-View (EV) branch of the ground SDR algorithm ignores this preliminary calibration by the flight software (see flat field discussion in Section 3.1.3.5.5).

The algorithm computes Earth radiances I^m_{Jk} for each macropixel (*J,k*) by dividing the corrected counts C_{Jk} (Equation 21) by the integration time t_{int} and applying the corrections described in Section 3.1.3.1.

$$I^m_{Jk} = \frac{C_{Jk} k^r_{Jk} A_{Jk}}{t_{\text{int}}} \tag{22}$$

Counts are converted to radiances using pre-launch radiance calibration constants k^r_{jk}.

The SDR algorithm sums the constants over the pixels *j,k* in each macropixel J,*k*, including only pixels identified as good in the EV sample table. The algorithm then corrects for changes in sensor response using radiometric calibration factors A_{Jk} read from CF_EARTH. These calibration factors have already been corrected for spectral shifts. If current calibration factors are missing, the latest older calibration factors are used, and this is noted in the Earth data quality flags. If the switch for calibration factor correction is set to false, then the calibration factor is re-set to 1, regardless its value in the CF_EARTH database.

3.1.2.9 Match-up with Total Column SDR

The OMPS NP and TC sensor fields of view are designed to coincide with a high degree of accuracy. Therefore the NP SDR algorithm ignores the small differences in timing, boresighting, and point spread functions that cause scene mismatch. The Nadir Suite design is such that the 5 central TC data cells have the same cross-track field of view when combined as the single NP cell. Since the NP and TC sensors share the telescope of the Nadir Suite, their along-track fields of view are nearly identical. The NP report period is planned to be exactly 5 times that of the TC (38 sec. and 7.6 sec., respectively), so 5 consecutive TC report periods comprise a single NP data cell, when the TC data are combined.

3.1.2.10 External Data Match-up

Each SDR contains EDR information from VIIRS and CrIMSS, if available. The geophysical quantities from each are listed in Section 3.1.1.1. EDR information will overwrite existing climatological values if available. In the event that an EDR parameter has been flagged as having poor quality, those data will not be used. EDR information will require minimal additional processing. Atmospheric profiles, however, are binned to the Umkehr layers defined in Table 2.3-2.

Following geolocation of OMPS NP radiance data, external EDR quantities will be read in for the correct latitude, longitude and time. The threshold horizontal and vertical cell sizes specified by the VIIRS and CrIS SRDs for the EDRs listed in Section 3.1.1.1 are sufficient for OMPS. Because OMPS NP, VIIRS, and CrIS are nadir viewing sensors, the data are obtained nearly simultaneously. Thus, measurement collocation is determined solely by spatial considerations.

The CrIMSS swath width encompasses the NP cells. Cell sizes range from 14 to 40 km. CrIMSS provides profiles of temperature and pressure with varying HCS depending on the observing conditions and varying vertical reporting intervals depending on the pressure level. lists the CrIMSS EDRs required for use in the NP SDR algorithm. Note that the Horizontal Cell Sizes (HCS) were taken from the NPOESS System Specification, DOC SY15-0007, Rev N, September 12, 2008.

Table 3.1-1 CrIMSS Horizontal Cell Size

EDR	HCS	Measurement Range
Temperature versus Pressure Profile		180 – 335 ºK
Clear - Nadir	14 km	
Cloudy - Nadir	40 km	
Pressure versus Altitude Profile		10 to 1050 mb
		in 1 km altitude steps

Because there are multiple CrIMSS observations within the NP footprint, the CrIMSS data are selected within the OMPS NP footprint using the criteria described below and then averaged. These selection criteria are as follows:

- For each of the CrIMSS profiles matching the OMPS NP observation time, define a quantity, Δlat, as the absolute difference between the latitude of the NP

observation and the latitude of the CrIMSS observation. Repeat this analysis for the longitude of the NP and CrIMSS measurements.

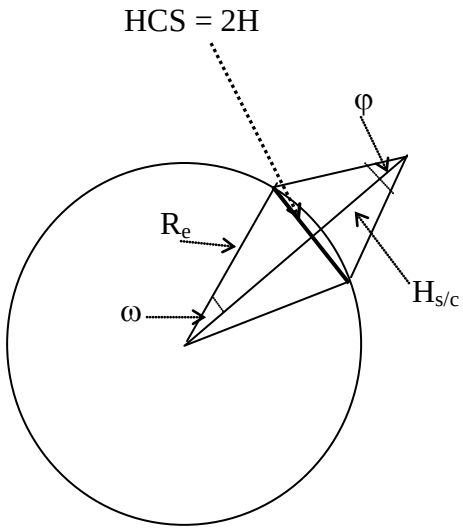

Figure 3.1-14. CrIMSS External Data Match-up

- Define an earth-centered angle, ω, in terms of the Nadir Profile (NP) Horizontal Cell Size (HCS). See the Figure 3.1-14.

  φ = OMPS swath FOV angular coverage/(number of NP horizontal cells)/2

$$\varphi = NP\_scale/2$$

$$\omega = \sin^{-1}\{ (H_{s/c} \cdot \tan(\varphi/2)) / R_e \}.$$

- Define an earth centered angle, β (similar to ω), related to the difference in both longitude and latitude on the earth's surface between two points:

$$\beta = \cos^{-1}\{ \cos(\Delta long) \cdot \cos(\Delta lat) \} \quad (23)$$

- Accept as match all CrIMSS profiles with latitude and longitude satisfying

$$\beta \leq \omega. \quad (24)$$

- Repeat for all the CrIMSS profiles, found within the time match.

- Keep track of all the accepted CrIMSS profiles.
- Average the final profiles into corresponding Umkehr layers.
- Average the matching profiles.

Similarly the VIIRS swath width encompasses all the NP cells. The VIIRS cell sizes range from 0.8 to 25 km. Table 3.1-2 lists the VIIRS EDRs required for use in the NP SDR algorithm. Note that the Horizontal Cell Sizes (HCS) were taken from the NPOESS System Specification, DOC SY15-0007, Rev N, September 12, 2008.

Table 3.1-2 VIIRS Horizontal Cell Size

EDR	HCS	Measurement Range
Cloud Top Pressure		50 to 1050 mb
Edge of Swath	25 km	
Nadir	5 km	
Sea Ice Characterization	Ice Concentration	1/10 to 10/10
Clear	2.4 km	
All Weather	20 km	
Nadir	0.8 km	
Worst Case	3.2 km	
Snow Cover		0 – 100% of HCS
Clear – Nadir	0.8 km	
All Weather	20 km	

Since there are multiple VIIRS observations within the NP footprint, the VIIRS data are selected within the OMPS NP footprint using the same criteria as described above for the matching CrIMSS observations within the OMPS NP footprint.

- For each of the VIIRS observations matching the OMPS NP observation time, define a quantity, Δlat, as the absolute difference between the latitude of the NP

observation and the latitude of the VIIRS observation. Repeat this analysis for the longitude of the NP and VIIRS measurements.

- Define an earth-centered angle, ω, in terms of the Nadir Profile (NP) Horizontal Cell Size (HCS). See the Figure 3.1-14.
- Define an earth centered angle, β (similar to ω).

$$\beta = \cos^{-1}\{ \cos(\Delta long) \cdot \cos(\Delta lat) \} \quad (25)$$

- Accept as match all VIIRS observations with latitude and longitude satisfying

$$\beta \leq \omega. \quad (26)$$

- Repeat for all the VIIRS observations found within the time match.
- Keep track of all the accepted VIIRS observations.
- Average the matching observations.

3.1.2.11 Data Quality Checks

Based on the current bad pixel values, the Earth processing calculates the percentage of good pixels out of the total number of pixels on the fully sampled CCDs image and writes the percentage as a quality flag in the output RDF. This is a basic first assessment of the data quality.

Using the geolocation data for the beginning and end of each observation, the algorithm relies on NPOESS processing to identify if the satellite ground track during an observation crosses the SAA and to supply the correct value from a static SAA map of relative radiation exposure from maximum. Using this percentage, the OMPS SDR algorithm flags an entire Earth scene FOV for SAA exposure. All other data types are also flagged for SAA level. For example, if the calculated exposure is 45% the data are flagged as exceeding 40% but not 50%. Flagging in 10% exposure gradations with an 80% maximum is adequate.

The SDR algorithm computes a median radiance over all wavelengths for each spatial cell. If the median is greater than a parameterized permitted value, the algorithm now flags, as a ratio of median value to allowed value, the spatial cell as containing some anomalously bright radiance. The SDR algorithm also should perform more localized transient hot pixel detection by comparison of Earth pixels with nearest neighboring pixels. A cubic spline, or similar smooth regression, should be performed along each row *J* (i.e. spectrally) for each data cell. The splined region should not exceed 2 nm. A gradated flag, similar to that used for the SAA, should be used to indicate the percent by which the measured radiance exceeds that computed from the spline. Macropixels that

have lower than expected radiances should not be flagged by this algorithm. Currently, this checking is not implemented in the operational code.

Using an almanac of Solar eclipses by the moon, the algorithm expects the NPOESS processing to check the latitude and longitude of the Earth data for the presence of a solar eclipse at each Earth spatial cell. If the data cell lies within an eclipse, the algorithm flags the SDR for eclipses.

Specular reflections of sunlight off water surfaces is a geophysical situation not properly incorporated in the EDR radiance tables. When the sun glint condition is met, water reflects much of the solar irradiation at a solar zenith angle θ_o into the sensor field of view at a satellite zenith angle θ. Waves diffuse the reflection, creating a range of angles for which sun glint produces an error. This includes reflections out of the principal plane, i.e. relative azimuth angle $\varphi \neq 0°,180°$. The SDR algorithm is coded for checks for sun glint for each of the 96 spatial pixels using the following equation for the co-scattering angle Φ.

$$\Phi = \cos^{-1}\left[\left(\cos\theta_o \cos\theta + \sin\theta_o \sin\theta\right)\cos\varphi\right] \leq 30^\circ \quad (27)$$

The algorithm identifies the surface type as water using the surface category. The surface category is currently not stored in the climatology UV reflectance database, so the algorithm expects the glint flag to be passed by the NPOESS processing, which has the same criteria as that given in the above equation.. The glint flag is set when the condition in Equation 27 is met and water covers at least 25% of the FO.V

The algorithm also compares the minimum and maximum derived wavelengths for each Earth data cell with pre-launch parameterized limits for minimum and maximum. The limits are based on extending, by a parameterized wavelength interval, the extrema of all the wavelengths of the initial laboratory scale. If the current assigned wavelengths for an Earth data cell exceed the extrema, the cell is flagged as suspect.

Data quality checks of the calibration data for the SAA and Eclipse are the same as for Earth data, though sun glint checks are not needed for the calibration data.

3.1.3 Calibration

The calibration concept for the OMPS Nadir Profile sensor follows closely that of TOMS and SBUV/2. The TOMS calibration procedures are described in Jaross, et al.,1995, Seftor et al., 1997, and McPeters, et al., 1998. The implementation for OMPS has been described in ICSR-8092402. The use of diffusers is described in ICSR-8110501.

Backscatter ultraviolet (BUV) instruments measure the response to solar irradiance by deploying a ground aluminum diffuser plate to reflect sunlight into the instrument. The three-diffuser system aboard TOMS reduces the exposure and degradation of the

diffuser used for the solar measurements and allows calibration through comparison of signals reflected off diffusers with different rates of exposure. An identical concept is employed on OMPS, but only two diffusers are used because mechanical design differences obviate the need for the third diffuser. The diffusers, designated Working and Reference, are arranged around an annulus so that a given diffuser can be rotated into view on demand. The full NP FOV is covered with the central diffuser position.

The Reference diffuser is exposed for one solar measurement sequence every 6 months, and the Working diffuser is exposed every week. The Working diffuser is the primary sensor calibration diffuser. Periodic comparisons with Reference diffuser solar measurements are used to detect changes in the Working diffuser.

3.1.3.1 Theoretical Basis: Radiometric Calibration

Conceptually, the calibration of measured Earth radiance and solar irradiance may be considered separately. We note that they are not, separately, calibrated quantities for OMPS NP, because the BUV technique cannot distinguish between solar flux changes and sensor response changes. The measured Earth radiance in a single pixel can be written as a function of the corrected instrument counts in the following way:

$$I^m_{jk}(t) = \frac{C^r_{jk} k^r_{jk}}{\tau_{jk}(t)} \tag{28}$$

where

$I^m_{jk}(t)$ = derived Earth radiance for pixel (j,k)

$C^r_{jk}(t)$ = radiance counts, corrected by initial signal corrections algorithms

$k^r_{jk}(t)$ = radiance calibration constant (from pre-launch calibration)

$\tau_{jk}(t)$ = pixel response changes ($\tau(t=0) = 1$)

The measured solar irradiance, F^m_{jk}, can be written as:

$$F^m_{jk}(t) = \frac{C^i_{jk} k^i_{jk}}{g\,\rho(t)\,\tau_{jk}(t)} \tag{29}$$

where

$C^i_{jk}(t)$ = irradiance mode counts (corrected) of pixel j,k

$k^j_{jk}(t)$ = irradiance calibration constant (from pre-launch calibration)

$\tau_{jk}(t)$ = sensor throughput changes ($\tau(t=0) = 1$)

$\rho(t)$ = solar diffuser plate reflectivity ($\rho(t=0)$ = 1)

g = relative angular irradiance response (goniometry) of the sensor

The constants k^r and k^i are not accurately determined separately in flight. The primary quantity measured by BUV sensors, and from which ozone is derived for the Nadir Profile sensor, is the normalized radiance $I^m(t)/F^m(t)$. The advantage of this approach is that sensor throughput changes τ affecting both Earth and solar measurements cancel in the ratio. The expression for normalized radiances becomes:

$$\frac{I^m_{jk}}{F^m_{jk}} = K_{jk}\frac{C^r_{jk}}{C^i_{jk}} g\,\rho(t) \tag{30}$$

where K_{jk} is a combined calibration constant for normalized radiances, often referred to as the Albedo Calibration Constant. This and g are determined in pre-launch calibrations. Because the sensor changes affecting both the Earth and solar measurements cancel in the ratio, the diffuser plate reflectivity, $\rho(t)$ is the quantity that is critical for the time-dependent calibration of the normalized radiances.

Monitoring of diffuser reflectivity is carried out periodically by deploying the Reference diffuser. The initial deployment frequency will be once every 6 months, and may decrease once adequate statistics of Working diffuser change $\rho(t)$ are obtained. A more detailed discussion of diffuser monitoring follows below. Diffuser deployment frequencies are described in ICSR-8110501. We expect several percent changes in the Working diffuser. Though we do not expect these changes to significantly affect ozone, our plan is to provide for corrections for diffuser change once the change exceeds a threshold amount. The threshold value will be determined based upon the resulting ozone error.

The expression for normalized radiances $I^m(t)/F^m(t)$, given in Equation 30, implies that time-dependent calibrations (apart from diffuser changes) are obtained by merely computing the ratio of sensor radiance signal to sensor irradiance signal. But this is not possible, since solar irradiance measurements are obtained only once per week. The solution is to characterize changes in the solar signal in order that the ratio can be computed as though irradiance measurements had been simultaneous with Earth radiance measurements. This is performed via trending and extrapolation algorithms, which are discussed in Section 3.1.3.5.

3.1.3.2 Theoretical Basis: Diffuser Degradation

The multi-diffuser approach to diffuser monitoring relies upon the fundamental assumption that all changes in diffuser reflectance at the sensor wavelengths are a result of solar exposure. No significant changes occur while the diffuser is stowed. Observations of diffuser reflectance change from TOMS, SBUV, and SBUV/2 (Jaross et

al. (1998b) show that the primary mechanism for reflectance decreases seems to be photo-deposition of outgassed contaminants. There is no evidence for significant degradation of either a stowed or exposed diffuser surface in the absence of UV radiation. Therefore, the diffuser degradation rate will be a function of the solar measurement frequency. Previous instruments show some evidence that initial rates depend on the diffuser material (Hilsenrath, 1994), but in the long term, contaminants and UV exposure appear to be the dominant parameters (Hall, 1994).

In the multi-diffuser approach to calibration employed by OMPS a quantity derived from solar calibrations is the Working to Reference signal ratio

$$r = \frac{W}{R} \tag{31}$$

where W and R represent the mean signals from the Working and Reference diffusers, respectively, normalized to their baseline (initial post-launch) calibration values. A small fractional change in the value of this ratio, due to the degradation of either surface or a relative goniometric error, is then written as

$$\frac{dr}{r} = \frac{dW}{W} - \frac{dR}{R} \tag{32}$$

The multi-diffuser calibration approach relies on the assumption of exposure-dependent degradation of the flight diffusers. As discussed in ICSR-8110501, almost all evidence indicates that this assumption is valid. This implies

$$W = f(t_W) \qquad R = f(t_R) \tag{33}$$

where *f(t)* is an arbitrary function of the exposure time *t*. The differential changes are then

$$\frac{dW}{W} = \frac{f'(t_W)}{f(t_W)} dt_W \qquad \frac{dR}{R} = \frac{f'(t_R)}{f(t_R)} dt_R \tag{34}$$

Since a solar measurement sequence is the same for Working and Reference surfaces, exposure times can be rewritten in terms of the number of Working and Reference measurements, n_W and n_R.

$$\frac{t_R}{t_W} = \frac{dt_R}{dt_W} = \frac{n_R}{n_W} \tag{35}$$

Results from TOMS Cover diffusers indicate that degradation is truly an exponential process (see ICSR-8110501). In the specific case where *f(t)* is an exponential, the change in the working surface reflectance as a function of the change in the quantity *r* is

$$\frac{dW}{W} = \frac{n_W}{n_W - n_R}\frac{dr}{r} \tag{36}$$

For situations where the number of Working measurements far exceeds the number of Reference measurements, as with OMPS, the Working change is nearly equal to the change in the ratio of diffuser surfaces. Any uncertainty ε_r in the value of *r* translates via this relationship to an uncertainty in *W*.

$$\frac{\varepsilon_W}{W} = \frac{n_W}{n_W - n_R}\frac{\varepsilon_r}{r} \tag{37}$$

It is the uncertainty in *W* that ultimately determines the long-term calibration uncertainty.

The value of ε_r is actually a time-dependent quantity because, assuming Gaussian statistics, it varies roughly as $\varepsilon_r = \sigma_r/\sqrt{n_R}$. The current operations schedule calls for Reference measurements every 6 months. Thus there will be 2 values of *r* derived per year. Each data point will have a variance σ^2_r associated with it. We will employ linear regression to these data of the form

$$\ln(r) = b \cdot t_R \tag{38}$$

to determine the Working degradation at a time *t*. An uncertainty ε_W can be estimated (see Bevington, for instance) at a time *t* using σ_r and the proposed exposure schedule.

$$\frac{\varepsilon_W}{W} = \frac{n_W}{n_W - n_R}\sigma_b \cdot t \qquad \sigma_b^2 = \frac{1}{\Delta}\sum^{n_R}\frac{1}{\sigma_r^2} \qquad \Delta = \sum_i^{n_R}\frac{1}{\sigma_r^2}\sum_i^{n_R}\frac{t_R^2}{\sigma_r^2} - \left(\sum_i^{n_R}\frac{t_R}{\sigma_r^2}\right)^2 \tag{39}$$

We note that the uncertainty does not depend on the rate *b* of degradation. Each value σ_r depends upon several factors, but is predominantly related to the errors in the goniometric corrections applied to the solar data. Provided that the relationship

$$\frac{\varepsilon_W}{W} > \frac{dW}{W} \tag{40}$$

holds, we do not intend to apply a correction for Working surface degradation.

3.1.3.3 Theoretical Basis: Wavelength Registration

The algorithm's calibration processing determines spectral shifts of the bandcenter wavelengths during the mission, by periodically comparing the OMPS observed solar spectrum with a standard solar spectrum. Before fitting the observed spectrum with the model spectrum, the algorithm first corrects the wavelengths for Doppler shifts induced by motion between the sun and satellite and convolves the standard solar spectrum by the sensor bandpass wavelength response. The best fit model yields the wavelengths. By extrapolating in time from recent solar wavelength calibrations (see Section 3.1.3.5.6), the algorithm predicts the bandcenter wavelengths for the terrestrial observations until the time of the next solar wavelength calibration. The bandcenters are recorded in each Earth SDF.

The sensor bandpass, often referred to as the slit function, is important in model fitting but also because the EDR Algorithm must convolve the slit function with the laboratory ozone spectral cross sections in order to accurately measure profile ozone. The SDR algorithm assumes that the slit functions for the NP data cells are properly characterized prior to launch. It also assumes that modal values of those functions, the bandcenter wavelengths, are properly established as of the time of the baseline solar measurement. Thus the initial wavelengths, bandpasses, and observed baseline solar spectrum define the baseline wavelength scale.

During the spectral fitting, the standard solar spectrum is convolved with varying FWHM NP pre-launch slit functions, and then sampled at the initial wavelength map of the CCD, so that all determined wavelength shifts are with respect to the initial baseline wavelengths. The initial NP spectral registration will be performed during pre-launch calibrations and also by comparing the baseline solar measurements with the standard spectrum. This initial OMPS observed, calibrated spectrum is referred to as the reference spectrum. However, because of the higher spectral resolution of the standard solar spectrum, the wavelength monitoring uses it as a comparison to obtain better precision than with the reference spectrum. To establish the accuracy of the initial wavelength baseline, the pre-launch sensor radiometric response is used to compare the observed reference counts with the standard solar spectrum.

The slit functions themselves can change in shape and width during flight, but within the spectral fitting processing, the algorithm derives and compensates for FWHM changes. As a non-parameterized check of the derived wavelength shifts, and as a backup to the spectral fitting in case of poor fitting results, the algorithm uses a subset of solar Fraunhofer absorption lines in the initial standard spectrum in the form of a shift table to gauge wavelength shifts in the observed spectrum during the flight. Slit function changes, though, as they affect the line shift table, must be dealt with through off-line analysis and updates to the shift table.

After a sufficient and parameterized number of wavelength monitorings, the wavelength processing uses the newest sensor radiometric response, rather than the initial radiometric response, to compare the observed solar counts with the model standard irradiances. This accounts for changes in the radiometric response of the pixels (pixel residual non-uniformity: PRNU) that can affect the wavelength monitoring. Thus the wavelength monitoring with fitted model spectra maintains its precision during flight and is the primary wavelength calibrator.

The PRNU changes, however, could pose a challenge for spectral checking using individual lines because the changes can be mistaken for a shift of the Fraunhofer spectrum along a CCD row. Nevertheless, the Fraunhofer structure is well known, so a real spectral shift across the full CCD is well defined and unique. Our line spectral shift checking with approximately ten lines is based on the exceedingly high probability that optical and quantum efficiency changes will not mimic this unique pattern. The result of actual PRNU changes, assuming they are random along rows and columns, is a reduction in the shift resolution precision obtained through the solar Fraunhofer line shift technique.

3.1.3.4 Calibration Record Processing

The processing flow for calibration data shares many elements and proceeds in much the same way as for earth-view data (Section 3.1.2). A fundamental difference is that calibration data are not binned prior to downlink from the spacecraft. Also, several of the data corrections are derived from the calibration data (e.g. dark signals), so these corrections would not always be applied as they are for earth-view data.

There are two basic parts to SDR processing of calibration data: record processing and trending. The former refers to processing of data as it is encountered in the RDR. This data flow is illustrated in **Figure 3.1-15a**. Automated trend analysis of calibration data, shown in **Figure 3.1-15b**, will occur on a routine (at present, weekly) basis. We begin by describing record processing steps.

3.1.3.4.1 Database Input

Information stored in databases is required for calibration data reduction. Before processing Earth SDR data for each day, these databases are read for the appropriate day and stored in memory for use on all Earth data observed on that day. While Figure 3.1-15 indicates three required databases, in fact dark currents and bad pixels are

determined from the current set of calibration RDF dark data if they exist; otherwise the most recent database values are used. The goniometry data is only ingested when calibration data is encountered.

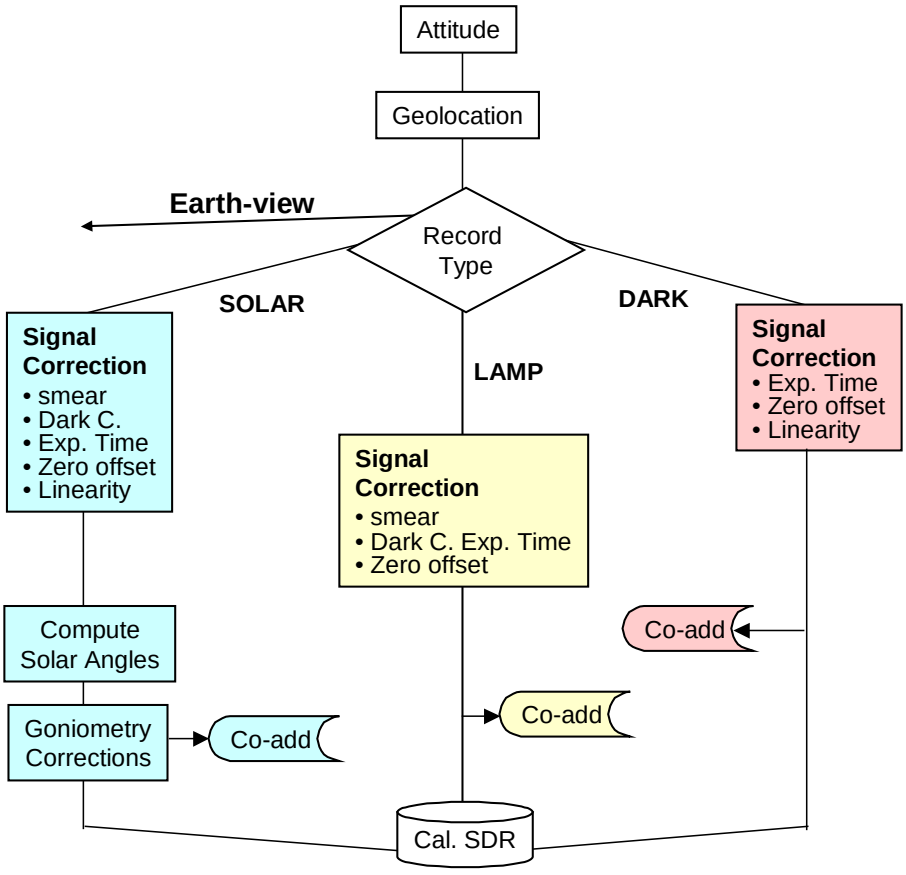

Figure 3.1-15(a). SDR processing flow for calibration records

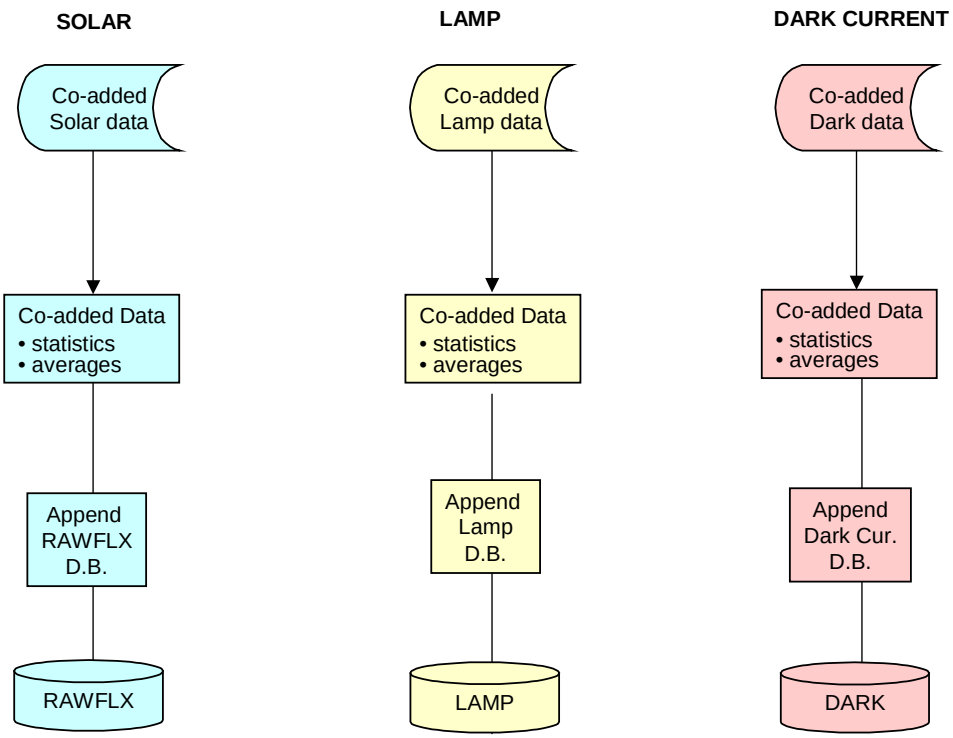

Figure 3.1-15(b). SDR processing flow for calibration records (continued)

3.1.3.4.2 Limit Checks on Input RDR Data

The RDR header quantities, such as sensor status, are written into the output SDRs for the corresponding input RDR. The sensor status values are also recorded in the appropriate calibration databases, but because a calibration record can span a range of time the sensor status values in the databases are an average over the calibration measurement period represented by the particular database record.

3.1.3.4.3 Initial Signal Corrections

Data corrections will begin once the record type is determined. Section 3.1.2.7 describes these corrections in more detail. These corrections are, for the most part, the same as for Earth-view data except for the linearity correction which is not needed for the EV data. When computing signal corrections, the SDR algorithm scales data counts by the ratio of integration times, data bin size, and number of image frame coadds to obtain the proper corrections. Table 3.1-3 summarizes the SDR signal corrections types.

Table 3.1-3: Signal corrections applied by the SDR algorithm to various data types

	Earth	*Solar*	*Lamp*	*Dark*
Bias	**X**	**X**		**X**
Dark	**X**	**X**		
Smear	**X**	**X**		
Linearity		**X**		**X**

3.1.3.4.4 Linearity

The linearity of the sensor radiometric response passing through signal amplifiers, is monitored using a series of lamp exposures of various times, and therefore varying count levels. To assess nonlinearities in the recorded count levels, the SDR algorithm processes and analyzes the RDR lamp calibration data, calculating separately for each image half the linearity response which is stored in the LINEARITY database. To retain the true count level during linearity calculations, dark current is not subtracted from the lamp data. The approach to analyzing the LED data and generating the linearity correction table is based on the BATC's LED database algorithm..

The raw lamp data are first corrected for smear, bias, and storage region dark current by subtracting the lowest ramped integration time image, and then averaged to get the average count for each ramped integration time image. A local quadratic fit to the average count levels in the reference integration time frames as a function of time stamp is used to determine the weights to be applied to the ramped integration times (*Tweighted*) to compensate for any lamp intensity instability. This produces the paired values of the corrected average counts (*Qreal*) and the corresponding weighted ramped integration times.

The linearity LUT is constructed from uncorrected ramped integration time data since it is the raw, uncorrected signals that are non-linearity corrected in the on-board software chain using the linearity LUT. To generate the linearity table, two tie points where the measured count levels equal to the ideal count values need to be defined. The lower tie point (*Qlow*), is defined as the count level at the lowest integration time, which is approximately equal to the values of the biases. The upper tie point (*Qup*), is a tunable algorithm parameter with a default value of 12000 counts, which was chosen to match that used by the OMPS data analysis team. Using all the data points of *Tweighted* vs. *Qreal*, the point in *Tweighted* corresponding to *Qup*, is located using a local quadratic fit. Between these two tie points, *Qup* and *Qlow*, a linear slope is determined and is

used to calculate the *Qideal* values corresponding to the weighted ramped integration times.

Once the array of *Qideal* corresponding to *Qreal* has been calculated, the LUT is constructed by using a local quadratic fit to each 3-point neighborhood [*Qideal*[i-1], *Qideal*[i], *Qideal*[i+1]] surrounding the interval *Qideal*[i] ≤ IndexLUT ≥ *Qideal*[i+1], where IndexLUT are the indices of the LUT (i.e. values from 0 to 16,383). For values of *Qideal* above 16383, the LUT will contain values of 16,383 since this is the 14-bit limit of the analog to digital converter.

The linearity tables created from the new calibration data will be reviewed and verified outside of the operational SDR algorithm. Once approved, it will be converted to the appropriate format for uploading to the spacecraft. The switch to the new linearity tables will occur in the ground SDR algorithm processing only when the earth view data to be processed are produced with the new linearity tables. Similarly, the calibration data is corrected for nonlinearity effects using the equivalent LUT of the flight version of the linearity table. The LUT is read at the beginning of the processing and is not automatically updated by the new calibration data.

3.1.3.4.5 Geolocation

Sensor geolocation (Section 3.1.2.5) is the same for Earth-view and calibration data, except that azimuthal and zenith scattering angles are not computed for the calibration data. Spacecraft-centered sun angles are needed for the goniometric correction of solar data. The SDR algorithm computes and stores the average subsatellite position separately for each kind of calibration data. It also calculates and stores the geocentric position and velocity vectors of the sun. Satellite velocity is subsequently used for computing the satellite-sun radial velocity used in spectral monitoring.

3.1.3.4.6 Goniometric solar corrections

A correction $1/g(\alpha,\beta)$ is applied that accounts for variations in irradiance sensitivity as the spacecraft-centered solar angles α and β change. This is a dimensionless quantity with a value of 1 at the angle at which radiometric calibrations were performed prior to launch. It will vary from pixel to pixel, i.e. spatially and spectrally. The pixel dependence of the correction can be established from pre-launch characterizations. If $C^i(t_{rep})$ represents the signal-corrected counts during report period t_{rep} with signal corrections applied, then the quantity $T(t_{rep})$ is written for each pixel into each SDR.

$$T\left(t_{rep}\right) = \frac{1}{T_o}\frac{C^i\left(t_{rep}\right)}{g\ t_{rep}} \tag{43}$$

In the equation, $T_o = C^i(0)/gt_{rep}$ refers to the fully corrected signal averages from the baseline solar measurement. The quantities T_o are stored as the first record in RAWFLX.

Operational implementation

The OMPS sensor has 2 diffusers – work and reference. Pre-launch characterization covers both diffusers and their nominal positions, as well as the range of solar angles, which may be seen during calibration on a given orbit. Characterization is done in the sensor coordinates.

The goniometry database input consists of these 2 BRDF tables, of corresponding solar angle tables, of actual diffuser positions for the measurement in the motor counts, and of the sensor on spacecraft mounting matrix. The database is preprocessed by transforming the BRDFs in the local diffuser coordinate system. This streamlines data processing and makes possible a fusion of BRDF data in order to better cover the solar angle range.

The goniometry algorithm gets information about the kind of diffuser used and about the diffuser position for a particular solar frame (RDR provides information about actual position of diffuser in the form of the motor counts; it may differ from the nominal position). Using this information, the algorithm transforms the solar angles in the spacecraft coordinates into the local diffuser coordinates and selects an appropriate BRDF table. It does the table interpolation and applies the goniometry correction to the flux_data and flux_err files. Applied goniometry coefficients are stored in the gon_par array and output in the SDR file in order to make possible a backprocessing of the flux data if necessary.

Flag information

The goniometry routine populates 2 flag variables. It also skips correction if sun was occulted by diffuser and passes the information to SDR algorithm to ignore this solar frame.

The variable occult_flag checks for the occultation of sun by the rotor and by Earth (night time calibration). It may have values 0, 1, 2, and 3 for each solar frame. 0 means that there is none of the above occultations, 1 means that the occultation by Earth takes place (night time), 2 means that the occultation by rotor occurred, and 3 means presence of both kinds of occultation. If this flag is set, the solar frame is ignored by SDR algorithm

The second variable, diff_incid_angle, passes the value of the solar incidence angle on diffuser to SDR algorithm. SDR algorithm may issue a warning if the solar rays are almost parallel to diffuser surface, because BRDF data may be too noisy at such angles or an extrapolation may occur.

3.1.3.4.7 Data co-addition and statistics

(The measured data are co-added onboard the spacecraft before downlinking to the ground. As a result, there is no need for co-adding the signal by the ground SDR processing. More importantly, it is no longer possible to calculate the statistics (e.g., standard deviation) from these effectively single measurements. Nevertheless, this section (3.1.3.4.7) is kept for the sole purpose of reference.)

Following the completion of signal processing of all RDRs of each data type in an RDF, the SDR algorithm coadds independently all SDRs of each data type: solar, dark, and lamp. The dark data $C^d(t)$ are summed and averaged to obtain a coadded dark calibration image.

$$D_{j,k} = \frac{1}{n_{rep}} \sum_{1}^{n_{rep}} \mathbf{L}\left(C^d_{j,k}\right) \; C^d_{j,k}\left(t_{rep}\right) \tag{44}$$

for an average exposure time of:

$$t_D = \frac{1}{n_{rep}} \sum_{1}^{n_{rep}} \left(t_{rep}\right)$$

The factor $\mathbf{L}(C^d)$ is the linearity correction read from the LINEARITY database. Lamp data $C^l(t)$ are coadded for each different integration time to obtain lamp count rates

$$L_{j,k} = \sum_{1}^{n_{rep}} \mathbf{L}\left(C^l_{j,k}\right) \; C^l_{j,k}\left(t_{rep}\right) / \sum_{1}^{n} t_{rep} \tag{45}$$

Solar data are coadded separately for each diffuser position *d*. Since diffuser positions probably will overlap slightly, this will likely result in multiple database entries for some pixels. The summation follows from Equation 43.

$$T\left(d\right)_{j,k} = \frac{1}{n_{rep} t_{rep} T_o} \sum_{1}^{n_{rep}} \frac{C^i_{j,k}\left(t_{rep}, d\right)}{g_{j,k}\left(d\right)} \tag{46}$$

A linearity correction **L** should be applied in Equation 46 as in Equation 43, if none is applied in the flight hardware (see discussion in Section 3.1.3.4.3).

Co-added calibration data are averaged and standard deviations are calculated. Lamp results L_{jk} are appended to the LAMP database, dark results D_{jk} are appended to the DARK database, and solar results T_{jk} are appended to RAWFLX. All records are uniquely identified by pixel location, orbit number, day, and year. Of the three databases, only RAWFLX contains normalized quantities. In particular, the entries representing the baseline solar measurement, *T(t=0)*, are all 1.

3.1.3.4.8 Solar spectral correction

Each record of the RAWFLX database contains the normalized, averaged, corrected solar signal for every pixel during a single calibration sequence. This quantity *T(t)*, defined in Equation 43, can be expressed in terms of the variables in Equation 29, where t refers to the calendar time of the calibration sequence.

$$T(t) = \frac{C^i(t)}{T_o\, g(t)} = \rho(t)\ \tau(t) \frac{F^m(t,\lambda)}{F^m\left(0,\lambda^r\right)} \tag{47}$$

The quantity *T(t)* represents two distinct components of solar measurements, sensor change and irradiance change. We emphasize this separation by re-writing the RAWFLX entries as

$$T(t) = \rho(t)\ \tau(t)\ \gamma \frac{F^m\left(t,\lambda^r\right)}{F^m\left(0,\lambda^r\right)} \tag{48}$$

where the factor γ is an estimate of the following ratio.

$$\gamma(\lambda,\lambda^r) \approx \frac{F^m(\lambda)}{F^m\left(\lambda^r\right)} \tag{49}$$

This factor, defined in Equation 70, describes the apparent change in solar irradiance resulting from spectral shifts of pixel bandcenter wavelengths. The quantity γ is estimated during wavelength trending and written in the BNDCTR database. Using estimates of $\gamma(t)$ and $\rho(t)$ (see discussion in Section 3.1.3.5.3), the SDR algorithm creates a second database called FLUX, which contains the quantity

$$T'(t) = \tau(t) \frac{F_m\left(t,\lambda^r\right)}{F_m\left(0,\lambda^r\right)} = \frac{T(t)}{\rho(t)\ \gamma(t)} \tag{50}$$

for each pixel. It is these values that are the basis for radiometric trending.

3.1.3.5 Calibration Trending

Calibration data are analyzed in more detail upon completion of the calibration SDR processing using results stored in the LAMP, RAWFLX, and DARK databases. No information from the RDF or SDF is utilized. It is important to note that for this reason calibrations of a particular type cannot be split across multiple RDFs. The flow for trending is shown in Figure 3.1-16. The purpose of trending is to provide an estimate of the calibration information at the time the earth observation is made. The process of extrapolating existing calibration results into the future has the added benefit of smoothing out random variations in those data.

3.1.3.5.1 Bad pixel update

The bad pixel database BADPIX is updated based on information from dark data. Potential bad pixels are output based on threshold values. These threshold values are tunable and set the upper and lower bounds of acceptable values (nominally set at 0 and 600). After HITL (human in the loop) review, pixels from this potential list can be accepted or rejected as bad. If accepted as bad, the EV_sampletable will be updated to exclude the newly determined bad pixels from both onboard and ground data processing.

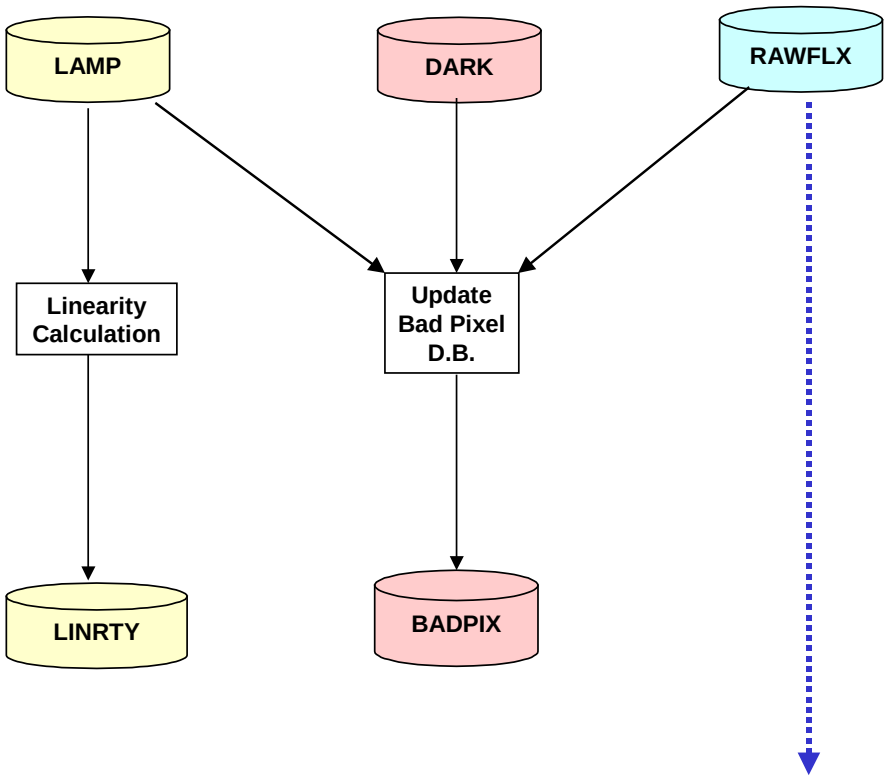

Figure 3.1-16 (a). SDR flow for trending calibration data

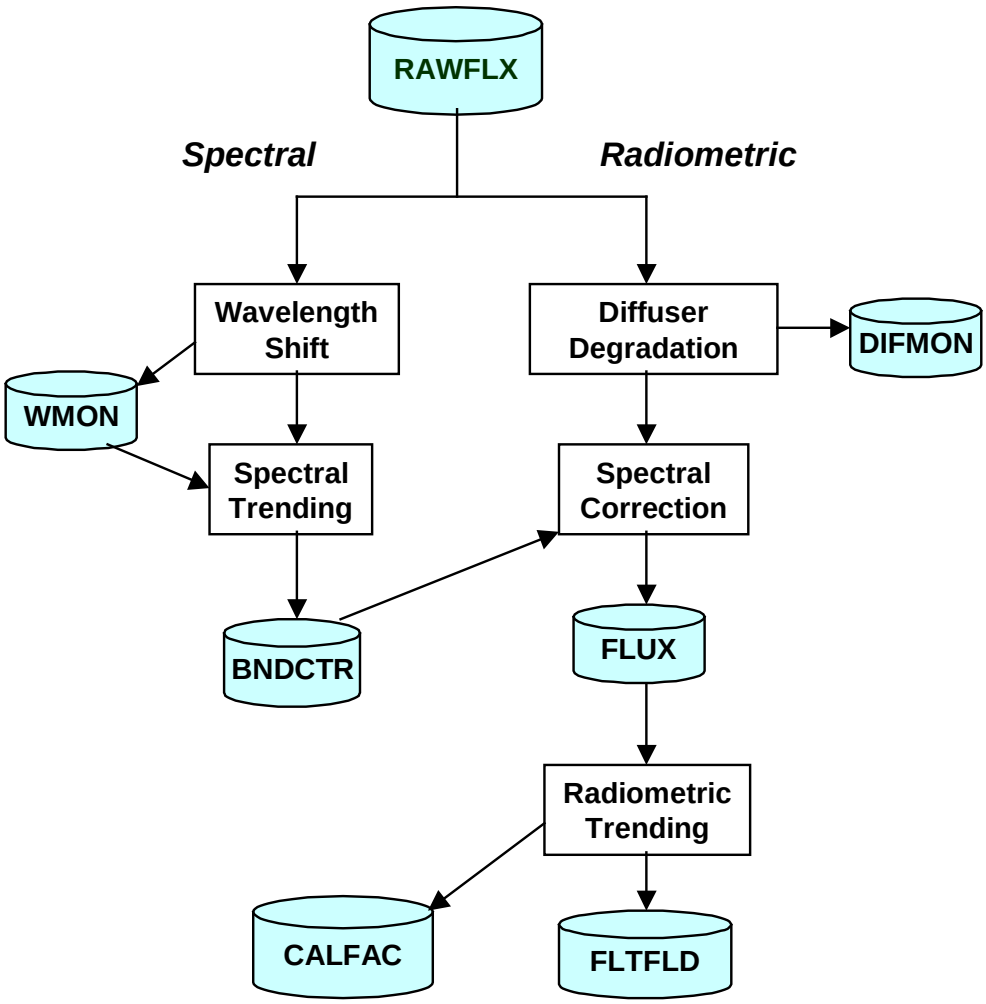

Figure 3.1-16 (b). SDR flow for trending calibration data

3.1.3.5.2 Diffuser Degradation

The basic approach for determining Working diffuser changes is described in Section 3.1.3.2, where the Working to Reference signal ratio

$$r_{jk} = \frac{W_{jk}}{R_{jk}} \tag{51}$$

was introduced. W_{jk} and R_{jk} represent the individual pixel signals from the Working and Reference diffusers, respectively. The operational algorithm will compute the values of W_{jk} and store them in RAWFLUX. R_{jk} is computed in an off-line process from the reference solar calibration data. Each pixel along a row (spectral dimension) measures a unique diffuser change. Since the solar diffusers are near a sensor aperture, each pixel's view of the diffuser surface overlaps that of adjacent pixels. Consequently, the values r_{jk} from many pixels along a column k can be combined without loss of information. Since optical degradation is thought to be a smooth, monotonic function of wavelength, r_{jk} values can also be combined in the spectral direction. The width of these spectral and spatial bins will depend upon the actual sensor performance.

$$r_{JK} = \frac{1}{n_{row} n_{col}} \sum_{j} \sum_{k} r_{jk} \tag{52}$$

The resulting averages r_{JK} would be used for off-line analysis of diffuser change. This analysis should ultimately produce an estimate for $\rho(t)$, determined by

$$\rho(t,\lambda) = 1 - \left(\frac{dW}{W} \right) \tag{53}$$

where dW/W is determined via Equation 36. The value of $\rho(t,\lambda)$ should be sampled at the appropriate band center wavelengths and entered into a database. The database values ρ_{jk} are read in by the SDR algorithm when computing the values T'_{jk}.

The values ρ_{jk} are initially all set to 1. With the proposed weekly solar measurement schedule, we do not expect significant degradation of the Working diffuser. TOMS diffuser data suggests the degradation that does occur has a linear wavelength dependence. The result is that the ozone products are insensitive to these changes. Should the need arise, the algorithm described above can be easily implemented.

It should be pointed out that the above analysis designed to monitor and characterize the solar diffuser degradation is not implemented in the operational algorithm. Instead, the analysis will be performed off-line by the cal/val and long term monitoring team. Once the solar diffuser surface degradation has been quantitatively characterized, the solar diffuser BRDF values of the working diffuser will be adjusted to bring the baseline working solar measurement into agreement with the baseline reference solar measurement.

3.1.3.5.3 Radiometric calibration

The radiometric calibration of the earth-view radiances, described in Equation 28, amounts to multiplying corrected counts by an initial calibration constant and dividing by an estimate of the pixel response change $\tau_{jk}(t)$. The values $T'_{jk}(t)$, stored in FLUX, are a close approximation of response change, differing only when the solar output changes.

In the BUV technique it is not possible, nor is it necessary, to separate sensor and solar changes. However, the resulting radiance $I^m_{jk}(t)$ (Equation 28) is in error by the amount that the solar output changed at the wavelength in question. Only the normalized radiance, in Equation 30, is a properly calibrated quantity.

Experience with TOMS (see ICSR-8110501) has demonstrated that a linear time dependence is quite adequate for trending over one week intervals. The number of previous data values included in the regression is typically less than ten. But the optimum number depends upon how the sensor response actually changes with time. Each regression is extrapolated in time to yield estimates of $\tau_{jk}(t+i)$, where *i* is the day number following the last solar measurement. For a weekly measurement schedule, *i* begins at 0 and need not exceed 7, though it is safer to generate more values and simply overwrite them as new solar measurements are made.

The SDR trending algorithm derives the calibration factors $\tau_{jk}(t+i)$ from $T'_{jk}(t)$ in an indirect manner. The temporal variations in TOMS solar data exhibited a significant degree of correlation between channels, with the result that channel ratios were less noisy than single channels. It follows, and was verified in the TOMS data, that the extrapolated channel ratios will remain closer to the true ratios than will the ratios of extrapolated single channels. With this in mind, the NP radiometric trending also operates on pixel ratios (along a row). The SDR trending algorithm computes ratios of T'_{jk} values for use in trending. Let *s* and *l* represent short and long wavelength values for each row *j* of T'_{jk}. The ratios *r* are simply

$$r = \frac{s}{l} \tag{54}$$

Trending yields the values *r'* and *l'*. A simple inversion of Equations 54 yields the trended value *s'* of $\tau_{jk}(t+i)$.

$$s' = l'\, r' \tag{55}$$

The choice of spectral pixels for *s* and *l* is somewhat arbitrary. We recommend choosing pixels at 306 nm or longer for the long channel in each row.

The algorithm computes calibration factors $A_k(t+i)$ by binning the extrapolated responses $\tau_{jk}(t+i)$ in each of the EV macropixel:

$$A_k(t+i) = \left[\frac{1}{nmacro} \sum_j \tau_{jk}(t+i) \right]^{-1}$$

where *nmacro* is the number of pixels made up of the *kth* macropixel, as derived from the macropixel sampletable. The binning is fewer than nmacro if the EV_sampletable indicates that the flight software will have excluded specific pixels in its binning. The daily values of A_k for each macropixel are stored in the database CF_EARTH. These

daily values can be overwritten if a better estimate is obtained, but only prior to their use in the Earth SDR processing.

3.1.3.5.4 Flat Field update

The flight hardware sums the signals from 96 pixels along a CCD column in a process referred to as binning. The radiance calibration constants k^r and calibration factors A, which are derived per pixel, are similarly binned in the SDR algorithm (see Equation 22). However, a significant radiometric error can occur if the individual pixel signals are binned prior to radiometric correction. This follows because

$$\sum_j k_j C_j \neq \sum_j k_j \sum_j C_j \tag{56}$$

To correct this error, a flat field correction is applied in the flight hardware prior to binning earth-view signals. The correction η_{jk} equalizes the pixel signals using the relative photon response non-uniformity (PRNU) as a weight.

$$\eta_{jk} = \frac{\frac{k^r_{jk}}{\tau_{jk}}}{\frac{1}{nmacro}\sum_j \frac{k^r_{jk}}{\tau_{jk}}} \tag{57}$$

The PRNU is estimated as k^r/τ where τ is obtained from an unbinned version of the CF_EARTH database. Similar to calibration, the SDR algorithm has the flexibility built in either to apply or not to apply calibration factor correction when computing the flat filed table, depending on the accuracy of the calibration factor computed from trending the solar data. As before, the sum is over fewer than nmacro when EV sampletable indicates a flight hardware pixel rejection. An important point concerning η_{jk} is it does not alter the binned signal, so the calibrations applied to the data cell by the Earth SDR algorithm need not be altered. Also, it does not alter the relative calibration between binned rows and columns.

The algorithm computes a full set of η_{jk} and appends the results to the FLATFIELD database. Thus there is a one-to-one correspondence with records in the RAWFLX database. The contents of the FLATFIELD database can be periodically loaded into tables for uplink to the flight hardware as deemed necessary. Since changes in PRNU are primarily the result of optical degradation, which has a broad spectral dependence, weekly uplinks to flight hardware are more than adequate.

3.1.3.5.5 Wavelength Registration - Operational

The operational algorithm computes bandcenter wavelength shifts by varying the standard solar irradiances using several model parameters, and then minimizing the differences between these model irradiances and the observed irradiance changes over the entire usable spectrum. The algorithm is based on Caspar and Chance (1997) [Caspar, C. and Chance, K., GOME Wavelength Calibration Using Solar and Atmospheric Spectra, Proc. 3rd ERS Symposium (ESA SP-414), p. 609, 1997.]

Additive spectral shifts and multiplicative shifts are primary spectral parameters that are applied to the standard spectrum to obtain a model spectrum. The derived shifts are relative to the wavelength scale that includes the grating dispersion. The fitting parameters account for grating rotations and focal plane shifts in the dispersion direction. The latter two effects are non-linear in wavelength, as given by the dispersion relation. But the change in the dispersion from the short to long wavelengths is about two percent, so a linear approximation is valid.

To account for broad, spectrally dependent diffuser and sensor response changes, one can vary multiplicative parameters for a cubic scaling in wavelength of the reference spectra by a polynomial.

$$P(\lambda) = a + b\lambda + c\lambda^2 + d\lambda^3 \tag{58}$$

In practice, the implemented Algorithm fitting as initially configured uses a linear subset of the parameters. To compute optimal additive and multiplicative spectral shifts that are actually present in the observed OMPS NP spectrum, the algorithm calculates a minimum chi-squared statistic over all wavelengths in common between the shifted F^s and model F^r spectra with noise σ.

$$\chi^2(\delta,\beta) = \sum_{\lambda} \left\{ \frac{F^s(\lambda) - P(\lambda) \cdot F^r(\lambda[1+\beta]+\delta)}{\sigma} \right\}^2 \tag{59}$$

$$\Delta_{\min} = \arg\min_{\delta}\{\chi^2(\lambda[1+\beta]+\delta)\} \tag{60}$$

$$\mathrm{B}_{\min} = \arg\min_{\beta}\{\chi^2(\lambda[1+\beta]+\delta)\} \tag{61}$$

where $\Delta_{\min}$ and $\mathrm{B}_{\min}$ are the resulting additive and multiplicative shifts, respectively.

The model spectrum F^r used in the regression is the convolved standard spectrum sampled at the baseline NP bandcenter wavelengths. At t=0, this should be equivalent to what is termed the reference solar flux. The current shifted spectrum containing

radiance changes due shifts and not changes in the sensor response can be expressed in terms of the reference spectrum, the newest solar measurement ratio, and calibration.

$$F^{s}_{jk}(t) = T_{jk}(t) F^{r}_{jk}(0) k^{i}_{jk} / \tau_{jk}(t) \quad (62)$$

By radiometrically calibrating the measured solar signal, the sensor fixed pattern noise and radiometric response are removed. The SDR algorithm processes solar data in the beginning of the flight with $\tau_{jk}(t)=1$. After processing a parameterized number of wavelengths monitorings during flight to attain the required precision, the algorithm then uses the newest previous *radiometric* calibration $\tau_{jk}(t-1)$ to account for the sensor response, independent of wavelength shifts. The wavelength monitoring obtains the radiance calibration factors by reading them from the CF_SOLAR database, which is based on the radiometric database FLUX.

Before performing the shift analysis, previously identified bad pixels are interpolated across or excluded by weighting them by an uncertainty equal to their value. The wavelength algorithm computes spectral shifts, additive and multiplicative, separately for each spatial row of the unbinned solar RDR data. In order to reduce the effect of sensor noise and the aliasing of PRNU changes into spectral shifts, the algorithm spatially averages the resultant shift information across all the pixels in a terrestrial data cell before storing it in the shift monitoring database WMON. Thus, the entire spatial region on the CCD, as defined by the Earth-view binning prescription, has a spectral registration determined using the measured solar spectrum in that region. Stored uncertainties in the shifts are also calculated as the standard deviations across the spatially averaged region. Only one final average wavelength scale over the binned region (horizontal spatial cell) is stored within WMON, WAVELENGTHS, and the binned Earth data cell in the output SDR file.

3.1.3.5.6 Discrete Spectral Lines

As a non-parametric measure of the wavelength shifts, the algorithm also calculates shifts of narrow spectral absorption lines at discrete wavelengths across the solar spectrum. This has the advantage that no assumptions are needed regarding the nature of the sensor spectral dispersion. In contrast to the parametric shifts derived from the continuum, shifts are derived by comparing the observed irradiance changes with a set of irradiance changes stored in a pre-computed reference shift table $M_{j\kappa\delta}$, where δ identifies the grid of shifts and κ refers to detector columns associated with specific Fraunhofer line. The row index *j* is introduced because of the slight spectral smile (row dependence) at the NP focal plane.

A response change, $d_{j\kappa}$, is determined from the RAWFLX entries $T_{j\kappa}$ according to

$$d_{j\kappa}(t) = 1 - T_{j\kappa}(t)$$

(63)

To remove broad spectral changes in diffuser and sensor response, the observed changes on each side of a line with center at pixel κ are subtracted from each other.

$$D_{j\kappa} = d_{j\kappa-1} - d_{j\kappa+1} \tag{64}$$

The contents of the table $M_{j\kappa\delta}$ are the computed column signal differences D for absorption lines κ with varying wavelength shifts S_δ. Linear interpolation of the observed difference in the shift table yields the estimated spectral shift $S_{j\kappa}$ at each pixel j,κ.

$$S_{j\kappa} = \frac{D_{j\kappa} - M_{j\kappa\delta-1}}{M_{j\kappa\delta} - M_{j\kappa\delta-1}} \cdot \left(S_\delta - S_{\delta-1}\right) + S_{\delta-1} \tag{65}$$

As with the parametric method, small-scale changes in diffuser and sensor response are removed by spatially averaging the shift results over rows *j*. The shift linearity with wavelength is checked with a linear regression fit to the line shifts. Individual line shifts, group shift values, uncertainties, and linear fitting parameters are stored in the WMON database. The linear regression and individual line shifts thus provide a comparison for the assumed linear shift that was derived previously in the operational algorithm.

3.1.3.5.7 Wavelength Trending in Time

For every day of the year, the wavelength trending algorithm predicts the spectral wavelengths for each Earth-view data cell. Bandcenter wavelengths are determined by adding a derived shift to the baseline wavelength scale. Trending is only performed on results from the operational method described above. If the wavelength fitting produces poor fits, as parameterized by a χ^2 threshold, the SDR algorithm substitutes the wavelength shift parameters that were derived from the discrete line-shift method.

Following updates to the WMON database, the algorithm performs a regression for the additive and multiplicative shift terms (see Equations 60 and 61). Regression results are extrapolated and evaluated daily for at least 2 weeks into the future. The Earth SDR algorithm reads these predicted values from the WAVELENGTHS database to provide the spectral registration of the Earth data cell in each Earth SDF. Once a WAVELENGTHS value is actually used for the output SDRs, the value in the database remains unchanged to serve as an additional history of the SDR spectral calibration. However, when the WMON database is subsequently updated, the trending algorithm overwrites outdated predicted values in WAVELENGTHS that were never used.

Regressions of the additive and multiplicative shift terms take the following forms.

$$\Delta_{Jk}(t) = \delta_{Jk} + \delta'_{Jk} t \tag{66}$$

$$B_{Jk}(t) = b_{Jk} + b'_{Jk} t \tag{67}$$

The daily values λ_k appended to the WAVELENGTHS database take the form

$$\lambda_k = \lambda^r_k + S_k \tag{68}$$

where

$$S_k = \delta_k + b_k \lambda^r_k + \left(\delta'_k + b'_k \lambda^r_k\right) \cdot (t + i) \tag{69}$$

and λ^r_k are the baseline bandcenter wavelengths of the macropixels. As with the radiometric trending, the time *i* refers to the day number beyond the most recent calibration, denoted by *t*. The algorithm computes wavelength precisions by propagating errors in root of the mean square minus the covariance of the linearly dependent additive and multiplicative parameters.

Alternatively, the shifts S_{Jk} can be averaged over spatial locations *J* provided they have no spatial dependence. The resulting values S_k would then be used for all *J* in Equation 68. Recall that the discrete method results are stored as a means of checking spatial and spectral dependence of the shifts.

3.1.3.5.8 Irradiance Shift Factors

Following the bandcenter wavelength prediction, the algorithm computes a set of solar shift factors. In order to derive normalized radiances, as represented in Equation 30, the EDR Algorithm must be provided measured irradiances $F^m(\lambda)$ on the same spectral scale as earth radiances. The irradiances are estimated in Equation 28 by scaling the baseline solar irradiances $F^m(\lambda^r)$. The scale factors $\gamma(t)$ describe the change in measured solar irradiance arising from shifts $\lambda(t)$-λ^r, and are defined as follows for each macropixel *k*.

$$\gamma_{Jk}\left(\lambda, \lambda^r\right) = \frac{F^r_{Jk}(\lambda)}{F^r_{Jk}\left(\lambda^r\right)} \tag{70}$$

The irradiances Fr(λ) are the standard spectrum convolved with the sensor spectral functions and evaluated via interpolation at the bandcenter wavelengths λ(t). The bandcenters are those written in the WAVELENGTHS database. The irradiances Fr(λr) are the reference spectrum, which uses the baseline spectral registration λr. The shift

factors γk, registered by day, are stored in WAVELENGTHS database along with the bandcenter wavelengths.

3.2 EDR PRODUCTION

The OMPS Nadir Profiler SDR algorithm's output format is based on the OMPS Total Column SDR algorithm's output format, and is different from PMF input format used by SBUV/2 Product Processor. In addition, the OMPS Nadir Profiler SDR algorithm produces calibrated radiances with approximately 0.42 nm sampling. In general, these wavelengths differ from SBUV/2 wavelengths and will shift through the mission. Therefore we have developed and implemented a module to convert radiances and other data from the OMPS NP SDR output format to the SBUV/2 PMF format. The OMPS NP SDR format also includes data, which are not used currently for processing but may be used in the future versions of the EDR Algorithm.

3.2.1 Wavelength Interpolation (OMPS to SBUV/2)

For the conversion of OMPS NP SDR algorithm output radiances to NOAA-11 wavelengths we use cubic spline interpolation. This interpolation introduces additional errors. Since the OMPS wavelengths will shift through the mission, we have included this error in the random error budget (see Section 7).

To determine the expected interpolation errors, a variety of atmospheres and viewing conditions were considered (see Table 3.2-1). Typical radiances are shown in Figure 3.2-1, where the dotted lines indicate different NOAA-11 channels and the dashed line separates NP and TC channels. We assumed that SDR wavelengths are uniformly spaced from 250 nm and to 380 nm with 0.42 nm steps. For the interpolation study, ten different sets of SDR channels starting at 250 nm + 0.042 nm*n, n=0,..,9 were generated. After this, for each SBUV/2 channel and each set the interpolation error is calculated. The ozone retrieval is performed in each case, and the relative error for all reported altitudes and total ozone is computed. The results are summarized in the Table 3.2-2.

Table 3.2-1. Profiles and parameters used for simulations and retrievals

Profile	SZA (deg)	Pressure (atm)	Reflectivity (%)	Lat (deg)	Lon (deg)
L275	7.8	1.0	15	0	0
M325	7.8	1.0	15	45	45
H475	7.8	1.0	15	80	0
L325	0	1.0	15	0	0
H225	80	1.0	15	80	0
L225	0	0.4	90	0	0
H575	80	0.4	90	80	0

Table 3.2-2. Relative ozone error caused by wavelength interpolation

1 mb	3mb	10mb	30mb	TOZ
0.01%	0.02%	0.04%	0.15%	0.03%

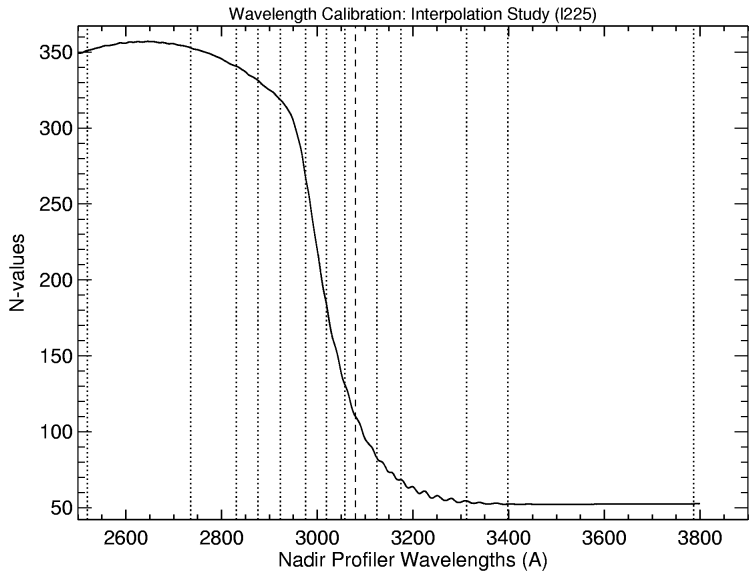

Figure 3.2-1. Radiances generated by TOMRAD for a sample L225 atmosphere

3.2.2 Albedo Measurements

The algorithm operates on the albedos whose derivation from the raw counts has been described in Section 3.1. Albedos are available for all 12 wavelengths listed in Table 3.2-3. The albedo at 255.6 nm is not used in the derivation of ozone profiles because McPeters (1980) has shown that the radiance at this wavelength is contaminated by emission in the 255.1 nm NO band. In subsequent BUV sensors including SBUV/2 and OMPS, this channel is moved to 252 nm to avoid NO contamination.

Table 3.2-3. Absorption and Scattering Coefficients

Wavelength (nm)	Ozone Absorption Coefficient* $(atm\text{-}cm)^{-l}$	Absorption Coefficient Sensitivity (**)	Rayleigh Scattering Coefficient (atm^{-1})
251.97	307.5	0.07	2.4573
273.55	169.9	-0.80	1.8131
283.08	79.88	-0.76	1.5660
287.64	48.33	-1.3	1.4597
292.27	27.82	-1.2	1.3627
297.55	13.66	-1.4	1.2605
301.93	7.462	-1.2	1.1831
305.80	4.281	-1.0	1.1194
312.49	1.632	-1.6	1.0198
317.49	0.8684	-0.8	0.9527
331.22	0.1397	-3.5	0.7956
339.80	0.0248	5.4	0.7134
378.61	—	Not Applicable	0.6864

* Calculated at a nominal temperature

** Percent change in absorption coefficient per 0.1 nm change in wavelength

For application of the algorithm, the measured albedos are converted to two functional forms:

a. the Q-Value:

$$Q_\lambda = \{4\pi / [\beta P(\cos\theta)]\}(I_\lambda / F_\lambda). \qquad \text{(same as equation 4)(71)}$$

b. the N-Value:

$$N_\lambda = 100 \log_{10}(I_\lambda / F_\lambda). \qquad (72)$$

3.2.3 Computation of Albedos

For the 292 nm and longer wavelengths, software using successive iterations of the radiative transfer equation (Dave, 1964) is used to compute theoretical albedos. This calculation requires the following information:

- Ozone absorption coefficients α_λ as a function of temperature for the BUV wavelength bands
- Rayleigh scattering coefficients β_λ
- Standard temperature profiles
- Standard ozone profiles
- Surface pressure at the lower boundary of the atmosphere
- Solar zenith angle

The resultant albedos are stored in the look-up tables used by the total ozone algorithm and the multiple scattering and reflectivity (MSR) correction table used by the nadir profile algorithm.

The effective ozone absorption coefficient is computed separately for each wavelength channel as a function of temperature and Rayleigh scattering. Table 3.2-3 gives the ozone absorption coefficients at nominal temperatures and the Rayleigh scattering coefficients.

A function is fit to the dependence of the measured absorption coefficients on temperature (Paur and Bass, 1985). Using this function with the standard temperature profiles (Environmental Science Services Administration et al., 1966), ozone absorption coefficients for the SBUV wavelengths are derived at different altitudes. The version 7 implementation of this algorithm will most probably use improved measurements of the ozone absorption spectrum in the region near 340 nm.

Twenty-three standard ozone profiles have been constructed, from an ozone climatology based on past satellite results for altitudes above the 16 mbar level and on balloon ozonesonde measurements for lower altitudes. The shape of a profile for a given total ozone value depends upon latitude (Bhartia et al., 1985). Profiles are constructed for three latitude bands: low-latitude (15°), mid-latitude (45°), and high latitude (75°). The mid- and high-latitude sets include 125 m-atm-cm and 175 m-atm-cm profiles that are characteristic of the Antarctic Spring minimum in ozone. The mid-latitude low ozone profiles are provided only as interpolation points and are identical to the corresponding high-latitude profiles. These profiles are given in Appendix B. The Version 7 algorithm will use a somewhat different set of standard profiles that have been adjusted to more completely span the ozone profile climatology (Wellemeyer et al., 1996).

Given the wavelength, total ozone and ozone profile, surface pressure, and solar zenith angle, the quantities I_0, I_s, f_1, and f_2 of equation (1) are calculated. For the tables used in the algorithm, these terms are computed for the eight longest wavelength channels and for the reflection monitoring (photometer) wavelength, for all 23 standard profiles, and two reflecting surface pressure levels (1.0 atm and 0.4 atm). For each of these cases, I_0 and I_s are calculated for ten choices of solar zenith angle, with a finer grid for higher zenith angles; f_1 and f_2 do not depend on zenith angle. As discussed in Section 2.1, the amount of second order and higher scattering and surface reflection for wavelengths shorter than 292 nm is negligible. At these wavelengths, I_0 is computed using a simpler formulation that considers only single scattering.

3.2.4 Computation of Reflectivity

As discussed in Section 2.1, the contribution of clouds and aerosols to the backscattered intensity is treated by assuming that radiation is reflected with a single effective reflectivity from a particular pressure level. In the BUV ozone retrieval algorithm, reflectivity is estimated using the radiances from the wavelength band at 340

nm. In this wavelength region, the reflectivity is weakly sensitive to the ozone amount; a change in ozone of 50 milli-atm-cm affects the reflectivity by less than one percent. To incorporate the ozone dependence into the calculated reflectivity at 340 nm, an iterative procedure is used. An estimated reflectivity is calculated using a climatological ozone value. Using this estimated reflectivity, an estimated total ozone is derived. The reflectivity is then recomputed, using the estimated total ozone. This reflectivity is then used in the final total ozone derivation.

In the wavelength-scanning SBUV instruments, photometer measurements at 380 nm, each coincident with the monochromator measurement at one wavelength, were used to monitor changes in scene reflectivity. These photometer measurements will be unnecessary for the OMPS nadir profiler since it measures all wavelength channels simultaneously.

Solving (1) for reflectivity R gives

$$R = (I - I_0)/[I_s f_1 + (I - I_0) f_2]. \tag{73}$$

With I_o, I_s and f_2 from the tables for the respective wavelengths, reflectivities are computed for surfaces at pressures of 1.0 and 0.4 atm.

3.2.5 Estimation of Surface Pressure

In the derivation of ozone values, an effective IFOV surface pressure, P_o is estimated from the terrain pressure P_t and the estimated cloud top pressure P_c using the following expression:

$$P_o = (1 - w)P_c + wP_t. \tag{74}$$

The weighting function w is based on the measured surface reflectivity. A higher reflectivity generally implies greater cloudiness. Normally, when snow or ice is not present, w is set to unity for R<0.2, to zero for R>0.6, and is obtained by linear interpolation as a function of R for intermediate reflectivities.

A different method is used to obtain effective surface pressure when there is evidence for snow or ice in the IFOV. Snow or ice thickness data from around the globe are collected by the Air Force Global Weather Center and mapped on a polar stereographic projection. These data have been mapped onto a 1° x 1° latitude-longitude grid and used to determine the presence or absence of snow in the IFOV. When snow or ice is present, it is assumed that, despite the high reflectivity, there is only a 50 percent probability that clouds are present. The effective pressure is then obtained by averaging the value of P_0 obtained from (60) with the terrain pressure.

The cloud-top pressure is estimated from an empirical climatology based on studies using THIR measurements:

$$Pc(atm) = 0.3 + 0.15[1 - \cos(2 \cdot lat)]. \quad (75)$$

There is also a possibility of using cloud top pressure from an external source. This option can is can be activated by a flag in the EDR Algorithm input.

When external measurements are available, total ozone values retrieved using external cloud-top pressures are computed. Total ozone values derived using the empirical climatology are computed whether or not external data are available.

The average terrain heights are available from the National Oceanic and Atmospheric Administration National Meteorological Center (NOAA/NMC), given in km for 2.5° x 2.5° latitude and longitude cells. These heights are converted to units of pressure and interpolated to each IFOV to establish the surface pressure at the point on the Earth's surface directly below the satellite.

3.2.6 Total Ozone

When measured and computed albedos are compared in the determination of total ozone, the albedos for individual wavelengths are not compared directly. Albedo ratios, called pair values, are calculated. A pair value is the ratio of the albedo at a longer wavelength that is relatively insensitive to ozone to that for a shorter, ozone sensitive wavelength. The use of albedo ratios reduces the effect of wavelength-independent uncertainties in the spectrometer calibration.

From the ozone values derived from the individual pairs, a "Best" ozone value is selected or computed, based on the sensitivity to ozone, profile shape, and wavelength separation of the values from each individual pair. When external cloud height data are available, a "THIR Best" total ozone value is also obtained.

3.2.6.1 Application of Tables

As discussed in Section 3.2.1, the measured albedos are expressed in terms of N-values, which are proportional to the logarithm of the albedo. A ratio of albedos then becomes a difference of N-values. Three pairs are defined:

A-Pair = N313 - N331
B-Pair = N318 - N331
C-Pair = N331 - N340

For each of the above N-value differences or pairs, four estimates of total ozone values are calculated. Values of total ozone above 1 atm are derived for reflecting surfaces at

1.0 atm and 0.4 atm. For each of these pressures, ozone values are derived from the two standard latitudes surrounding the actual latitude of the measurements. In each case, N-values for the solar zenith angle of the measurement and the given latitude and pressure level are computed from the table values of I_0, I_s, and f_2. These N-values produce table-derived pair N-value differences for total ozone values at 50 milli-atm-cm intervals. Ozone between the terrain height and actual pressure level is subtracted using the amount of ozone between 0.4 and 1.0 atm in the standard profile as a basis, assuming that cumulative ozone is linear with log pressure at these levels. Interpolation of the measured N-value pair difference in the table-derived N-value pairs produces total ozone values for each latitude and pressure. The total ozone values for the two pressures are combined using (17). The ozone value for the latitude of the measurements is derived by linear interpolation in latitude between the values for the two bordering standard latitudes. Between 15° and the equator, only the profile set for below l5° is used; poleward of 75°, only the profile sets for above 75° are used, both without interpolation or extrapolation. An average reflectivity is calculated in the same manner.

3.2.6.2 Best Ozone

The Best ozone is a weighted average of the total ozone values derived from the A-, B-, and C-pairs:

$$Best = (W_A f_A \Omega_A + W_B f_B \Omega_B + W_C f_C \Omega_C)/(W_A + W_B + W_C), \quad (76)$$

where the adjustment factors f_A, f_B, and f_C have been selected to remove existing biases between the ozone values derived from the different pairs. These biases have been derived from the ozone values yielded by different pairs in the regions where both provide information, near a zenith angle of 45° for the A- and B-pairs and near 75° for the B- and C-pairs. By convention, the adjustment f_A for the A-pair is defined to be unity. The adjustment factor f_C, which corrects for the bias between the A- and C-pairs, is derived from the measured adjustment factor for the C-pair relative to that for the B-pair ($f_{C/B}$) by the following expression:

$$f_C = f_B f_{C/B}. \quad (77)$$

For Nimbus 7 SBUV, f_B=0.98, and f_C=1.10. The values used for subsequent SBUV/2 sensors are similar, because the offsets are largely due to Ring effects not taken into account in the forward model (Joiner et al., 1995).

The weight W for each individual pair is derived from the following sensitivity factors:

s_1 = Sensitivity of the pair N-value to changes in total ozone ($dN/d\Omega$),

s_2 = Sensitivity of the pair ozone to the wavelength dependence of the reflectivity (assumed to be inversely proportional to the separation of the two pair wavelengths),

s_3 = Sensitivity of the pair ozone to the ozone profile shape (assumed to be proportional to s_i divided by the sensitivity that would be derived using Beer's law if all the radiation were scattered from the ground). The Beer's law sensitivity is proportional to the difference between the ozone absorption coefficients at the two pair wavelengths, using the expression

$$W = s_1^{\,2} s_2^{\,2} s_3^{\,2}. \tag{78}$$

The overall weighting factor for a given pair is then given by the following expression:

$$W = (\delta\lambda)^{-2} (\delta\alpha)^{-2} (dN / d\Omega)^4, \tag{79}$$

where $\delta\lambda$ is the separation of the two pair wavelengths, and $\delta\alpha$ is the difference between the absorption coefficients at the two pair wavelengths.

3.2.6.3 Validity Checks

The algorithm performs several validity checks for maintaining data quality. Before measured radiances are accepted for use in ozone determination, the solar zenith angle, satellite attitude, and instrument status are checked to ensure the suitability of the radiances and other geophysical input to the algorithm. This section describes the quality checks performed on the derived reflectivity and Best ozone to identify invalid ozone values caused by either bad input data that passed preprocessing checks or by limitations of the ozone algorithm. The data quality for each sample is identified by a data quality flag. The total ozone flag is in word 26 of the output data record for "THIR" total ozone and word 40 for "non-THIR" total ozone. Note that the individual pair values, which also are stored in PMF (Product Master File) data format, are neither checked nor modified. The PMF data format is described in section 6.3.

Next, checks are made on the reflectivity. The reflectivity must be no less than -0.05 and no greater than +1.05. If the reflectivity is outside this range, the Best ozone is set to -999, and the error flag is set to 8.

The Best ozone is then compared with the total ozone returned by the profile algorithm. If the two ozone values differ by more than 3 standard deviations, usually about 1.5 percent, the quality flag is set to 5 and Best ozone is set to -999. The ozone profile is still derived in this case.

If the data pass flags 9, 8, 7, and 5, the ozone path is calculated in units of atm-cm:

$$ozone\ \ path = BEST\ x\left(1 + \sec\theta_0\right). \tag{80}$$

The consistency between Best ozone and the A-, B-, or C-pair is then checked; the pair used in the comparison is the one with the largest weighting factor, as given by (22). The quality flag is set to 4 if inconsistency exists, and Best ozone is set to -999. Data

that pass flag 4 are assigned a flag value of 0, 1, or 2 as determined by the ozone path, see Table 3.2-4:

Table 3.2-4. Best Ozone Data Quality Flags

Ozone Path	Quality Flag	Pair Used in Flag 4 Consistency Check
1.5	0	A
1.5-3.5	1	B
3.5	2	C

If the data were taken on the descending (north to south) part of the orbit, the value 10 is added to a flag value.

3.2.7 Profile Ozone

Ozone profiles are derived from the measured albedos using an optimum statistical inversion technique (Rodgers, 1976; Klenk et al., 1983; Bhartia et al., 1996). Because the retrieval of an ozone profile is an attempt to derive a continuous function from a limited number of its integrals, the solution is not unique. An additional constraint, called *a priori* information, is needed to select the particular solution most likely to represent physical reality from among the possible mathematical solutions. Generally, the *a priori* information can be mathematical restrictions on the form of the solution, constraints derived from the physics of the problem, independent information on the solution, or other assumptions. The retrieved profile is thus constructed from both the *a priori* information and the measured albedos. Because the *a priori* information is an integral part of the profile construction, it is sometimes referred to as “virtual measurements.”

The *a priori* information used in the inversion algorithm for the BUV ozone profile includes a “first guess” profile derived from the best available ozone climatology for the lower portion of the profile and from the three shortest wavelength channel radiances for the uppermost portion. The albedos that such an ozone profile would yield are calculated. The differences between the albedos calculated from the first guess profile and the measured albedos are then used to provide a new set of profile values that are more nearly consistent with both the measured albedos and the first guess profile.

Application of the optimum statistical technique requires not only the measurements and *a priori* profiles but also an assessment of their uncertainty or variance. In the case of the albedo, the uncertainty is characterized by the measurement errors. The method also requires the covariance of the measurement errors, to determine how dependent the errors at one wavelength are on the errors at another. For the *a priori* information, the variances and covariances are obtained in the development of the climatology.

The derived ozone profile data are provided in two formats. In the first format, the ozone content is given in units of milli-atm-cm (Dobson Units) for each of 12 layers. These layers extend from the Earth's surface to the top of the atmosphere, with widths of approximately 5 km. The second format is volume mixing ratio in units of parts per million (ppmv), at specified pressure levels from 100 mbar to 0.3 mbar. Volume mixing ratios in parts per million (ppmv) are obtained by dividing the mass mixing ratio by 1.657. Details of the two formats are presented in Section 6.

3.2.7.1 *A Priori* Information

The *a priori* information used by the inversion method consists of a first guess and its variances and covariances. The first guess is constructed from a lower profile in Umkehr Layers 0-5 that is a climatological function of total ozone and latitude, and an upper profile in Umkehr Layers 9-12 that is computed using the radiances at the shortest three wavelength channels assuming a functional form for the upper level profile. The upper and lower portions of the first guess are combined using a cubic spline (Bhartia et al., 1996).

The ozone climatology used to construct the variances information has been obtained from the best available satellite and balloon ozonesonde measurements. The *a priori* profile covariance matrix is constructed on the basis of a statistical analysis of the climatological data. For layers 1-5, the covariance of the Hohenpeissenberg data set about the fit values was used. For layers 6-12, the same process was applied to the SBUV data set, but with modifications to allow for the difference between the covariance of an ensemble of real profiles and an ensemble of climatological profiles. The off-diagonal elements linking layers in the separate sets were estimated subjectively. A single covariance matrix is used for all latitudes and times. Matrix values are presented in Appendix C.

3.2.7.2 Measurement Errors

A measurement covariance matrix is based on the uncertainties in both the measured and calculated Q-values. For the SBUV/2 retrievals, in addition to the 1.0 percent errors in the measured radiance and the 2.0 percent error in total ozone, the measurement error covariance matrix includes contributions from all errors in quantities that enter into the calculations of the multiple scattering correction and of the albedo that would be generated by the assumed profile. In particular, there is an allowance for a contribution from the errors in the ozone absorption coefficients that arise from variations in atmospheric temperature, about 0.5 percent. The contributions from errors in surface reflectivity and surface pressure are not included but are believed to be small.

3.2.7.3 Calculation of Albedos

The theoretical albedo used in profile retrieval is the sum of two parts:

a. Single scattered radiance.

b. The sum of multiply scattered radiance and that reflected from the surface (MSR).

The single scattered radiance is computed using equation (2). The MSR radiance is obtained from a look-up table. The same quantities are calculated for the MSR tables as for the total ozone tables (i.e., I_0, I_s, and f_2), except that I_0 for MSR includes only the difference between the results of scattering to all orders and those of single scattering. The MSR thus contains only the sum of the theoretical radiance from second order and higher scattering and the component reflected from the surface.

MSR is a significant component only at wavelengths longer than 290 nm. MSR is weakly dependent on profile shape (Taylor et al., 1980), but strongly dependent on total ozone, surface reflectivity, and solar zenith angle. The reason is that the stratosphere acts principally as an attenuator on the wavelengths that are multiply scattered - the longer wavelengths. Thus, the MSR component of the wavelengths used for profiling has the same overall characteristics as the full radiances used for total ozone.

As for total ozone, there are profile MSR tables for three standard latitudes: low-latitude (15°), mid-latitude (45°), and high-latitude (75°). Values for intermediate latitudes are obtained by linearly interpolating in latitude between the Q-values for the adjacent standard latitudes.

As part of the interpolation process for determining the MSR Q-values, the sensitivity of MSR Q-values to total ozone is calculated for each of the longer profile wavelengths. This sensitivity is used to calculate the variances and covariances associated with the MSR component for the measurement covariance matrix.

3.2.7.4 Inversion

The unknown ozone profile is represented by a vector x, whose components are the values for ozone content for each of the 12 layers. The single scattering integral equation, (5), is linearized by expanding in a Taylor series about the first guess profile x', and dropping second and higher order terms in the expansion. The resulting expression is suitable for an iterative profile solution and may be written in the following form:

$$[\ln Q(x)]_l = [\ln Q(x')]_l + \sum_k (\partial \ln Q_l / \partial \ln x_k) x'(\ln x_k - \ln x'_k), \quad (81)$$

where

Q = Q-value as defined in (4)

x = solution ozone

x' = ozone profile from previous iteration

k = layer index

1 = wavelength index.

The partial derivative coefficients in the second term on the right-hand side are calculated using the ozone profile for the previous iteration and constitute the weighting function. They measure the sensitivity of the radiance at a particular wavelength to changes in ozone in the different layers in the profile. In vector format, this equation becomes

$$y = y_n + K_n(x - x_n), \tag{82}$$

where

x = vector of ln x_k values for solution ozone profile

x_n = vector of ln xk values for ozone profile for iteration n

y = vector of measured values for ln Q_1

y_n = vector of values for n Q_1 calculated from x_n

K_n = matrix of values of weighting function $(\partial \ln Q_1 / \partial \ln x_k)$.

A solution profile is computed using the *a priori* and error information from the equation

$$x_{n+1} = x_0 + S_x K_n^T \left[K_n S_x K_n^T + S_e\right]^{-1} \left[y - y_n - K_n(x_0 - x_n)\right], \tag{83}$$

where

S_e = measurement covariance matrix

S_x = *a priori* covariance matrix

x_0 = *a priori* profile.

Convergence is determined by the size of $x_{n+1} - x_n$.

3.2.7.5 Validity Checks

Several checks are made to identify scans with missing or grossly abnormal values. If a scan fails any one of these checks, a profile error code of 4 through 9 is assigned and no profile is reported. This error code appears in word 157 of the output data record.

If measurements are missing at any wavelength used in the profile calculations, a profile error code of 9 is assigned. If a Best ozone value has not been computed in the total ozone algorithm, then a profile error code of 8 is assigned. Next, the reflectivity for the six longest wavelengths, those that are multiply scattered, is checked. If the reflectivity for any of these wavelengths is outside the range (-0.05, +1.05), or if the cumulative reflectivity change averages greater than 0.05 between adjacent wavelength channels (step scan positions in SBUV), then a profile error code of 7 is assigned. Such values for reflectivity usually indicate defective data.

The algorithm uses the 274 nm and 283 nm Q-values to calculate values for **C,** the cumulative ozone above 1 mbar, and σ, the ratio of the atmospheric scale height to the ozone scale height, assuming that the cumulative ozone x is a function of the pressure p (McPeters, 1980):

$$x = Cp^{1/\sigma}. \tag{84}$$

If σ is outside the range from 0.3 to 0.8, a profile error code of 6 is assigned. If C is greater than 3.0 milli-atm-cm or less than 0.5 milli-atm-cm, a profile error code of 5 is assigned.

The observed Q-values are compared with the initial Q-values calculated from the *a priori* profile, and residues r are calculated. A residue is defined by the following equation:

$$r = 100\left(Q_{obs} - Q_{calc}\right)/Q_{calc} \tag{85}$$

where Q_{obs} are the Q-values derived from the observed radiances, and Q_{calc} are the Q-values derived from an assumed profile, in this case, the first guess. If this initial residue is larger than 60 percent, a profile error code of 4 is assigned. If the scan passes all checks described thus far in this section, the ozone profile is computed and additional checks are made. A final residue is derived, using the computed profile to derive Q_{calc} of (71), and compared with the standard deviation (σ) of the observed measurements, obtained as the square root of the diagonal term of the measurement error covariance matrix. If the final residue is larger than 3σ, an error code of 3 is assigned. If total ozone returned by the profile algorithm differs by more than 3σ from the total ozone for profiling, derived from the Best total ozone returned by the total ozone algorithm, an error code of 2 is assigned. If the ozone derived for the three lowest altitude layers differs by more than 5σ from the climatology-derived initial estimate for those layers, an error code of 1, signifying lower-level anomaly, is assigned on the output data record. Aerosol contamination is discussed in greater detail in Section 7.6.

A profile that passes all these tests is considered a good profile and is assigned a profile error code of 0. For descending orbit (north to south) data, a value of 10 is added to the error flag.

3.2.8 Data Quality Flags

This material summarizes the discussions of the total ozone and profile error flags presented above in Sections 3.2.7.5 and 3.2.6.3. The data quality flags describe the quality of the retrieved ozone values. The flag values appear in words 26 ("THIR" total ozone flag), 40 ("non-THIR" total ozone flag), and 157 (profile flag) of the data record of the output data record. The data quality flags are two-digit. The units digit describes the optical path length, warns of a discrepancy between ozone values derived from different wavelength pairs, or explains why good ozone values could not be retrieved from the scan. The tens digit signifies whether the measurement was made on the ascending or descending part of the orbit. **Table 3.2-5** summarizes the significance of each of the flags.

Total ozone data quality degrades as the optical path of the ultraviolet radiation through the atmosphere increases. For the purpose of setting the total ozone data flag indicators, the path length is characterized by the product of air mass and total column ozone, in units of atm-cm. In the SBUV/2 viewing geometry, for a typical 350 milli-atm-cm (DU) column ozone amount, low path would represent all measurements with solar zenith angles less than 72.3°, high path would include measurements between 72.3° and 83.6°, and very high path would extend up to 88°. Data are not processed for solar zenith angles greater than 88°. A value of 4 for the units digit indicates that the differences among the three total ozone values derived independently from the three wavelength pairs are outside a selected tolerance. Flag 4 rarely occurs at small solar zenith angles. However, at large solar zenith angles, a user may wish to accept total ozone values with a data quality flag of 4 if noisy data are preferable to no data at all.

Table 3.2-5. Data Quality Flags

Code (Units Digit)	Total Ozone (Words 26,40)	Profile (Word 157)
0	Low path (air mass x total ozone < 1.5 atm-cm)	Good profile
1	High path (1.5 atm-cm ~ air mass x total ozone < 3.5 atm-cm)	Ozone for 3 lowest layers deviates from climatology; probable volcanic contamination
2	Very high path (air mass x total ozone> 3.5 atm-cm)	Profile total ozone inconsistent with Best ozone from total ozone algorithm
3	Spare	Large final residue
4	Large disagreement among A,B,C pair total ozone	Initial residue> 60%
5	Best total ozone and profile total ozone inconsistent	C outside 0.5-3.0 mbar
6	Spare	σ outside 0.3-0.8 mbar
7	Photometer and monochromator reflectivity differ by more than 0.05 between consecutive wavelengths	Reflectivity outside range -0.05 to 1.05, or changes by than 0.15
8	Reflectivity outside -0.05 to 1.05 range	No Best total ozone available
9	Derived total ozone outside range of tables	Bad counts or missing measurements
Tens Digit		
0x	Ascending part of orbit	
1x	Descending part of orbit	

4 Assumptions

4.1 CONTINUING ASSUMPTIONS

The assumptions made in the NP algorithm can be divided into two categories. First we list assumptions that are made in the Version 6 algorithm and will probably be made in the subsequent versions of the algorithm as well.

- The IFOV is characterized as a point source with a single solar zenith angle.
- The atmosphere is composed of ozone and Rayleigh scatterers.
- Instrument performance is consistent with the specifications in Section 5.
- Ozone below the scattering layer can be estimated using climatology.
- The cloud fraction is zero over permanently snow covered regions.

4.2 ASSUMPTIONS REMOVED IN FUTURE VERSIONS OF THE ALGORITHM

A second set of assumptions are made in the Version 6 algorithm, but will probably not be made in the subsequent versions of the algorithm when it becomes available.

- Ozone absorption over a finite band can be characterized by an effective absorption coefficient.
- Rotational Raman scattering is insignificant and can be ignored.
- The gravitational constant g is constant with altitude.
- Molecular orientations are isotropic in the atmosphere.
- Spherical effects on outgoing radiation are insignificant and can be ignored.
- The reflecting surface can be modeled as a single surface with an effective pressure and reflectivity.
- The first guess and *a priori* profile are the same.
- The multiple scattering and reflectivity radiance component is not a function of ozone profile shape.
- The cloud fraction is 0.5 over bright scenes in snow covered regions.

5 Input Data Requirements

5.1 PRIMARY SENSOR REQUIREMENTS

The sensor requirements for the nadir profile algorithm are based on the requirements of the adopted SBUV profile ozone algorithm, see **Table 5.1-1**.

Table 5.1-1. Heritage and Allocated Sensor Requirements

Sensor Parameter	Baseline Algorithm Needs	Baseline Sensor Allocation	Comments
Wavelength range	252-380 nm min. (252-306 for profile)	250-310 nm min. (310-380 nm from TC)	Ozone profiling, column, and refl.
Bandwidth (FWHM)	1.1 nm	1 nm	Pair/triplet approach
Samples/FWHM	1 min.	2.4	λ shift, Ring effect
Number of channels	13 discrete channels* (8 below 310 nm)	Hyperspectral coverage: 250-380 nm	Triplets, over-sampling, aerosols
Horizontal cell size	250 km @ nadir	250 km @ nadir	Heritage sampling
SNR	From SBUV/2 spec	SBUV/2 spec values for NP channels, 1000 for TC channels	Precision
Polarization sensitivity	<5%	<5%	Accuracy
λ registration	< 0.01 nm	< 0.01 nm	Ozone cross section error
Albedo calibration	2%	2%	Accuracy and stability
Pixel to pixel calibration (includes linearity)	1% max.	1% max.	Accuracy
Stray light, out-of-field	1% max. (integrated)	1% max.	Accuracy and stability
Stray light, out-of-band	1% max (all wavelengths)	1% max.	Accuracy and stability

* The 8 profiling wavelengths are: 251.97, 273.55, 283.08, 287.64, 292.27, 297.55, 301.93, and 305.80 nm. The wavelength channels from the total column focal plane are 312.49, 317.49, 331.22, 339.80, and 378.61 nm.

5.2 OTHER OMPS SENSOR DATA REQUIREMENTS

The V6 heritage profiling algorithm requires measurements of normalized radiance at four wavelength channels longward of 310 nm to estimate total column amounts for use in the profile retrieval process. These will be obtained from the nadir total column (TC) sensor by combining measurements from the smaller TC sensor FOV made at the same time that the NP sensor makes its measurement. This is accommodated by co-boresighting NP and TC FOV. Note that this requirement does not affect EDR threshold compliance. The Limb height registration function of the NP (see Section 6) is not affected by the total column determination, and the NP capability is provided as a link to heritage measurements rather than a measurement solution to meet profiling EDR thresholds.

Nonetheless, we want to provide the best possible continuity with previous data sets, and we want to provide a high-quality continuous spectrum of normalized albedo from 250 - 380 nm. In order to couple the NP and TC spectra, the latest version of the NP algorithm will be preferred. Residues from the latest version of the total ozone algorithm applied to the co-boresighted overlapping channels at around 306 nm and 309 nm will provide optimum information to intercalibrate the NP and TC spectra. This successful

coupling will position OMPS for possible technology insertion in the form of any new EDR Algorithms that may be developed out of the series of hyperspectral instruments now being flown. This is another good reason for positioning OMPS NP to adopt/adapt the latest version of the profiling algorithm when it becomes available.

5.3 OTHER NPOESS SENSOR DATA REQUIREMENTS

The current version of OMPS NP algorithm does not use any external EDRs. In the future, we expect that SBUV Version 6 algorithm will be replaced by SBUV Version 8 algorithm, which may use some external EDRs (surface pressure, cloud fraction, snow/ice flag, cloud top pressure, and temperature profile) to enhance data quality.

5.4 CLIMATOLOGY DATA REQUIREMENTS

The baseline software uses climatological data sets to provide estimates for modeling parameters to be used in absence of coincident measurements made by other sensors. For the future version (if external EDR is available) the baseline climatologies will be retained in our OMPS NP design strategy to provide for "graceful degradation" of the measurement system in the case of failures associated with other sensors. These include: surface pressure, cloud pressure climatology, snow/ice climatology, probably surface reflectivity climatology, and standard ozone and temperature profiles.

6 Output Data Description

6.1 PRIMARY DATA PRODUCT

The baseline output data are well described in the SBUV and SBUV/2 data user's guides. Included in this document (below) is the data record description of these data sets. It has been reproduced from the SBUV Ozone Products User's Guide (NASA REF. Pub. 1234, 1990) and updated to reflect more recent adjustments to the output format. Other data records including orbital header and trailer records contain further valuable information such as calibration information and quality flag statistics that will be included in the final OMPS NP data sets, and are described in both of the references cited above. An additional output of this system, discussed above in Section 5.2, is calibration information relating NP and TC spectra. The residues at the overlapping channels (probably 306 nm and 308 nm) will be fed back onto the NP SDR to complete the spectral radiance information resident there.

6.2 ADDITIONAL DATA PRODUCTS

From the retrieval of layer ozone, several other useful quantities are derived. An estimate of the total column ozone is produced. The Lambertian equivalent surface reflectivity of each measured scene is also calculated.

6.3 DATA CONTENT

PMF Record Format (also known as HDSBUV Tape format)

The PMF (Product Master File) format is used for input and output data by the SBUV and SBUV/2 processing algorithms. We use this format for OMPS NP processing. A separate adaptor module is supplied to convert the output of the NP SDR algorithm to the PMF format used by the OMPS NP processing algorithm.

4-Byte

Words	Description
1	Block identifier (Zx0 800); X = block number.
2	Logical sequence number (n+1) for n^{th} data record.
3	Orbit number.
4	Day and year at the start of scan (yyyyddd).
5	GMT (seconds).
6	Subsatellite latitude at beginning of scan (degrees, -90° to +90°, southern latitudes negative).
7	Subsatellite longitude at beginning of scan (degrees, -180° to +180°, western longitudes negative).
8	View latitude—average for total ozone (degrees).
9	View longitude—average for total ozone (degrees).
10	Solar zenith angle—average for total ozone (degrees).
11-14	Total column sensor N value for 380 nm channel
15-18	Four monochromator N-values (339.8 nm, 331.2 nm, 317.5 nm, 312.5 nm).
19	Gain selection flags for each of four wavelengths.
20	THIR processing code.
21	THIR Best total ozone (milli-atm-cm).
22	Cloud top pressure (reported by THIR).
23	Pressure of reflecting surface (estimated using THIR).
24	THIR average reflectivity.
25	THIR percent cloudiness B(3).

26 THIR error flag for total ozone.

27 A-pair total ozone (milli-atm-cm).

28 A-pair sensitivity (n-value/ milli-atm-cm).

29 A-pair average reflectivity.

30 A-pair weight.

31 B-pair total ozone (milli-atm-cm).

32 B-pair sensitivity (n-value/ milli-atm-cm).

33 B-pair average reflectivity.

34 B-pair weight.

35 Best total ozone (milli-atm-cm).

36 C-pair total ozone (milli-atm-cm).

37 Pressure of reflecting surface estimated without THIR.

38 Average reflectivity.

39 C-pair sensitivity (n-value/ milli-atm-cm).

40 Error flag for total ozone.

41 Table selection scheme index.

42 Snow/IceCode

10: Snow/Ice

0: NoSnow/Ice

-1: No information

43 Photometer-monochromator reflectivity difference.

44 Terrain pressure (atm).

45 D-pair total ozone (milli-atm-cm).

46 SOI (sulfur dioxide index).

47 B'-pair total ozone (milli-atm-cm).

48 View latitude—average for profile (degrees).

49 View longitude—average for profile (degrees).

50 Solar zenith angle—average for profile (degrees).

51-58 Eight photometer N-values (profile wavelengths 255.5 nm, 273.5 nm, 283.0 nm, 287.6 nm, 292.2 nm, 297.5 nm, 301.9 nm, and 305.8 nm).

59-66 Eight monochromator N-values (profile wavelengths).

67-68 Gain selection flags for each of eight wavelengths (one REAL*8 word).

69-80 *A priori* profile individual ozone amounts (milli-atm-cm) in 12 layers (see Appendix A).

81 Total ozone (milli-atm-cm) for *a priori* profile.

82-91 Q-values corrected for multiple scattering and surface reflectivity (255.5 nm through 317.5 nm).

92-101 Initial residues (255.5 nm through 317.5 nm) in percent.

102-106 Multiple-scattering and reflectivity correction to Q-values for five longer wavelength channels (297.5 nm through 317.5 nm).

107-111 Monochromator reflectivities for five longer wavelength channels (297.5 nm through 317.5 nm).

112-116 Sensitivity of multiple-scattering correction to total ozone for five longer wavelength channels (297.5 nm through 317.5 nm).

117-121 Multiple-scattering mixing fraction for five longer wavelength channels (297.5 nm through 317.5 nm).

122-131 Final residues (255.5 through 317.5 nm) in percent.

132-143 Solution profile individual ozone amounts (milli-atm-cm) in 12 layers (see Appendix A).

144-155 Standard deviations for solution profile individual ozone amounts (%) in 12 layers, SBUV layer 1 first.

156 Total ozone (milli-atm-cm) for solution profile.

157 Profile error code.

158-159 Parameters C and sigma (σ).

160-178 Solution mixing ratio (ppmv) at 19 pressure levels; 0.3 mbar first.

179-190 Standard deviations for *a priori* profile individual ozone amounts (%) in 12 layers.

191-200 Standard deviations for Q-values corrected for multiple scattering and reflectivity *(*255.5 nm through 317.5 nm) in %.

201 Number of iterations for profile solution.

202 VCI (Volcano Contamination Index).

203 Non-sync Flag

204 D-pair sensitivity (n-value/ milli-atm-cm).

205 B-pair sensitivity (n-value/ milli-atm-cm).

206 Solar zenith angle at start of scan (radians x 104).

207 Solar zenith angle at end of scan (radians x 104).

All words are in IBM floating-point format (REAL*4) except word 1, which contains hexadecimal data. Any word in the record may contain -77, indicating fill data.

PMF Record Format – Detailed Description of Selected Words of Data Record

Words ***Comment***

2 Contains positive value 2 or larger for data record.

11-18 N-value is computed from each measurement as $N = -100 \log_{10}(1/F)$,

where I = measured radiance and F measured solar irradiance.

19 Gain selection flags are packed into a 4-byte REAL word, with the 339.8 nm gain being the most significant byte.

20 Cloud processing code (describes quality of THIR data):

<0: Quality information not available; THIR data not used.

0-3: Describes quality of THIR cloud data used by algorithm; a larger number signifies poorer quality: 0 is best, 3 is lowest quality acceptable for use by algorithm.

>3: Quality of THIR data extremely poor; THIR data not used by algorithm.

21-26 Final output of total ozone processing using the cloud information from the THIR instrument—total ozone is value above actual terrain height; Contains -77. if THIR data not available.

28, 32 Sensitivity of a pair is defined as $\Delta Np/\Delta\Omega$ □where AN is the difference in 39 the N-value of pair wavelengths and $\Delta\Omega$ is the difference in the total ozone.

30, 34 Weighting factor given to pair in Best ozone computation using equation (76), $W_C=1 - W_A - W_B$.

35, 37 Final output of total ozone processing using the cloud information

38, 40 As provided indirectly from the measured reflectivity. Total ozone is value above actual terrain height.

26, 40 Error flags are defined as follows (further discussion of the error codes appears in Table 3.2-5):

0 - Low path length, good scan.

1 - High path length, good scan.

2 - Very high path length, good scan.

3 - Spare.

4 - Inconsistency between Best ozone and largest weighted ozone pair value.

5 - Inconsistency between Best ozone and profile total ozone (difference >3□)

6 - Spare.

7 - Photometer and monochromator reflectivities differ by more than 0.15.

8 - Reflectivity out of range (-0.05,1.05).

9 - Best total ozone exceeds the dynamic range of the tables.

The dynamic ranges are as follows:

Latitude <15° 180 to 350 DU

Latitude 15°to 45° 180 to 600 DU

Latitude >45° 180 to 650 DU.

(10 is added to the error flags for descending orbit data).

41 Table selection scheme index is a real number valued 1.0 - 3.0 indicating the relative weight given to standard profiles from

1.0 Equatorial profiles

2.0 Mid-latitude, and

3.0 High latitude.

46 Sulfur dioxide index; can be used to infer the presence of volcanic $S0_2$

59-66 N-values for eight wavelengths in the following order—word 59: 255.5, 66: 305.8 nm.

67-68 Packed as in word 19, 305.8 being the most significant digit. (one REAL*8 word) NB: Must be read as a single REAL*8 word, not two REAL*4 words.

69-80 *A priori* profile amounts in SBUV layers, layer 1 first.

81 Total ozone above 1 atm for *a priori* profile, not necessarily above actual terrain height.

82-131 The following comments apply to these words:

$Q = [4\pi I/F]\beta P(\theta_0)$, where

I= intensity of the backscattered radiation

β= Rayleigh scattering coefficient

F = solar flux

Q-values for wavelengths are as defined in equation (4); that is, $P(\theta_0)$= Rayleigh scattering phase functions.

The residue is defined as follows: 100(Qobs - Qcalc)/Qcalc, where

Qobs = Q-value calculated from an assumed radiance and solar flux

Qcalc = Q-value calculated from an assumed profile

Qmsr = Q-value that refers only to the multiple-scattered and reflected component of the total intensity (obtained from a lookup table).

The Q-values and other related quantities are given in order from the shorter to the longer wavelengths. In words 102 through 121, values for wavelengths shorter than 297.5 nm are assumed to be zero.

Words reserved for 312.5 nm contain valid data only when this wavelength is used.

82-91 Qcorrected = Qobs - Qmsr.

92-101 Residue derived using Qcalc obtained from first guess profile.

102-106 Qmsr.

122-131 Residue derived using Qcalc obtained from final solution profile.

156 Total ozone above 1 atm for solution profile.

157 Error flags are defined as follows: (Further discussion of the error codes appears in Table 3.2-5).

0 - No error.

1 - Lower level anomaly; probable aerosol contamination.

2 - Inconsistent total ozone and profile total ozone (>3σ).

3 - Final residue> 3σ.

4 - Measured Q-value differs by more than 60% from Q-value calculated with a priori profile.

5 - C greater than 3.0 milli-atm-cm or less than 0.5 milli-atmcm.

6 - Sigma greater than 0.8 or less than 0.3.

7 - Reflectivity less than -0.05 or greater than 1.05, or changes by more than 0.05 from wavelength to wavelength.

8 - No Best total ozone available.

9 - Missing measurements or bad counts.

(10 is added to the error flag for descending orbit data.)

158-159 Parameters determined by assuming an ozone profile of the form:

$$x(p) = \underline{C} p^{1/\sigma}$$

where p = pressure in mbar,

x = cumulative ozone at pressure level p and

C = cumulative ozone at 1 mbar (milli-atm-cm).

160-178 Values of the solution profile volume mixing ratios are given in order of increasing atmospheric pressure at the 19 pressure levels: 0.3, 0.4, 0.5, 0.7, 1.0, 1.5, 2.0, 3.0, 4.0, 5.0, 7.0, 10, 15, 20, 30, 40, 50, 70, and 100 mbar. Volume mixing ratio (ppmv) = mass mixing ratio/l.657.

202 Volcano Contamination Index can be used to identify whether the derived profiles below 5 mbar are incorrect because of scattering by aerosols (See Section 7.6 for examples and explanation of use).

7 System Accuracy and Precision

This section is out of date. The analysis on system accuracy and precision will likely be moved to error-budget documentation and therefore has not been updated here.

7.1 ACCURACY AND PRECISION OF ALBEDO

The accuracy of the albedo derived from BUV measurements depends on the accuracy of the pre-launch radiance and irradiance calibration constants. The accuracy of the pre-launch calibration depends, in turn, primarily upon the radiometric accuracy (± 3 percent) of the standard calibration lamp supplied by the National Institute of Standards and Technology (NIST). The ratio of radiance and irradiance calibration constants used to calibrate the normalized radiance used in the retrieval algorithm, however, is not affected by the lamp calibration and will be known to better than ± 2% for the OMPS nadir profiler.

The accuracy of the calibration of the long-term albedo relative to the first day of measurement depends primarily on the accuracy in characterizing time-dependent changes in the diffuser plate. The use of a diffuser carousel has been shown to reduce this uncertainty. It is now estimated that after 7 years of in-orbit operation, the change in diffuser plate reflectivity can be determined to within ± 0.5%.

In addition to changes in sensitivity, uncertainties in the instrument wavelength scale can lead to uncertainties in the retrieved ozone. The algorithm is based on the assumption that the instrument measures radiances and irradiances at known wavelengths and bandpasses. If the wavelengths of measurement are not those specified, then the relation between ozone and backscattered radiation will not be that assumed by the algorithm, leading to an error in the retrieved ozone. For the OMPS nadir profiler, these uncertainties will be small, as shown in Section 3.1 describing wavelength calibration using spectral analysis of the measured solar spectrum.

In summary, it is estimated that the albedo calibration of the OMPS nadir profiler will be accurate to ± 2% at all wavelengths immediately after launch and may drift up to ± 0.5% over the nominal lifetime of seven years.

7.2 RELATION BETWEEN ALBEDO ERRORS AND OZONE ERRORS

Table 7.2-1 shows how a positive 1 percent error in all measured albedos affects the derived profile and total ozone in the mid-latitudes. The effect on the total ozone (minus 0.3 percent) is relatively small compared to the effect on the profile above 10 mbar (minus 1 to 2 percent). When the albedo increases, the derived ozone is expected to decrease, in the same way as it does in the higher altitudes of the profile and for total ozone, as shown in Table 7.2-1. However, at lower profile altitudes, ozone increases for higher albedos. The increase occurs because the computed profile is constrained to a profile-derived total ozone. Because the change in profile-derived total ozone is less

than the overall change in ozone in the higher altitudes of the profile, the profile algorithm compensates for this difference by adding some ozone in the lower levels of the profile (levels below the maximum concentration).

Table 7.2-1. Effect of 1% Change in Albedos at All Wavelengths on Derived Mid-latitude Ozone

Pressure (mbar)	Effect on Derived Ozone (percent)
0.3	-1.20
0.4	-1.43
0.5	-1.60
0.7	-1.81
1.0	-1.92
1.5	-1.87
2.0	-1.70
3.0	-1.36
4.0	-1.16
5.0	-1.04
7.0	-0.91
10.0	-0.82
15.0	-0.62
20.0	-0.38
30.0	0.03
40.0	0.35
50.0	0.54
70.0	0.56
100.0	0.25
Total Ozone	-0.3

Table 7.2-2 summarizes the estimated absolute errors in the derived ozone profile. Such errors do not change with time. These errors are provided as a function of error source and altitude. Line 3 shows the error in ozone resulting from the uncertainty in the wavelength calibration of the instrument, as discussed in Section 7.1. Line 4 shows the error resulting from the uncertainty in the prelaunch radiometric calibration. Random errors are summarized in **Table 7.2-3**. Line 1 shows the altitude dependence of the uncertainty in ozone arising from instrument noise. In all cases, the uncertainty in ozone at a given altitude depends upon the wavelengths used in determining the ozone for that altitude, the uncertainty in the measurement at those wavelengths, and the sensitivity of the retrieved ozone to a change in the albedo at that wavelength.

Table 7.2-2. Time-Invariant Errors (Accuracy) in Retrieved Ozone

Error Source	Ozone Mixing Ratio Error (%)			
	1 mb	3 mb	10 mb	30 mb
1) Rayleigh Scattering Coefficient (c)	0.5	0.5	0.33	0.17
2) Ozone Absorption Cross-Section (b,c)	3	3	3	3
3) Wavelength Calibration	0.10	0.15	0.55	0.25
4) Radiometric Calibration	5.01	3.44	2.21	0.87
5) Retrieval Error (c)	3	2	4	5
Root Sum of Squares of Sources 1 Through 5	6.58	5.01	5.50	5.90
Heritage (SBUV) Error	7	5	5.5	6

Notes: a) Possible error in mid-latitude profiles (1σ) from each error source is listed.
b) This error applies only to OMPS comparisons with non-UV instruments. With other BUV sensors, errors should be less than 1%.
c) These errors may be ignored when comparing similar BUV instruments on different satellites.

Table 7.2-3. Random Errors (Precision)

Error Source	Ozone Mixing Ratio Error (%)				
	1 mb	3 mb	10 mb	30 mb	Total Ozone
1) Sensor Noise	2.0	1.6	1.2	0.9	0.1
2) Atmospheric Temperature	0.5	1	1	1	1
3) Retrieval Error	5	3.5	4	10	2
(Sum σ^2)^{½} of Sources 1 Through 3	5	4	5	10	2
Heritage (SBUV) Error	5	4	5	10	2

Notes: Errors listed are rms values for typical mid-latitude measurements. During winter months or under disturbed atmospheric conditions errors 2 and 3 may be larger by a factor of 2.

Vertical resolution of buv-derived profiles is 10 km. Listed errors are applicable only at this resolution (see also Section 7.4).

7.3 INPUT PHYSICS

Calculation of the absorption and scattering of atmospheric radiation by ozone and the other constituents of the atmosphere requires knowledge of the ozone absorption and Rayleigh scattering coefficients. The values used in the algorithm are obtained from laboratory measurements. Any uncertainty in the laboratory values will propagate through the algorithm to produce a systematic error in the derived ozone. Lines 1 and 2 of Table 7.2-2 show the altitude dependence of the effect of these uncertainties. In addition, the absorptivity of ozone is a function of the temperature. As the temperature changes, the absorption coefficient may change from that assumed in the algorithm, producing an error in retrieved ozone. The size of this error is shown in line 2 of Table 7.2-3.

7.4 PROFILE RESOLUTION

The vertical resolution of the ozone profiles retrieved from BUV depends upon the width of the radiance weighting functions and, to a lesser extent, on the separation between the weighting functions. The weighting functions of the five shortest SBUV wavelengths (252 nm to 292 nm) have values of full width at half maximum (FWHM) of about 10 km and peaks separated by 2-3 km. The longer wavelengths have wider weighting functions, whose FWHMs range from 15 km to 25 km, and whose peak separations increase to 5 km. These fundamental properties of the weighting functions, determined by the selection of wavelengths, the physics of radiative transfer and the vertical distribution of ozone in the Earth's atmosphere, limit the amount of information the measured radiances can provide regarding the vertical distribution of ozone.

Two approaches have been taken in estimating the resolution of the profiles derived from the BUV algorithm. In one, the response of the algorithm to a very narrow perturbation in the atmosphere is calculated. In the other, the profiling system is treated as operating on the atmospheric properties as a bandpass filter, called the averaging kernel.

7.4.1 Perturbation Studies

In these studies, a perturbation is applied to the atmospheric ozone profile, the albedos that would be produced by the perturbed profile are calculated, and the algorithm is applied to these albedos to retrieve a profile in the same way as it would be applied to measured albedos. The retrieved profile is compared with the profile used to calculate the albedos. **Figures 7.4-1** and **7.4-2** show the results of two such calculations. In both cases, the change in ozone has a Gaussian shape and is centered at the 3 mbar level. The solid line shows the percentage difference between the perturbed and unperturbed profile; the dashed line shows the ratio of the retrieved profile to the unperturbed profile. The agreement between the two is a measure of how well the algorithm can reproduce the structure represented by the perturbation. Figure 7.4-1 shows the results of a study where the maximum change is 10% and the FWHM is 10 km; Figure 7.4-2 shows the results for a perturbation with the same maximum amplitude but with a FWHM only half as wide.

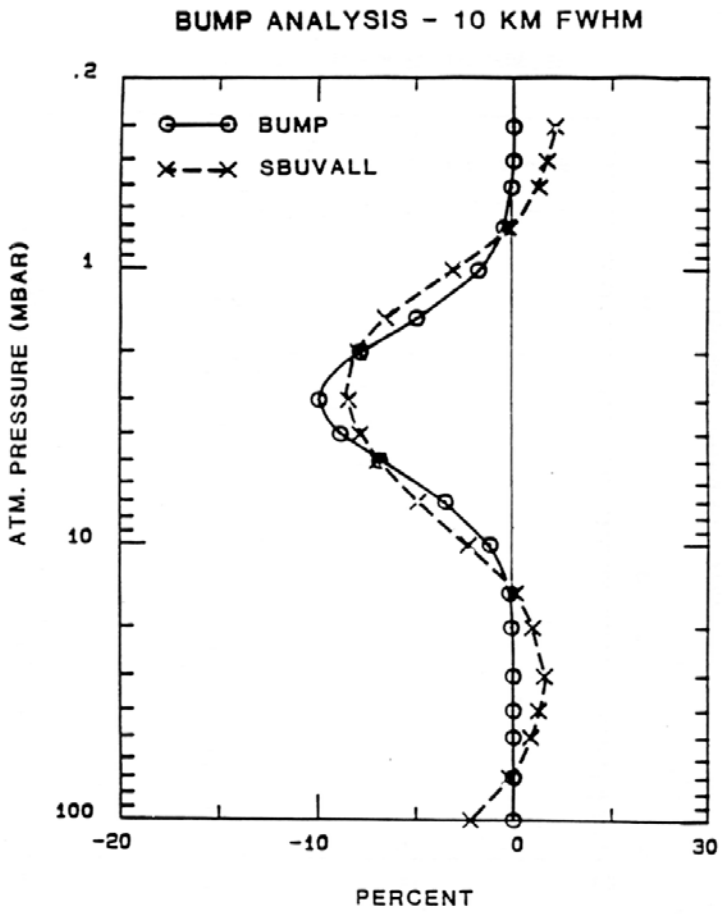

Figure 7.4-1. Effect on retrieved ozone of 10% Gaussian change in ozone, centered at 3.0 mbar with 10 km full-width at half-maximum

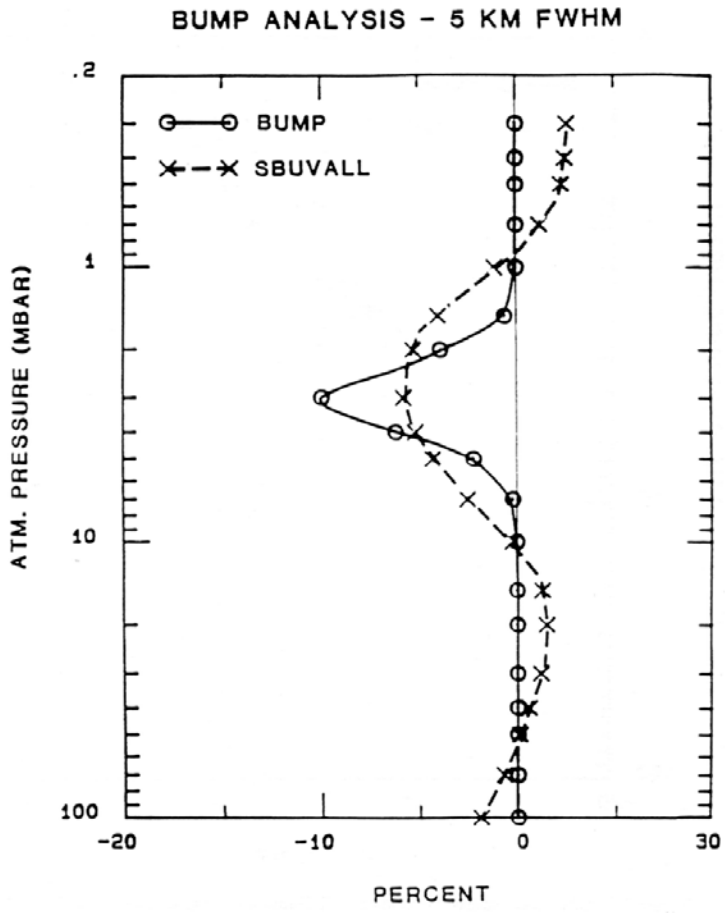

Figure 7.4-2. Effect on retrieved ozone of 5% Gaussian change in ozone, centered at 3.0 mbar with 5 km full-width at half-maximum

These figures show that, while the algorithm can still retrieve a change in ozone in the appropriate region of the atmosphere, the agreement between the altitude dependence of the retrieved and assumed ozone changes is markedly poorer for the 5 km FWHM perturbation.

7.4.2 Averaging Kernels

In the averaging kernel approach the profiling system is regarded as a bandpass filter, called the averaging kernel. The profile retrieved by the algorithm in this concept is the convolution of the averaging kernel with the actual ozone profile. The FWHM of this filter defines the resolution of the profiling system. Other properties of the averaging kernel are also analogous to those of a typical bandpass filter, such as an asymmetric bandpass or out-of-band response.

Figure 7.4-3 is a plot of these kernels at selected pressure levels. The results shown are for a measurement made near the equinox in mid-latitudes, but results for other situations are similar, except at very high solar zenith angles, where all the kernels shift upward by up to 5 km. **Table 7.4-1** summarizes the properties of the averaging kernels at the 19 pressure levels at which mixing ratios are reported. The peak or mode is the pressure, in mbar, at which the averaging kernel has its maximum value. The error of the peak is the difference in *kilometers* between the actual height of each pressure level and the height where the averaging kernel has its peak value. Positive values signify that the actual height of the pressure level is above that of the peak of the averaging kernel for that level.

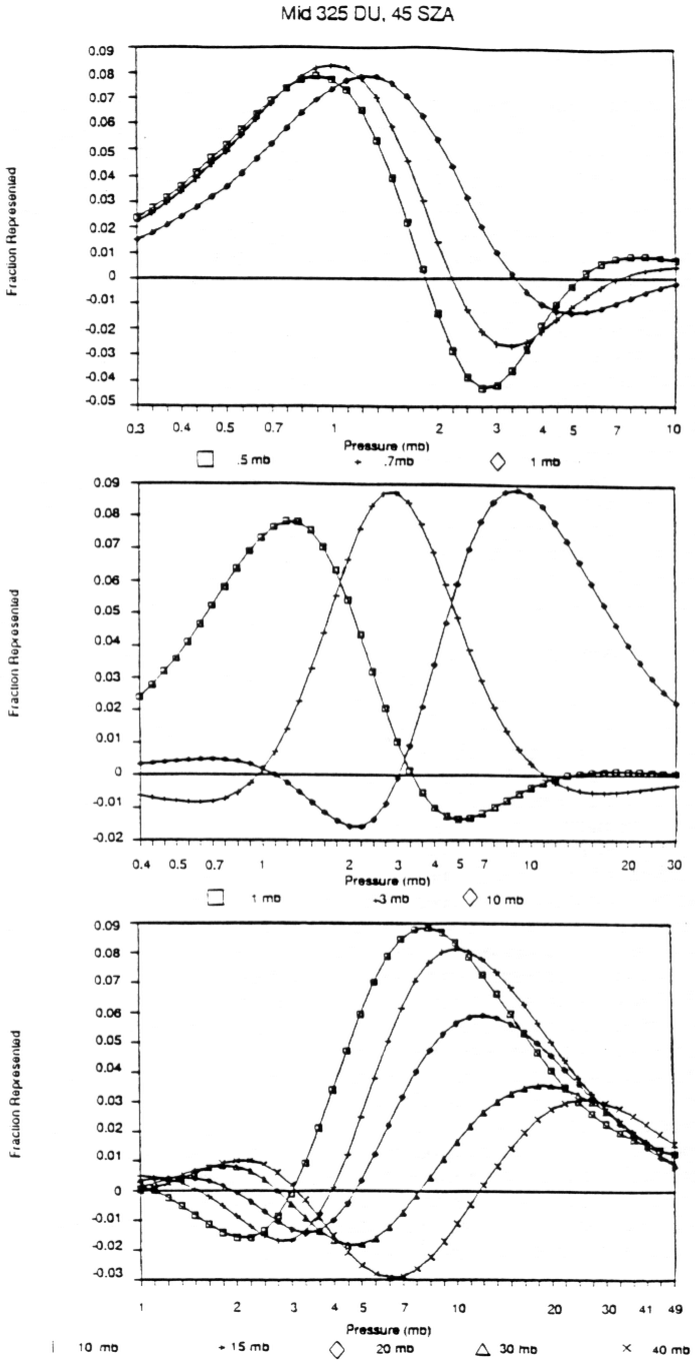

Figure 7.4-3. Nadir Profile Retrieval Averaging Kernels

Table 7.4-1. Properties of Averaging Kernels

Pressure (mb)	Peak (mb)	Error of Peak (km)	FWHM (km)	Out-of-Band/ In-Band
0.3	.8	6.8	8.2	.35
0.4	.9	5.6	8.7	.26
0.5	.9	4.1	8.7	.21
0.7	1.0	2.5	9.6	.13
1.0	1.3	1.8	10.2	.08
1.5	2.0	2.0	8.5	.12
2.0	2.4	1.3	7.6	.13
3.0	3.0	0.0	7.9	.16
4.0	3.8	-0.4	8.4	.11
5.0	4.5	-0.7	7.9	.06
7.0	6	-1.1	8.7	.06
10.0	8	-1.5	10.0	.06
15.0	10	-2.8	9.7	.07
20.0	12	-3.5	9.8	.14
30.0	20	-2.8	8.9	.47
40.0	25	-3.3	8.3	.67
50.0	30	-3.5	9.0	.37
70.0	40	-3.9	10.8	.18
100.0	45	-5.5	11.2	

Because of these differences between the location of the mode of the averaging kernel and the pressure level, a change in ozone that affects a region of the atmosphere on the order of or smaller than the FWHM given in Table 7.4-1 will be reported at the wrong altitude. The mode error is the maximum possible error of this kind that can occur. The out-of-band to in-band ratio is the ratio of the fraction of the system response not located between the two zeroes surrounding the mode to that between the two zeroes. A large out-of-band fraction for a level means that changes at levels far away from a given pressure level may affect the derived results for that level.

In general, the averaging kernels between 0.7 mbar and 20 mbar have “reasonable” properties; the likelihood that the algorithm will report misleading information between these altitudes is small. At higher solar zenith angles (> 80 degrees) the upper limit moves up to 0.3 mbar. Outside these limits, the resolution of the derived ozone profiles depends strongly on the validity of the *a priori* assumptions made in the retrievals.

For the upper levels (0.3 mbar to 1 mbar), the key *a priori* assumption is that the ozone profiles have a constant scale height (in pressure units); i.e., log $p(O_3)$/1og p is constant, where $p(O_3)$ is the ozone partial pressure and p is the atmospheric pressure. In the lower levels, the key *a priori* assumption in the algorithm is that the fractional variance of the ozone in layer 2 is almost 2 orders of magnitude larger than that in layer 5, fractional variances of other intermediate layers falling in between. The ozone balloonsondes show this behavior very clearly for short-term to mid-term (seasonal) variations in ozone. For longer term variations, however, the validity of these

assumptions is not certain. Current photochemical theories do suggest that the changes in layer 5 (around 20 mb) are likely to be the smallest.

The derived ozone in the 20 mb to 100 mb range agree extremely well with balloonsonde results and, therefore, may be usable for those scientific studies where a high degree of accuracy is not required or when no other source of reliable information—such as the study of global ozone fields, meridional transport, or estimation of ultraviolet flux at different altitudes in the atmosphere—is available. For studies requiring a high degree of accuracy, such as studies of long-term trends in ozone, users are advised to study the sum of ozone in layers 2, 3, and 4 rather than the reported ozone mixing ratios in the 20 mb to 100 mb range. Error studies show that the *a priori* information largely determines how ozone is distributed among the three layers, whereas the instrumental measurements determine the sum of the ozone amounts in the three layers.

The estimated systematic errors in ozone due to the retrieval process are given in line 3 of Table 7.3-2; the random errors appear in line 3 of Table 7.3-3.

7.5 LONG-TERM DRIFT

Table 7.5-1 presents the estimates of uncertainty in determining long-term trends. Two of the sources of uncertainty are instrumental effects discussed in Section 7.1: a possible change with time in the wavelength calibration and a possible change in the correct radiometric calibration constants. Estimates of the size of these effects appear in the first two lines of Table 7.5-1. A third source of uncertainty arises from a possible long-term temperature change and its effect on ozone absorptivity. This effect is discussed in Section 7.3. The possible time-dependent error is estimated on line 3. The remaining two sources of error in Table 7.5-1 are associated with possible changes in ozone in layers where SBUV cannot measure ozone directly.

Table 7.5-1. Experimental Uncertainties in Measuring Long-Term Ozone Trend

Error Source	Ozone Mixing Ratio Error (%)				
	1 mb	3 mb	10 mb	30 mb	Total Ozone
1) Wavelength Calibration	0.0/T	0.01/T	0.01/T	0.01/T	0.02/T
2) Radiometric Calibration	1.0/T	0.7/T	0.5/T	0.5/T	0.5/T
3) Atmospheric Temperature	0.02/°K	0.05/°K	0.1/°K	0.15/°K	0.15/°K
4) Tropospheric Ozone		0.0/% Change			0.05% Change
5) Ozone Above 0.3 mb	0.1/% Change			0.01/% Change	

Notes: The value of T in error sources 1 and 2 is equal to the number of years of instrument data used for analysis. For OMPS, T is 7 years. The values given apply to mid-latitude retrievals.
Errors 3, 4, and 5 are given as an ozone error due to changes in the relevant atmospheric parameter. If these changes are known from external sources, the derived ozone values can be corrected using these numbers. So, these errors are correctible using external data sources.

The algorithm for retrieving profiles requires that the sum of the amounts of ozone in individual layers, calculated from measurements at the shorter, profiling wavelengths, equal an independently measured total ozone value. However, the radiances used to derive the ozone profile by SBUV are not sensitive to changes in tropospheric ozone. Should tropospheric ozone change, derived total ozone will change, but the radiances will be relatively unaffected. In such a case, the algorithm will assume the wrong total amount of ozone in the layers it is calculating. This ozone deficit or excess will appear in the profile, at the highest pressures or lowest altitudes. This error is listed on line 4 of Table 7.5-1. The wavelengths at which SBUV measures albedo do not provide enough information to monitor changes in ozone above 0.3 mbar. Nevertheless, if ozone in these layers changes, there will be a slight effect on the albedos at the shortest wavelengths, and, therefore, on the ozone derived at higher pressure. Line 5 shows the magnitude of this effect. The errors in the changes of ozone with time estimated in lines 3, 4, and 5 of Table 7.5-1 are errors that would be produced by plausible changes in temperature, tropospheric ozone, or ozone above 0.3 mbar. If independent measurements of any of these quantities were available, they could be used to correct the derived ozone values and eliminate that source of uncertainty in the trend.

7.6 CONTAMINATION FROM VOLCANIC ERUPTIONS

The three eruptions of El Chichon in southern Mexico between 28 March and 6 April 1982 and the eruption of Mt. Pinatubo on June 15, 1991 injected significant amounts of sulfur-containing gas and dust into the tropical stratosphere. The principal sulfur gas in volcanic eruptions was S02, which changes in time to H_2SO_4 aerosol.

When gaseous S02 is present, it absorbs in several bands in the 290 nm to 320 nm range, some of which coincide with wavelengths used by SBUV to measure ozone. When aerosols form, enhanced scattering is expected, in particular at the 297.5 nm, 301.9 nm, and to a lesser extent, at the 305.8 nm wavelengths used to measure ozone.

Thus, in the first days after the El Chichon eruption for example, the data reflect these two opposite effects. Some tropical areas show the increased radiances from aerosol scattering, while others show the decreased values caused by S02 absorption. By early June only anomalous increased radiances occur in the data, as the S02 gas is converted entirely to aerosol. Thus, the only relatively long-term effects of major eruptions such as El Chichon or Pinatubo on the BUV data are increased radiances caused by aerosol scattering.

Because the effect of aerosol on the longer wavelengths used to determine total ozone is relatively small, the accuracy of derived total ozone is not significantly affected, even when stratospheric aerosol levels are highest. The use of ratios of albedos for pairs of wavelengths further reduces the impact of any anomalous increase in radiance from the aerosols. On the other hand, the anomalous increased radiances at the three ozone measurement wavelengths listed above significantly affect the accuracy of the ozone profile. For these increases in radiance, the profile algorithm derives a significant decrease in ozone in the middle stratosphere, where most of the ozone resides. The profile from the altitudes of the 5 mbar pressure level downward is affected. Because the algorithm requires that the sum of the ozone amounts equal total ozone, and because total ozone is practically unaffected, the profile algorithm is forced to increase the ozone at some other layer. This increase occurs where the derived ozone is least sensitive to the measured albedos, in Umkehr layers 1-3, from 64 mbar to the surface. Because the normal ozone content of these layers is low, the distortion of the albedos by aerosol produces a very large anomalous increase in the profile ozone for Umkehr layers 1-3. Thus, the profile algorithm can detect the presence of very small amounts of stratospheric aerosols by monitoring the anomalous increases in ozone for Umkehr layers 1-3.

The degree to which tropospheric ozone for a particular profile deviates from the values expected from climatology is described by the Volcano Contamination Index (VCI). The VCI is expressed in units of the climatological standard deviation of the tropospheric ozone value for a given latitude. For example, a VCI of 5.0 represents a profile with a tropospheric ozone value 5.0 standard deviations larger than the climatological average.

When the VCI is *5.0* or greater, the profile error flag is set to 1. This error flag does not screen all the data contaminated by aerosol but only that which is most significantly affected. *Unflagged data, in particular unflagged data with VCI between 2 and 5, can still have significant aerosol contamination.* Consequently, ozone profiles with values of the VCI between 2 and 5 should be rejected if they are in the neighborhood of profiles with a VCI greater than 5. In addition, ozone profiles from other extended regions where the VCI is consistently above 2 should also be considered suspect.

The VCI derived for an aerosol layer of a given optical thickness is very sensitive to the height of the layer. Calculated simulations show that aerosols below 20 km would be indistinguishable from normal tropospheric clouds. Thus, even when significant aerosol is present, it has relatively little impact on the profile if it is sufficiently low in the atmosphere.

Krueger (1985) describes a function related to the amount of S02 present that is denoted as the SO2 Index (SOI). This index can be expressed as the following function of the N-values for BUV measurements:

$$SOI = [32.21N_{340} - 60.88N_{331} + 51.69N_{318} - 23.03N_{312} \\ -1.8 - 59.3s\Omega - 47.6(s\Omega)2 + 59.3\Omega]/s, \quad (86)$$

where s is slant path 1+secθ_0, Ω is Best ozone, and θ_0 is solar zenith angle. The SOI appears on the output data record as word 46. The SOI was output because it has proved useful in deriving S02 amounts from TOMS data; however, examination of selected scans has shown that the SOI from SBUV is not a reliable measure of atmospheric S02.

7.7 STRAY LIGHT SENSITIVITY STUDY

The stray light error characteristics of the OMPS Nadir Profile sensor are expected to be similar to the SBUV/2 sensor. There is virtually no or limited data available on the SBUV/2 stray light. Based on historical SBUV/2 data, Larry Flynn has constructed a model for the out-of-band (OOB) stray light,

$$\text{Corrected } I_\lambda / F_\lambda = \text{Measured } I_\lambda / F_\lambda - C_\lambda \text{ Measured } I_p / F_p \quad (87)$$

where C_λ = {9, 7, 7, 6, 6}E-5 is a series of constants which are wavelength dependent for the shortest five wavelengths {252, 273, 283, 288, 292} nm, and I_p/F_p is the ratio of the photometer albedo at 378 nm.

In order to analyze the sensitivity of the Nadir Profile algorithm to stray light, we processed simulated NP radiance data using the M325 standard TOMS atmosphere with random noise associated with the OMPS NP SNR plus additional values for various NP stray light models. The retrieval results were compared to the inversion results without the additive stray light. The stray light models included Larry Flynn's SBUV/2 model for OOB stray light and the OMPS NP sensor allocations.

Figure 7.7-1 presents these models where the stray light is reported as the percent of the channel radiance. The thin dashed (brown) line is the SBUV/2 stray light (SL) model described above. The solid (blue) line with circles is the OMPS NP allocation for OOF stray light. The symbols with the large rectangles (pink) represent the OMPS OOB stray light allocation.

Figure 7.7-2 presents the retrieved results as a function of pressure where we show the comparison with and without stray light as a systematic error. The lines have the same legend as indicated above. In the figure we have added an additional set of lines

representing the 'Allocated' Ozone Error to the NP sensor stray light. Since this allocation is not currently explicitly defined in the algorithm Development Specification, we constructed it from the SBUV accuracy error defined in Table 7.2 of the SBUV Ozone Product User's Guide. The SBUV error table does not include some radiometric error terms, (viz., pixel-to-pixel non-linearity, polarization, and stray light). These we include. The stray light component of the allocated error is the quadrature difference between the total SBUV error (column 1) and the remaining error terms. The result of this analysis is summarized in the **Table 7.7-1**.

Table 7.7-1 Error allowance for stray light

P (mb)	Accuracy	Ray	O3	Waveln	Algo	Cal	Non-Lin	Polar	Stray Light	Stray Light
	SBUV					Radiometric			OOB	OOF
1	7.00%	0.50%	3.00%	0.10%	3.00%	3.80%	0.40%	1.90%	2.50%	2.50%
3	5.00%	0.50%	3.00%	0.15%	2.00%	2.80%	0.03%	1.40%	0.98%	0.98%
10	5.50%	0.33%	3.00%	0.55%	4.00%	1.60%	0.71%	0.80%	0.75%	0.75%
30	6.00%	0.50%	3.00%	0.25%	5.00%	0.06%	0.50%	0.03%	0.85%	0.85%

The allocated stray light is equally divided between OOB and OOF and is represented given as:

$$\text{OOB (OOF) SL} = \text{SQRT}[((\text{Accuracy})^2 - (\text{Ray})^2 - (\text{O3})^2 - (\text{Waveln})^2 - (\text{Algo})^2 - (\text{Cal})^2 - (\text{Non-Lin})^2 - (\text{Polar})^2)/2)]. \quad (88)$$

We have demonstrated the sensitivity of the NP Algorithm to stray light levels. The allocated OOB and OOF stray light meet the requirement that is based on the SBUV/2 radiometric error. The performance results are tabulated below in the **Table 7.7-2**.

Table 7.7-2 Allocated and computed errors for stray light

Pressure	OOB Stray Light		OOF Stray Light	
(mb)	Allocated	Performance	Allocated	Performance
1	2.50%	1.83%	2.50%	1.83%
3	1.00%	0.83	1.00%	0.83
10	0.75%	0.52%	0.75%	0.52%
30	0.85%	0.41%	0.85%	0.41%

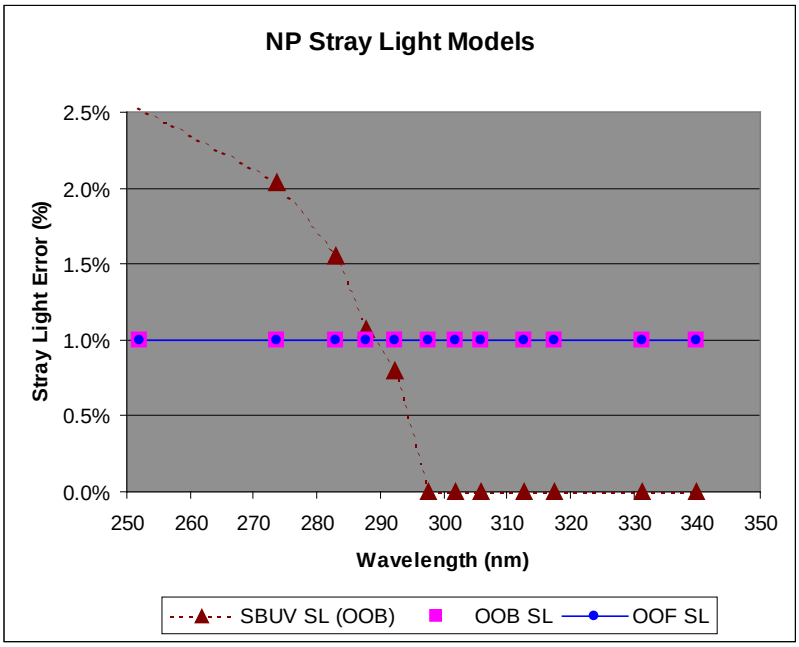

Figure 7.7-1. OMPS NP Stray Light Model

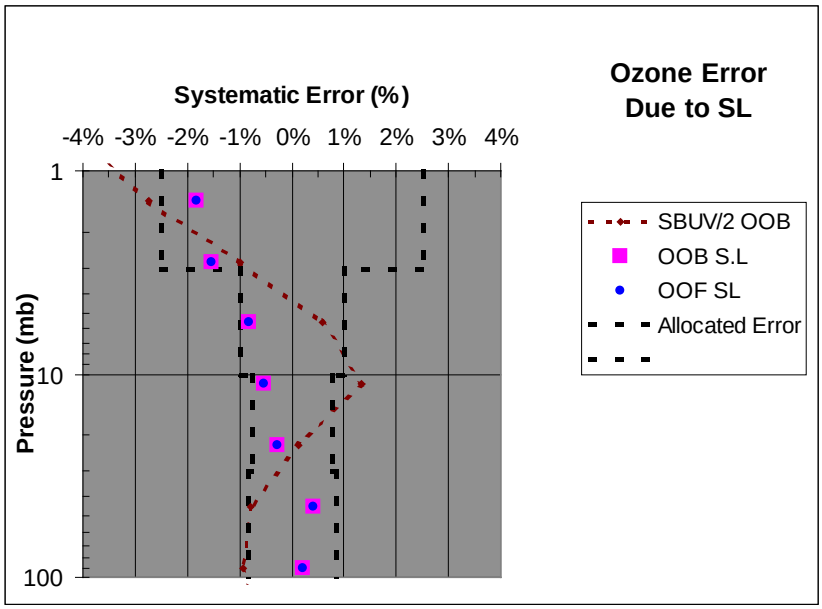

Figure 7.7-2. NP Algorithm Sensitivity to Stray Light. The thick dashed line is the allocated error due to OOB (OOF) stray light. The solid line is the stray light performance for the allocated OOB (OOF) levels.

7.8 SNR SENSITIVITY STUDY

We used allocated OMPS SNRs for the SNR sensitivity study. The SNRs for the shortest eight channels are the same as SBUV/2 nominal SNRs. SNRs for the other five channels are based on the OMPS TC allocated SNRs (see **Table 7.8-1**).

Table 7.8-1. OMPS and SBUV/2 SNR comparison

Wavelength	*SBUV/2*	*Allocated SNR*
2520.	**35.**	***35.***
2736.	***100.***	***100.***
2831.	***200.***	***200.***
2876.	***260.***	***260.***
2923.	***400.***	***400.***
2976.	***400.***	***400.***
3019.	***400.***	***400.***
3058.	***400.***	***400.***
3125.	***400.***	***1000.***
3175.	***400.***	***1000***
3312.	***400.***	***1000.***
3398.	***400.***	***1000.***
3786.	***400.***	***1000.***

Since no major modifications have been made to the SBUV V6 algorithm, we expect that the improved SNR values will result in smaller values for ozone profile errors. **Table 7.8-2** shows this improvement based on computations for four standard atmospheres (L225, M225, M575, H125).

Table 7.8-2: SNR Performance Table

	Heritage Performance			OMPS Simulation		
Altitude Range	**Error**	**Sensitivity Factor**	**Ozone Error**	**Error**	**Sensitivity Factor**	**Ozone Error**
1 mb	2.9%	0.7 % / %	2.0%	2.9 %	0.7 % / %	2.0%
3 mb	.25 %	6.4 % / %	1.6%	0.25 %	6.4 % / %	1.6%
10 mb	.25 %	4.8 % / %	1.2 %	0.25 %	4.8 % / %	1.2%
30 mb	.25 %	4.4 % / %	1.1 %	0.25 %	3.6 % / %	0.9%

7.9 SUMMARY FOR ACCURACY AND PRECISION

Nadir Profiler retrieval accuracy allocation in the OMPS System Specification is 7% at 1 mb. The precision allocation is 10% at 30 mb. These allocations are based on the performance of the heritage SBUV/2 system. In our error budget approach, we essentially follow the method used in computing the error budget of the SBUV system. The additional errors not present in SBUV are wavelength interpolation error and co-boresighting error. Our studies show these errors to be relatively small compared to other error budget terms. The results are summarized in the **Tables 7.9-1** and **7.9-2**.

Table 7.9-1. Accuracy error budget for OMPS NP at 1 mb

Error Source	Ozone error (%)	Comments
Rayleigh Scattering Coefficient	0.5	Based on work of Eric Shettle
Ozone Absorption Cross-Section	3	The same as SBUV
Retrieval Error	3	The same as SBUV
Wavelength Calibration	0.1	Studied for RRR1 and RRR3, also see Nadir Profiler Test Results Report
Radiometric Error	5.01	Combined error, includes Radiometric Calibration and Stray Light, see section 7.7.
Total Error	6.6	Allocation is satisfied

Table 7.9-2. Precision error budget for OMPS NP at 30 mb

Error Source	Ozone error (%)	Comments
Sensor Noise (SNR)	0.9	See SNR sensitivity study, section 7.8.
Atmospheric temperature	1	The same as for SBUV
Retrieval Error	10	The same as for SBUV
Interpolation Error	0.15	New error source, negligible compared to already existing errors, subsection 3.2.1
Total Error	10	Allocation is satisfied

8 References

Bass, A.M., and R. J. Paur, The ultraviolet cross-section of ozone, I, The measurements, in Atmospheric Ozone, edited by C.S. Zerefos and A Ghazi, pp 606-610, D. Reidel, Norwood, Mass., 1984. (Proceedings from 1984 Ozone Symposium.)

Bates, D. R., Rayleigh scattering by air, *Planet. Sp. Sci., 32,* 785-790, 1984.

Bhartia, P. K., K. F. Kienk, V.G. Kaveeshwar, S. Ahmad, A. J. Fleig, R. D. McPeters, and C. L. Mateer, Algorithm for vertical ozone profile determination for the Nimbus-4 BUV data set, *Proceedings, Fourth Conference on Atmospheric Radiation,* Toronto, Ont., Canada, pp. 27-32, 1981.

Bhartia, P. K., D. Silberstein, B. Monosmith, and Albert J. Fleig, Standard profiles of ozone from ground to 60 km obtained by combining satellite and ground based measurements, in *Atmospheric Ozone,* edited by C. S. Zerefos and A. Ghazi, pp. 243-247, D. Reidel, Dordrecht, 1985.

Bhartia, P. K., R. D. McPeters, C. L. Mateer, L. E. Flynn, and C. Wellemeyer, Algorithm for the estimation of vertical ozone profiles from the backscattered ultraviolet technique, *J. Geophys. Res., 101, D13,* pp. 18793-18806, 1996.

Chapman, S., The absorption and dissociative or ionizing effect of monochromatic radiation in an atmosphere on a rotating earth, *Proc. Phy. Soc. (London),* 43, 483-501, 1931.

Dave, J. V., Meaning of successive iteration of the auxiliary equation of radiative transfer, *Astrophys. J., 140,* 1292-1303, 1964.

Dave, J. V., Effect of aerosols on the estimation of total ozone in an atmospheric column from the measurement of its ultraviolet radiance, J. *Atmos. Sci., 35,* 899-911,1978.

ECS Project, 1995. Theoretical Basis of the SDP Toolkit Geolocation Package for the ECS Project, Technical Paper, 445-TP-002-002.

Environmental Science Services Administration, National Aeronautics and Space Administration, and United States Air Force, U. S. standard atmosphere supplements, 1966, U.S. Government Printing Office, Washington, D.C., 1966.

Fleig, Albert J., R. D. McPeters, P. K. Bhartia, Barry M. Schlesinger, Richard P. Cebula, K. F. Klenk, Steven L. Taylor, and D. F. Heath, 1990, Nimbus-7 Solar Backscatter Ultraviolet (SBUV) Ozone Products User's Guide, NASA Reference

Publication, 1234, National Aeronautics and Space Administration, Washington, DC.

Fraser, R. S., and Z. Ahmad, The effect of surface reflection and clouds on the estimation of total ozone from satellite measurements. Fourth NASA Weather and Climate Program Science Review, *NASA Conf. PubI. 2076, [NTIS N79206331* pp.247-252, 1978.

Joiner, J., Bhartia, P.K., Cebula, R.P., Hilsenrath, E., and McPeters, R.D., "Rotational-Raman Scattering (Ring Effect) in Satellite Backscatter Ultraviolet Measurements, *Appl. Opt., 34*, 4513-4525, 1995.

Klenk, K .F., P. K. Bhartia, A. J. Fleig, V. G. Kaveeshwar, R. D. McPeters and P. M. Smith, Total ozone determination from the Backscattered Ultraviolet (BUV) experiment, f *AppI. Meteor., 21,* 1672-1684, 1982.

Klenk, K. F., P. K. Bhartia, A. J. Fleig, and C. L. Mateer, Vertical ozone profile determination from Nimbus-7 SBUV measurements, in *Proceedings, Fifth Conference on Atmospheric Radiation,* Baltimore, MD, 1983.

Krueger, A. J., Detection of volcanic eruptions from space by their sulfur dioxide clouds, Proceedings AIAA 23rd Aerospace Sciences Meeting, January 14—17, *1985.*

NIMA, 1997. NIMA TR8350.2: Department of Defense World Geodetic System 1984, Its definition and Relationship with Local Geodetic Systems, Third Edition, prepared by the NIMA WGS84 Development Committee.

Paur, R., and A. M. Bass, The ultraviolet cross-sections of ozone: II. Results and temperature dependence, in *Atmospheric Ozone,* edited by C. S. Zerefos and A Ghazi, pp.611-616, D. Reidel, Dordrecht, 1985.

Rodgers, C. D., Retrieval of atmospheric temperature and composition from remote measurements of thermal radiation, *Rev. Geophys. Sp. Phys., 14,* 609-624, 1976.

Taylor, S. L., P. K. Bhartia, V. G. Kaveeshwar, K. F. Kierik, A. 3. Fleig, C. L. Mateer, Role of multiple scattering in ozone profile retrieval from satellite measurements in ultraviolet, *Remote Sensing of Atmospheres and Oceans,* Williamsburg Va., Academic Press, pp 219-231. 1980.

Wertz, J.R. (ed.) 1985, Spacecraft Attitude Determination and Control, D. Reidel Publishing Co., Vol. 73.

Wellemeyer, C.G., S.L. Taylor, C.J. Seftor, R.D. McPeters, P.K. Bhartia, A correction for TOMS profile shape errors at high latitude, *J. Geophys. Res.,* submitted (1996).

Gleason, J. F., R. D. McPeters, and J. R. Herman, "Characterization and Analysis of the Nimbus-7 SBUV Data in the "Non-sync" Period (February 1987 - June 1990)," *Ozone in the Troposphere and Stratosphere*, Edited by Robert D Hudson, pp. 236-239, 1992.

Gleason, J. F., P. K. Bhartia, J. R. Herman, R. McPeters, P. Newman, R. S. Stolarski, L. Flynn, G. Labow, D. Larko, C. Seftor, C. Wellemeyer, W. D. Komhyr, A. J. Miller, and W. Planet, "Record low global ozone in 1992," *Science, 260*, 523-526, 1993.

Hughes STX Corporation, "Nimbus-7 TOMS wavelength scale adjustments," *Hughes STX Doc. HSTX-3036-212-MD-94-007*, 1994.

Jaross, G., A. Krueger, R. P. Cebula, C. Seftor, U. Hartmann, R. Haring, and D. Burchfield, "Calibration and post-launch performance of the Meteor 3/TOMS instrument," *J. Geophys. Res.*, *100*, 2985-2995, 1995.

McPeters, R. D., T. Miles, L. E. Flynn, C. G. Wellemeyer, and J. M. Zawodny, "Comparison of SBUV and SAGE II ozone profiles: Implications for ozone trends", *J. Geophys. Res.*, *99*, 20513-20524, 1994.

Taylor, S. L., R. D. McPeters, and P. K. Bhartia, "Procedures to validate/correct calibration error in solar backscattered ultraviolet instruments", in Proceedings of the Quadrennial Ozone Symposium, *NASA Conf. Publ. 3266,* 1994.

Wellemeyer, C. G., S. L. Taylor, R. R. Singh, and R. D. McPeters, "External comparisons of reprocessed SBUV/TOMS ozone data", in Proceedings of the Quadrennial Ozone Symposium, *NASA Conf. Publ. 3266,* 1994.

Related Literature

Chandrasekar, S., Radiative Transfer, Oxford University Press, London, 1950.

Heath, D. F., A. J. Krueger, and H. Park, in *The Nimbus-7 User's Guide,* edited by C. R. Madrid, pp.175-187, NASA Goddard Space Flight Center, Greenbelt, MD, 1978.

Heath, D. F., A. J. Krueger, H. A. Roeder, and B. D. Henderson, The Solar Backscatter Ultraviolet and Total Ozone Mapping Spectrometer (SBUV/TOMS) for Nimbus G, *Opt. Eng., 14,* 323-331, 1975.

Klenk, K.F., et al.,"Standard ozone profiles from balloon and satellite sata sets*," J. Climate Appl. Meteorol., 22*, 2012-2022, 1983.

McPeters, R.D., P.K. Bhartia, A.J. Krueger, J.R. Herman, B.M. Schlesinger, C.G. Wellemeyer, C.J. Seftor, G. Jaross, S.L. Taylor, T. Swissler, O. Torres, G. Labow, W. Byerly, and R. P. Cebula, Nimbus-7 TOMS Ozone Mapping Spectrometer (TOMS) Data Products User's Guide*, NASA Reference Publication 1384*, Apr (1996).

Appendix A. Definition of SBUV Profile Layer and Levels

SBUV ozone profiles are reported in two separate ways:

1) As ozone amounts (milli-atm-cm) in 12 atmospheric layers with their 1σ uncertainties expressed as a percentage of the layer amounts.

2) As ozone volume mixing ratios at 19 selected pressure levels from 0.3 mbar to 100 mbar.

Error bars are not reported for mixing ratios because they are virtually the same as those for layer amounts for a vertically smooth ozone profile.

Table A-1 defines the layers for which SBUV layer ozone amounts are reported. Most of these layers are similar to those used by operational Umkehr technique, except that they are numbered differently in that the Umkehr layer 1 spans 253-507 mbar.

Table A-1. Standard Layers Used for Ozone Profiles

SBUV Layer Number	Umkehr Layer Number	Layer Pressure (mb)	Pressure at Altitude of Midpoint	Layer Midpoint (km)
1	–	0.000 – 0.247	–	–
2	–	0.247 – 0.495	.350	56.5
3	–	0.495 – 0.990	.700	51.0
4	9	0.990 – 1.980	1.40	45.5
5	8	1.980 – 3.960	2.80	40.2
6	7	3.960 – 7.920	5.60	35.2
7	6	7.920 – 15.80	11.2	30.4
8	5	15.80 – 31.70	22.4	25.8
9	4	31.70 – 63.30	44.8	21.3
10	3	63.30 – 127.0	89.6	17.0
11	2	127.0 – 253.0	179.0	12.5
12	0 and 1	253.0 – 1013	507.0	5.5

Table A-1 also gives the pressure and altitude of the layer midpoints (defined in terms of altitude). These are useful quantities since the layer mean partial pressure reported by Umkehr is often very close to the true partial pressure at the layer midpoint for a vertically smoothed ozone profile. Layer ozone amounts (milli-atm-cm), reported by SBUV, can be easily converted to layer mean partial pressures (mb) by multiplying by 1.828 for layers 2 through 11, and by 0.914 for layer 1.

Ozone mixing ratios O_3 are obtained from the following equation

$$O_3 = [(2.096/p)(dx/d \log p)],$$

where O_3 is the ozone mixing ratio in micrograms/gram, p is the pressure in millibars, and x is the cumulative ozone amount above pressure p in milli-atm-cm, obtained by summing the layer amounts.

To obtain the necessary derivative, a cubic spline is fit to the x-log p curve. Simulation results show that this procedure does not increase the retrieval errors provided the x-log p curve is smooth, as it is for SBUV retrieval. The values of the solution profile volume mixing ratios are given in order of increasing atmospheric pressure at the 19 pressure levels: 0.3, 0.4, 0.5, 0.7, 1.0, 1.5, 2.0, 3.0, 4.0, 5.0, 7.0, 10, 15, 20, 30, 40, 50, 70, and 100 mbar.

Finally, it should be mentioned that ozone mixing ratios are often expressed as parts per million by volume (ppmv), which are obtained by dividing the mixing ratio values (given in parts per million by mass) by 1.657. Partial pressure (mbar) is obtained by multiplying the mixing ratio (ppmv) by the pressure (mbar).

Appendix B. Climatological Profiles Used for Total Ozone Tables

Umkehr layer ozone amounts in milli-atm-cm (DU) are given for each standard profile, comprising low, mid and high latitude profiles for a range of total column amounts in milli-atm-cm.

Profile	0&1	2	3	4	5	6	7	8	9	>10
225 Low	26.0	5.0	7.0	25.0	62.2	57.0	29.4	10.9	3.2	1.3
275 Low	26.0	6.0	16.0	52.0	75.2	57.0	29.4	10.9	3.2	1.3
325 Low	26.0	10.0	31.0	71.0	87.2	57.0	29.4	10.9	3.2	1.3
125 Mid	16.5	18.3	7.6	8.2	28.6	22.0	12.4	7.7	2.5	1.2
175 Mid	17.5	22.8	21.0	24.9	35.3	26.8	15.0	8.0	2.5	1.2
225 Mid	27.0	12.0	14.0	40.0	52.1	39.2	24.5	11.1	3.7	1.4
275 Mid	28.0	15.0	29.0	58.0	63.7	40.6	24.5	11.1	3.7	1.4
325 Mid	30.0	26.0	45.0	74.7	66.9	41.7	24.5	11.1	3.7	1.4
375 Mid	32.0	39.0	64.0	85.7	71.1	42.5	24.5	11.1	3.7	1.4
425 Mid	34.0	54.0	84.0	97.7	71.7	42.9	24.5	11.1	3.7	1.4
475 Mid	38.0	72.0	107.7	101.0	72.6	43.0	24.5	11.1	3.7	1.4
525 Mid	42.0	91.0	131.7	108.0	68.8	42.8	24.5	11.1	3.7	1.4
575 Mid	58.1	114.0	134.8	114.0	75.8	40.2	21.7	10.7	4.1	1.6
125 High	16.5	18.3	7.6	8.2	28.6	22.0	12.4	7.7	2.5	1.2
175 High	17.5	22.8	21.0	24.9	35.3	26.8	15.0	8.0	2.5	1.2
225 High	18.0	24.6	41.7	46.0	38.0	28.8	15.4	8.3	2.9	1.3
275 High	26.0	30.5	62.9	59.2	38.5	28.8	15.4	8.9	3.4	1.4
325 High	29.0	40.8	78.6	71.2	45.7	28.8	17.2	8.9	3.4	1.4
375 High	33.0	53.2	89.8	82.2	51.9	32.5	18.7	8.9	3.4	1.4
425 High	38.0	68.7	100.9	91.2	56.9	35.6	20.0	8.9	3.4	1.4
475 High	45.0	85.0	114.1	99.0	59.8	37.5	20.9	8.9	3.4	1.4
525 High	54.0	104.1	128.1	105.0	60.2	38.2	21.7	8.9	3.4	1.4
575 High	58.1	114.0	134.8	114.0	75.8	40.2	21.7	10.7	4.1	1.6

Climatological temperature profiles used for total ozone tables. Separate temperature profiles are used for low, mid and high latitudes, and two additional profiles are used for the special low ozone amount profiles (125 milli-atm-cm and 175 milli-atm-cm) associated with the Antarctic Spring minimum in total ozone.

Profile	0&1	2	3	4	5	6	7	8	9	>9
Low Lat.	267.0	214.0	201.0	210.0	222.0	234.0	248.0	261.0	270.0	271.0
Mid Lat.	256.0	216.0	214.0	217.0	222.0	229.0	240.0	254.0	265.0	268.0
125 milli-atm-cm	228.0	196.0	191.0	193.0	210.0	220.0	240.0	260.0	272.0	272.0
175 milli-atm-cm	228.0	196.0	196.0	206.0	225.0	238.0	254.0	266.0	272.0	272.0
High Lat.	244.0	221.0	222.0	222.0	221.0	227.0	235.0	243.0	256.0	261.0

Appendix C: *A Priori* Ozone Profile Covariance Matrix

Covariance elements must be multiplied by 10^{-2}.

Layer	1	2	3	4	5	6	7	8	9	10	11	12
1	1.44	0.00	0.00	0.00	0.00	0.00	0.00	0.00	0.00	0.00	0.00	0.00
2	0.00	1.00	0.00	0.00	0.00	0.00	0.00	0.00	0.00	0.00	0.00	0.00
3	0.00	0.00	0.64	0.00	0.00	0.00	0.00	0.00	0.00	0.00	0.00	0.00
4	0.00	0.00	0.00	0.64	0.20	0.00	0.00	0.00	0.00	0.00	0.00	0.00
5	0.00	0.00	0.00	0.20	0.64	0.24	0.00	0.00	0.00	0.00	0.00	0.00
6	0.00	0.00	0.00	0.00	0.24	0.64	0.24	0.00	0.00	0.00	0.00	0.00
7	0.00	0.00	0.00	0.00	0.00	0.24	1.00	0.20	-0.45	0.00	0.00	0.00
8	0.00	0.00	0.00	0.00	0.00	0.00	0.20	1.00	0.30	-0.75	0.00	0.00
9	0.00	0.00	0.00	0.00	0.00	0.00	-0.45	0.30	2.25	0.75	-1.57	0.00
10	0.00	0.00	0.00	0.00	0.00	0.00	0.00	-0.75	0.75	6.25	0.00	-1.87
11	0.00	0.00	0.00	0.00	0.00	0.00	0.00	0.00	-1.57	0.00	12.25	0.00
12	0.00	0.00	0.00	0.00	0.00	0.00	0.00	0.00	0.00	-1.87	0.00	6.25